

**AD-A243 546****ENTATION PAGE**
 Form Approved  
 OMB No 0704-0188

1

Implied to average 1 hour per response, including the time for reviewing instructions, searching existing data sources, and reviewing the collection of information. Send comments regarding this burden estimate or any other aspect of this burden to: Washington Headquarters Services, Directorate for Information Operations and Reports, 1215 Jefferson Dr, Office of Management and Budget, Paperwork Reduction Project (0704-0188), Washington, DC 20503.

|   |  |  |                            |
|---|--|--|----------------------------|
| PORT DATE   |  | 3. REPORT TYPE AND DATES COVERED<br><b>THESIS/DISSERTATION</b>       |                            |
| 4. TITLE AND SUBTITLE<br><br>Optical Properties of Thermally Intermixed Quantum Wells<br>an Superlattices   |  | 5. FUNDING NUMBERS   |                            |
| 6. AUTHOR(S)<br><br>Michael W. Prairie, Captain   |  |  |                            |
| 7. PERFORMING ORGANIZATION NAME(S) AND ADDRESS(ES)<br><br>AFIT Student Attending: North Carolina State University   |  | 8. PERFORMING ORGANIZATION REPORT NUMBER<br><br>AFIT/CI/CIA- 91-020D |                            |
| 9. SPONSORING / MONITORING AGENCY NAME(S) AND ADDRESS(ES)<br><br>AFIT/CI<br>Wright-Patterson AFB OH 45433-6583  |  | 10. SPONSORING / MONITORING AGENCY REPORT NUMBER                     |                            |
| 11. SUPPLEMENTARY NOTES<br><br>C  |  |  |                            |
| 12a. DISTRIBUTION/AVAILABILITY STATEMENT<br><br>Approved for Public Release IAW 190-1<br>Distributed Unlimited<br>ERNEST A. HAYGOOD, Captain, USAF<br>Executive Officer |  | 12b. DISTRIBUTION CODE   |                            |
| 13. ABSTRACT (Maximum 200 words)  |  |  |                            |
| 14. SUBJECT TERMS   |  | 15. NUMBER OF PAGES<br>159   |                            |
|   |  | 16. PRICE CODE   |                            |
| 17. SECURITY CLASSIFICATION OF REPORT   | 18. SECURITY CLASSIFICATION OF THIS PAGE | 19. SECURITY CLASSIFICATION OF ABSTRACT                              | 20. LIMITATION OF ABSTRACT |

**AUTHOR:** Michael W. Prairie, Captain, USAF

۲۰۸

## **TITLE: Optical Properties of Thermally Intermixed Quantum Wells and Superlattices**

**DEGREE:** Ph.D., Electrical Engineering

DATE: 1991

**INSTITUTION:** North Carolina State University

**PAGES:** 159

## ABSTRACT:

→ The optical properties of thermally intermixed GaAs/AlGaAs quantum wells and superlattices are examined using thermal annealing, photoluminescence (PL), time-resolved photoluminescence (TPL), and theoretical models. A computer model to calculate the energy structure of intermixed quantum wells is refined and used with PL and TPL techniques to characterize the properties of thin (1 monolayer (ML) to 8 ML) annealed wells. A model for intermixed superlattices is developed next which predicts the changes in energy dispersion and density of states with annealing time, and is verified using PL and TPL.

Selective intermixing techniques using a gallium focused ion beam (FIB),  $\text{SiN}_x$  encapsulation, and patterned GaAs grown at low substrate temperature (LT-GaAs) are then studied. The FIB technique tends to suppress layer interdiffusion in and around the implanted region. The  $\text{SiN}_x$  encapsulation is most promising with an interdiffusion selectivity ratio of more than 4:1. Initial LT-GaAs experiments show a small selectivity between regions. ↵

Finally, a model of the dielectric constant for partially intermixed quantum wells is developed using a modified optical matrix element which takes into account the electron-hole wavefunction overlap, as well as the penetration of the wavefunctions into the barriers of thin and intermixed wells. The radiative lifetime is calculated and compared with TPL data. The results suggest transport of crystal defects from the surface during the annealing process. Next, the index of refraction of intermixed wells is calculated, and a 3-dB power splitter is designed as an example of selective intermixing applied to integrated optics.

91-17926

6

91 1213 176

甲子日

# Optical Properties of Thermally Intermixed Quantum Wells and Superlattices

by

Michael William Prairie  
Captain, United States Air Force

A thesis submitted to the Graduate Faculty of  
North Carolina State University  
in partial fulfillment of the  
requirements for the Degree of  
Doctor of Philosophy

Electrical and Computer Engineering  
Department

Raleigh

1991

Approved by:

R. T. M. Kalbar  
Chairman of Advisor Committee

|                   |         |
|-------------------|---------|
| Accession No.     |         |
| Author            | Special |
| Date              | 1991    |
| Approved          |         |
| Classification    |         |
| By _____          |         |
| Distribution      |         |
| Approved by _____ |         |
| Dist              | Special |
| R-1               |         |

J. B. Burkhardt J. H. Law  
J. B. Burkhardt



## Abstract

PRAIRIE, MICHAEL WILLIAM. Optical Properties of Thermally Intermixed Quantum Wells and Superlattices. (Under the direction of Robert M. Kolbas.)

The electronic structure and optical properties of thermally intermixed GaAs/AlGaAs quantum wells and superlattices are examined using thermal annealing in a controlled environment, time-integrated and time-resolved photoluminescence (PL and TPL, respectively), and theoretical models based on the envelope-function approximation. A computer model to calculate the energy structure of intermixed quantum wells is refined and used with PL and TPL techniques to characterize the luminescence properties of thin (1 monolayer (ML) to 8 ML) annealed quantum wells. A model for intermixed superlattices is developed next which predicts the changes in energy dispersion and density of states with annealing time. Both PL and TPL are used to verify the validity of the model.

Selective intermixing techniques using a gallium focused ion beam (FIB),  $\text{SiN}_x$  encapsulation, and patterned GaAs grown at low substrate temperature (low-temperature GaAs, or LT-GaAs) are then studied. The FIB technique tends to suppress layer interdiffusion in and around the implant region. The  $\text{SiN}_x$  encapsulation is most promising with a selectivity ratio of more than 4:1. Initial LT-GaAs experiments show a small selectivity between regions.

Finally, a model of the dielectric constant for partially intermixed quantum wells is developed using a modified optical matrix element which takes into account the electron-hole wavefunction overlap, as well as the penetration of the wavefunctions into the barriers of thin and intermixed wells. The radiative lifetime is calculated from the matrix element, and compared with TPL data. The results suggest the transport of

crystal defects from the surface during the annealing process. Next, the index of refraction of partially intermixed wells is calculated, and a 3-dB power splitter is designed as an example of using selective intermixing in integrated optics.

*To Sharron.*

*My Wife, Technical Editor, and Best Friend.*

## Acknowledgements

I would like to express my deep appreciation to Dr. Robert M. Kolbas for the encouragement, support and guidance he provided throughout the course of this work. He has strengthened my ability to "see" the physics beyond the equations, and has taught me much about doing science that goes beyond the measurements and calculations. My gratitude also goes to Dr. K.W. Kim for his help with theoretical problems, and to Dr. J. Bernholc for his suggestions. Many thanks are also extended to committee members Dr. R.J. Trew and Dr. T.J. Lada, and to Dr. M.C. Osturk for a brief, but timely, exercise in humility.

I cannot forget to give credit to my family for helping me get through this challenging endeavor. Christopher has shown great maturity for a three-year-old, and I couldn't ask for more cooperation and patience than he has given. Kaitlyn, only three months old at this writing, has been nothing short of amazing herself. She was sleeping through the night before the first month (read: Dad was able to get some rest), and has been either happy or sleeping the rest of the time. Sharron gets most of the credit, however, since I probably wouldn't have started this program without her encouragement. Without her support, I probably wouldn't have survived, and without her typing and editing, I definitely wouldn't have finished on time. I also thank my mother for her support and encouragement throughout my life when I made the choices which eventually led me to this point. My thanks to Jan and Dan for helping to smooth the way for Sharron, Christopher, Kaitlyn and me during the more recent years.

Knowing and working with the members of Dr. Kolbas' group has been an enjoyable experience, both technically and culturally, that I will not soon forget. I am grateful to Dr. Ken Hsieh for passing on to me everything I know about sealing

ampoules and for getting me started in other aspects of the lab. I also thank the other crystal growers, Dr. Jung Lee, Yawlin Hwang, Tong Zhang, and Mark Mytych, for without them, there would be little to do in the lab. I am indebted to Willie Yin for taking me under his wing in the processing lab. I thank Dick Kuehn and Joan O'Sullivan for their assistance, and Yongkun Sin for some helpful hints. I thank Dr. David Dreifus and Barbara Frank for their suggestions early in my program. I am grateful to Subash Krishnankutty for re-teaching me how to integrate and embarrassing me with my limited knowledge of American history. I particularly appreciate the many fruitful discussions I've had with Dr. David Benjamin, as well as his expertise in photoluminescence spectroscopy. Along with Dr. Benjamin, I thank Dahua Zhang for all the picoseconds they spent taking data for me, and I am grateful to Dahua for the many technical and philosophical discussions we have had. Finally, I want to thank Rick Reed and Will Rowland for the questions they have as they begin a new generation in the group, for they force me to think about what I am doing.

Finally, I wish to thank the Air Force Institute of Technology Civilian Institute Program for selecting and supporting me through this degree program. I thank the AFROTC Staff for their administrative support, and Maj. Lauraleen O'Connor for her support and guidance as AFIT Liaison Officer.

# Table of Contents

|  |           |
|--|-----------|
| List of Figures .....  | vii       |
| Table of Tables .....  | ix        |
| List of Abbreviations .....  | x         |
| List of Symbols .....  | xii       |
| <b>1 Introduction .....</b>  | <b>1</b>  |
| 1.1 Motivation .....   | 1         |
| 1.2 Overview of Thesis .....   | 3         |
| <b>2 Review of Thermal Intermixing and Optical Properties of Quantum Wells and Superlattices .....</b> | <b>6</b>  |
| 2.1 Thermally Intermixed Quantum Wells and Superlattices .....   | 6         |
| 2.1.1 Heterojunction Intermixing .....   | 6         |
| 2.1.2 Intermixed Heterostructure Potential Wells .....   | 16        |
| 2.2 Optical Properties of Semiconductor Quantum Structures .....                                       | 24        |
| <b>3 Experimental Methods .....</b>  | <b>28</b> |
| 3.1 Crystal Growth .....   | 28        |
| 3.2 Optical Characterization .....   | 29        |
| 3.2.1 Standard Photoluminescence (PL) Spectroscopy .....   | 31        |
| 3.2.2 Time-Resolved Photoluminescence (TPL) Spectroscopy .....   | 32        |
| 3.3 Thermal Annealing .....  | 34        |
| 3.4 Device Processing .....  | 38        |
| 3.5 Hall Mobility Measurements .....   | 40        |
| <b>4 Heterostructure Intermixing .....</b>   | <b>42</b> |
| 4.1 Error Function Model for Intermixed Quantum Wells .....  | 42        |
| 4.2 Compositional Dependence on the Interdiffusion Coefficient .....                                   | 49        |
| 4.3 Model for Intermixed Superlattices .....   | 56        |
| <b>5 Selective Intermixing .....</b>   | <b>63</b> |
| 5.1 Localized Gallium Overpressure .....   | 63        |
| 5.1.1 Gallium Focused Ion Beam .....   | 63        |
| 5.1.2 Electron Mobility Experiment .....   | 65        |
| 5.2 $\text{SiN}_x$ Encapsulation .....   | 67        |
| 5.3 Low-Temperature Gallium Arsenide .....   | 69        |
| <b>6 Optical Properties of Intermixed Quantum Wells .....</b>  | <b>72</b> |
| 6.1 The Matrix Element of Intermixed Quantum Wells .....   | 73        |
| 6.1.1 Theory .....   | 74        |
| 6.1.2 Lifetime Experiment .....  | 82        |
| 6.2 Damping Coefficient .....  | 88        |
| 6.3 Density of States .....  | 89        |
| 6.4 Index of Refraction .....  | 92        |

|  |            |
|--|------------|
| <b>7 The Trek .....</b>  | <b>99</b>  |
| 7.1 Voyages .....  | 99         |
| 7.2 Where No One Has Gone Before .....   | 102        |
| 7.3 The Continuing Mission .....   | 104        |
| <b>8 References .....</b>  | <b>106</b> |
| <b>9 Appendices .....</b>  | <b>111</b> |
| 9.1 Appendix A: The Dielectric Constant .....                                      | 112        |
| 9.1.1 The Oscillator Model .....   | 113        |
| 9.1.2 Quantum Mechanical Model .....   | 114        |
| 9.1.3 Oscillator Strength and Lineshape Broadening .....                           | 118        |
| 9.1.4 Dielectric Constant .....  | 119        |
| 9.2 Appendix B: Optical Matrix Elements in Quantum Wells .....                     | 122        |
| 9.3 Appendix C: The Density of States for Quantum Wells and<br>Superlattices ..... | 131        |
| 9.4 Index .....  | 132        |

## List of Figures

|   |    |
|---|----|
| <b>Figure 1.1</b> Schematic of a selectively intermixed quantum well.....   | 4  |
| <b>Figure 2.1</b> Schematic of the interdiffusion process. ....   | 8  |
| <b>Figure 2.2</b> Al-Ga interdiffusion coefficient as a function of annealing environment. ....                                       | 11 |
| <b>Figure 2.3</b> Al-Ga interdiffusion coefficient as a function of overpressure source quantity. ....                                | 12 |
| <b>Figure 2.4</b> Energy diagram of an intermixed GaAs/AlGaAs quantum well. ....  | 18 |
| <b>Figure 2.5</b> Al-Ga interdiffusion coefficient as a function of temperature and aluminum composition. ....                        | 20 |
| <b>Figure 3.1</b> The photoluminescence process. ....   | 30 |
| <b>Figure 4.1</b> Composition profile of an intermixed quantum well.....  | 43 |
| <b>Figure 4.2</b> Stair-step approximation to the intermixed quantum well.....  | 45 |
| <b>Figure 4.3</b> Convergence of the calculated bound state for an intermixed quantum well. ....                                      | 46 |
| <b>Figure 4.4</b> Transition wavelength shifts for intermixed quantum wells as a function of well width. ....                         | 48 |
| <b>Figure 4.5</b> Comparison of error function and composition-dependent diffusion of a GaAs/AlGaAs quantum well. ....                | 51 |
| <b>Figure 4.6</b> Structure to test compositional dependence of the interdiffusion coefficient. ....                                  | 53 |
| <b>Figure 4.7</b> Composition-dependent Al-Ga interdiffusion coefficient as a function of annealing time.....                         | 55 |
| <b>Figure 4.8</b> Energy dispersion curves for an intermixed GaAs/AlAs superlattice. ....   | 59 |
| <b>Figure 4.9</b> Photoluminescence spectra of an annealed GaAs/AlAs superlattice. ....   | 60 |
| <b>Figure 4.10</b> Luminescence decay of the electron-to-light-hole transition. ....  | 62 |
| <b>Figure 5.1</b> Photoluminescence spectra of a selectively intermixed GaAs/AlAs superlattice via $\text{SiN}_x$ encapsulation. .... | 68 |

|   |     |
|---|-----|
| <b>Figure 5.2</b> Photoluminescence peaks of a selectively intermixed quantum well using low-temperature GaAs.....  | 71  |
| <b>Figure 6.1</b> Schematic for calculating the matrix element of a thin quantum well.....  | 76  |
| <b>Figure 6.2</b> Matrix element for $e_1$ - $hh_1$ transitions in a GaAs/Al <sub>0.3</sub> Ga <sub>0.7</sub> As quantum well as a function of well thickness.....                | 77  |
| <b>Figure 6.3</b> Matrix elements as a function of thickness for $e_1$ - $hh_1$ and $e_1$ - $lh_1$ transitions in a GaAs/Al <sub>0.3</sub> Ga <sub>0.7</sub> As quantum well..... | 78  |
| <b>Figure 6.4</b> Matrix elements for intermixed quantum wells.....   | 80  |
| <b>Figure 6.5</b> Separate confinement heterostructure for ultrathin quantum wells.....   | 83  |
| <b>Figure 6.6</b> Lifetimes of ultrathin GaAs/Al <sub>0.3</sub> Ga <sub>0.7</sub> As wells as a function of annealing time.....   | 85  |
| <b>Figure 6.7</b> Refractive index for an intermixed GaAs/Al <sub>0.3</sub> Ga <sub>0.7</sub> As quantum well.....  | 94  |
| <b>Figure 6.8</b> Electric field distribution for an optical waveguide defined by selective intermixing.....  | 96  |
| <b>Figure 6.9</b> Interaction length of a 3 dB optical waveguide coupler designed with disorder-defined waveguides.....   | 98  |
| <b>Figure 9.1</b> Coordinate system for the transformation of basis functions.....  | 124 |

## Table of Tables

|  |     |
|--|-----|
| <b>Table 9.1</b> Momentum Matrix Elements between Conduction- and Valence-Band states. ....  | 116 |
| <b>Table 9.2</b> Bulk and Quantum-Well average matrix elements $\langle P^2 \rangle$ for conduction-heavy hole, light hole, and split-off band transitions ..... | 127 |

## List of Abbreviations

|                     |  |
|---------------------|--|
| 2D                  | - Two-dimensional  |
| 3D                  | - Three-dimensional  |
| Al                  | - Chemical symbol for aluminum   |
| As                  | - Chemical symbol for arsenic  |
| CW                  | - Continuous wave  |
| DI-H <sub>2</sub> O | - Deionized water  |
| DOS                 | - Density of states  |
| e-hh                | - Electron to heavy hole   |
| e-lh                | - Electron to light hole   |
| FIB                 | - Focused ion beam   |
| FWHM                | - Full width at half maximum   |
| Ga                  | - Chemical symbol for gallium  |
| HEMT                | - High-electron mobility transistor                                    |
| I <sub>III</sub>    | - Interstitial defect; Group-III sublattice atom not at a lattice site |
| III <sub>V</sub>    | - Substitutional defect (e.g. Group-III atom in Group-V sublattice)    |
| IILD                | - Impurity-induced layer disordering                                   |
| KTP                 | - Frequency doubling crystal   |
| LT                  | - Low temperature  |
| MBE                 | - Molecular beam epitaxy   |
| ML                  | - Monolayer  |
| MODFET              | - Modulation-doped field effect transistor                             |
| MQW-LD              | - Multiple quantum well laser diode                                    |
| Nd:YAG              | - Neodymium-doped yttrium-aluminum-garnet                              |

|                        |   |
|------------------------|---|
| <b>ns</b>              | - Nanoseconds, $10^{-9}$ seconds        |
| <b>PL</b>              | - Photoluminescence                     |
| <b>ps</b>              | - Picoseconds, $10^{-12}$ seconds       |
| <b>RF</b>              | - Radio frequency                       |
| <b>RTA</b>             | - Rapid thermal annealing               |
| <b>SI</b>              | - Semi-insulating                       |
| <b>SLI</b>             | - Selective layer intermixing           |
| <b>TCE</b>             | - Trichloroethane                       |
| <b>TE</b>              | - Transverse electric                   |
| <b>TM</b>              | - Transverse magnetic                   |
| <b>TPL</b>             | - Time-resolved photoluminescence       |
| <b>V<sub>III</sub></b> | - Group-III vacancy; empty lattice site |

## List of Symbols

|                      |  |
|----------------------|--|
| $a$                  | - Period of a superlattice   |
| $\hat{a}_\lambda$    | - Unit vector in the direction of the electric field of $\lambda$ -polarized photons |
| $A_{mn}$             | - Probability of spontaneous emission (Einstein A coefficient)                       |
| $\alpha(\omega)$     | - Absorption coefficient; a function of frequency                                    |
| $B_{mn}$             | - Probability of stimulated emission (Einstein B coefficient)                        |
| $\beta_x$            | - Optical waveguide mode propagation coefficient in the x-direction                  |
| $\beta_y$            | - Optical waveguide mode propagation coefficient in the y-direction                  |
| $c$                  | - Speed of light   |
| $C$                  | - Composition  |
| $D$                  | - Diffusion coefficient  |
| $\Delta$             | - Split-off energy   |
| $\Delta t$           | - Increment of time  |
| $e$                  | - Electronic charge  |
| $E_g$                | - Bandgap energy   |
| $E_n$                | - Bound state energy   |
| $\epsilon(\omega)$   | - Complex dielectric constant, a function of frequency                               |
| $\epsilon'(\omega)$  | - Real part of the complex dielectric constant, a function of frequency              |
| $\epsilon''(\omega)$ | - Imaginary part of the complex dielectric constant, a function of frequency         |
| $\epsilon_0$         | - Free-space permitivity   |
| $\epsilon_b$         | - Background dielectric constant   |

|                  |   |
|------------------|---|
| $erfc$           | - Error function  |
| $f$              | - Oscillator strength   |
| $\gamma$         | - Damping coefficient (frequency)   |
| $\Gamma$         | - Damping coefficient (energy)  |
| $\hbar$          | - Planck's constant   |
| $\hbar$          | - Planck's constant ( $\frac{\hbar}{2\pi}$ )                                |
| $h\nu$           | - Photon energy   |
| $k_B$            | - Boltzmann's constant  |
| $k$              | - Electron or hole wavevector   |
| $\kappa(\omega)$ | - Extinction coefficient; a function of frequency                           |
| $\kappa_c$       | - Coupling coefficient  |
| $L$              | - Coupling length for a directional coupler                                 |
| $\lambda_0$      | - Free-space wavelength   |
| $L_z$            | - Width of the quantum well   |
| $m$              | - Mode number for the optical waveguide                                     |
| $m$              | - Band index  |
| $M$              | - Mole number   |
| $m_e$            | - Free-electron mass  |
| $ M ^2$          | - Momentum matrix element squared   |
| $m^*$            | - Effective mass  |
| $\mu$            | - Reduced mass of the combined carriers in the conduction and valence bands |
| $n$              | - Index of refraction   |

|                         |  |
|-------------------------|--|
| $n$                     | - Band index   |
| $N$                     | - Number of oscillators  |
| $\bar{n}$               | - Group index of refraction  |
| $n_c$                   | - Complex index of refraction  |
| $n_{\lambda\beta}$      | - Photon occupation number given by the Bose-Einstein distribution function        |
| $\langle n   m \rangle$ | - Overlap of electron wavefunction in state $n$ and hole wavefunction in state $m$ |
| $n(\omega)$             | - Real part of the index of refraction; a function of frequency                    |
| $\omega$                | - Frequency  |
| $P$                     | - Overpressure   |
| $P_{mn}$                | - Interband matrix element   |
| $\bar{P}$               | - Macroscopic polarization   |
| $\Psi_n$                | - Wavefunction of the bound state  |
| $q$                     | - Superlattice wavevector  |
| $Q$                     | - Activation energy  |
| $R$                     | - Gas constant   |
| $R(\omega)$             | - Reflectivity; a function of frequency  |
| $\rho$                  | - Density of states  |
| $s$                     | - Separation between waveguides in a directional coupler                           |
| $S$                     | - Transfer matrix  |
| $t$                     | - Time   |
| $T$                     | - Temperature  |
| $\tau$                  | - Lifetime of the excited state  |

$\tau_{nr}$  - Non-radiative lifetime

$U(z)$  - Periodic potential

$V$  - Volume

$V(z)$  - Single well potential

$W$  - Weight

$W_g$  - Width of the waveguide

$x$  - Aluminum fraction in  $\text{Al}_x\text{Ga}_{1-x}\text{As}$

$y_0$  - The  $1/e$  point of the evanescent field in an optical waveguide

$z$  - Direction perpendicular to the heterostructure layers

# 1 Introduction

This chapter introduces previous work in thermally intermixed quantum wells and superlattices and provides an overview of the work done in this thesis. The evolution of semiconductor quantum structures for integrated optics is presented first, and serves as the motivation for studying the optical properties of partially intermixed quantum wells. Then, an overview of the goals and an outline of this thesis are given.

## 1.1 Motivation

Ever since 1974 when Esaki and Chang demonstrated resonant tunneling across potential barriers,<sup>[1]</sup> and Dingle *et al.* measured the quantized energy levels in a man-made quantum well,<sup>[2]</sup> the study of ultrathin semiconductor layers has exploded. As crystal growth improved and new materials were used to make these layers, many new electronic structures were possible, some of which have found their way into electronic and optical devices.<sup>[3]</sup> The underlying advantage of these structures is that the optical and electronic properties can be tailored by choosing appropriate materials and layer thicknesses. One example of this ability to engineer the properties of a semiconductor device is the quantum well heterostructure laser in which the emission wavelength can be selected by varying the thickness of the well.<sup>[4]</sup>

The dielectric response, which determines the index of refraction and the absorption properties of semiconductors is also dependent on the electronic structure. These characteristics can be adjusted through choices of materials and layer thicknesses in quantum wells and superlattices. Early work by Streifer *et al.* estimated the index of refraction of a multiple quantum well laser diode (MQW-LD) to be that of the average AlGaAs alloy over the entire superlattice or MQW-LD structure.<sup>[5]</sup> Ladig *et al.*<sup>[6]</sup> and Holonyak *et al.*,<sup>[7]</sup> however, showed that the index of a superlattice which had been

thermally intermixed into an average alloy was lower than adjacent areas of the superlattice which had been preserved. This effect had obvious applications to integrated optics. The selective intermixing was achieved through impurity-induced layer disordering (IILD), which was used by Deppe *et al.*<sup>[8]</sup> and Thornton *et al.*<sup>[9]</sup> to fabricate index-guided MQW-LD's which exhibited some of the lowest threshold currents of any semiconductor laser. The IILD technique was later used by Julien *et al.* to fabricate impurity-induced disorder-delineated passive optical waveguides.<sup>[10]</sup>

While IILD demonstrates the ability of selective disordering to delineate optical waveguides, it also introduces impurities into the waveguide structure. The optical field is then attenuated through scattering losses from three factors: (1) the increased number of defects; (2) increased interband absorption due to the shift in the absorption edge by the impurities, and (3) increased free carrier absorption since the impurities generate more free carriers.<sup>[11]</sup> In order to make low-loss waveguides, a method of selective disordering must be used which avoids the use of impurities. One way to do this is to control the point defects generated during high-temperature annealing steps using overpressures of the same elements that constitute the semiconductor structure.<sup>[12]</sup> The delineation of structures using this impurity-free method requires selective exposure of areas of the semiconductor to these overpressures. This can be accomplished by using a dielectric to mask selected regions for thermal annealing in an overpressure.<sup>[13,14]</sup> Another effective method is to implant constituent atomic species in or near the heterostructure to mechanically intermix the wells or to create a local internal "overpressure," respectively.<sup>[6,15,16]</sup>

The study of selective intermixing for use in integrated optical devices is in its infancy, and a great deal of work is needed before the technique can be used to fabricate sophisticated devices. For example, the index of refraction and electro-optic coefficients of intermixed quantum structures must be known precisely in order to

determine the dimensions and process conditions to build a directional-coupler switch. While data and models exist (and continue to be refined) for the index of quantum wells and superlattices<sup>[17-19]</sup> as well as alloys,<sup>[20,21]</sup> we would be naive to think that a selectively intermixed structure would be made up of regions of a perfectly preserved superlattice which abruptly joins to regions of completely intermixed alloys. In fact we would expect both the "preserved" and "intermixed" regions to be partially intermixed as shown in Figure 1.1, the differences being the degree to which they are intermixed. To date, no attempt to quantify the dielectric properties of partially intermixed quantum structures has been published. With that in mind, the purpose of this thesis is to extend the theories mentioned above to include partially intermixed quantum structures.

## 1.2 Overview of Thesis

In this thesis, the optical properties of thermally intermixed GaAs/AlGaAs quantum wells and superlattices are investigated. Specifically, the effects of atomic interdiffusion at the heterostructure interfaces on the optical matrix element are examined, and a theory is developed which describes the matrix element, and hence, the dielectric properties for partially intermixed wells. Several interdiffusion experiments were performed to characterize the intermixing process, and several existing theories were applied to the results to develop a new model. The emphasis throughout the thesis is on the application of intermixed quantum wells in optical waveguides for integrated optoelectronics.

A review of recent research which is relevant to this work is presented in Chapter 2. A record of the work performed in this thesis begins in Chapter 3, where the experimental methods are described. Chapters 4 and 5 contain the studies of the intermixing process. The former describes the work performed to characterize the

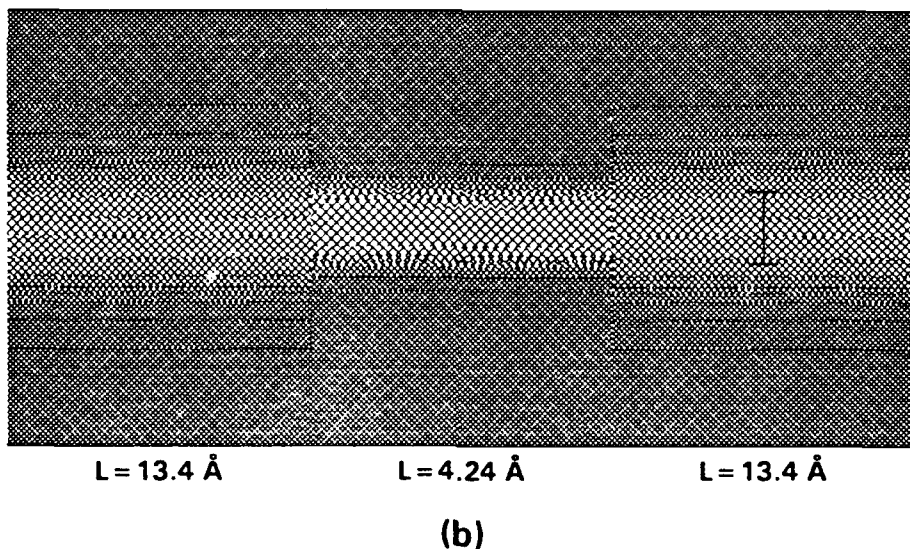
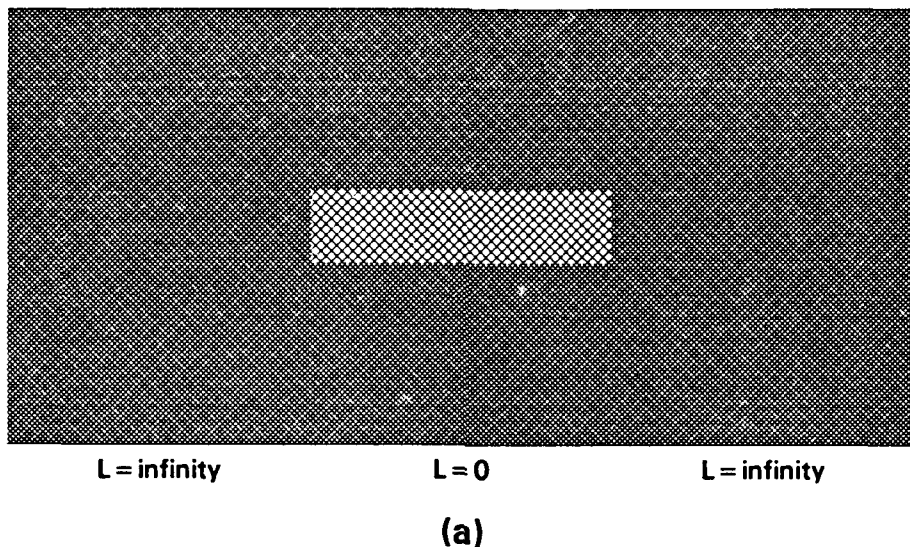


**Figure 1.1** Schematic of a selectively intermixed quantum well. The diffusion length  $L = \sqrt{Dt}$  is (a) infinity in the intermixed region and zero in the preserved region for the ideal case, and (b) finite for the realistic case. Here, a 10:1 ratio of the interdiffusion coefficient is assumed for the intermixed and preserved regions, respectively, ( $5 \times 10^{-18}$ : $5 \times 10^{-19}$ ) for a one-hour annealing process.

interdiffusion coefficient between GaAs/AlGaAs heterostructure interfaces, and the latter examines several techniques to selectively intermix quantum wells and superlattices.

The optical properties of intermixed wells are addressed in Chapter 6, where an original model for the optical matrix element in intermixed quantum wells is presented. This new matrix element is used to calculate the dielectric constant, which then allows for the first-ever calculation of the refractive index for partially intermixed quantum wells.

The work is summarized in Chapter 7, and conclusions are drawn regarding the applicability of using selectively intermixed quantum wells and superlattices in integrated optoelectronic devices. Finally, the reference list appears in Chapter 8, followed by a collection of appendices describing in depth some of the basic theories used in this thesis.

## 2 Review of Thermal Intermixing and Optical Properties of Quantum Wells and Superlattices

In this chapter, recent work in characterizing the mechanisms of thermal intermixing of quantum wells and superlattices is presented first. The development of theories to describe the dielectric constant, or optical properties of quantum structures (and hence, their refractive index and absorption properties) is presented separately. Although brief reference has been made to selective intermixing to produce local changes in the refractive index, these two methods have not been quantitatively combined until this study and will be reported in subsequent chapters where they are integrated for the first time.

### 2.1 Thermally Intermixed Quantum Wells and Superlattices

When first grown, quantum wells and superlattices are composed of layers of different materials with sharp interfaces. If these heterostructures are exposed to high enough temperatures, defects are generated in the crystal lattice which allow the materials at the heterojunctions to intermix. This results in a graded interface between the materials, which changes the shape of the original potential. The first task in controlling the intermixing of quantum structures, then, is to characterize the mechanisms of diffusion and find a way to control them.

#### 2.1.1 *Heterojunction Intermixing*

The AlGaAs material system has the zinc blende crystal structure which is composed of two inter-penetrating face-centered cubic sublattices. The Group-III sublattice contains the gallium and aluminum atoms, while the Group-V sublattice is

made up entirely of arsenic atoms. Since atomic diffusion on the Group-V sublattice is inconsequential, the intermixing of heterojunctions depends only on the diffusion of gallium and aluminum atoms on the Group-III sublattice.

Diffusion of the atoms on the Group-III sublattice occurs via defects in the lattice. Some important defects are shown in Figure 2.1 (a). The vacancy ( $V_{III}$ ) is an empty lattice site, the interstitial defect ( $I_{III}$ ) is an atom belonging to the Group-III sublattice that is not at a lattice site, and the substitutional defect can be either a Group-III atom in the Group-V sublattice ( $III_V$ ) or vice-versa ( $As_{III}$ ). These basic defects are combined to make other, more complex defects. For example, a Frenkel Pair is an interstitial atom which is associated with a nearby vacancy where that atom should be. The diffusion process via Group-III vacancies occurs when a  $V_{III}$  is filled with an aluminum or gallium atom from the nearest Group-III lattice point, or it may be filled from a passing interstitial atom. Group-III interstitials,  $I_{III}$ , on the other hand, move about the lattice until switching places with an atom in a Group-III lattice site, thereby creating another  $I_{III}$ , which may be an  $I_{Ga}$  or an  $I_{Al}$ . The substitutional, or antisite, defect process involves, for instance,  $As_{III}$  which migrates through the crystal, being replaced by either  $Ga_{III}$  or  $Al_{III}$  as it leaves each lattice site. Some interdiffusion mechanisms are shown in Figure 2.1 (b). The rate at which the atoms diffuse depends on the equilibrium concentration of defects. Assuming that interstitial atoms and vacancies are the dominating defects, their concentrations are denoted by  $[I_{III}]$  and  $[V_{III}]$ , respectively. The diffusion coefficient,  $D_{III}$ , can then be described by the simplified model<sup>[22]</sup>

$$D_{III} = f_1 D_{V_{III}} [V_{III}] + f_2 D_{I_{III}} [I_{III}] \quad (2.1)$$

where  $f_1$  and  $f_2$  contain information about the crystal structure,  $D_{V_{III}}$  is the Group-III vacancy diffusion rate, and  $D_{I_{III}}$  is the Group-III interstitial diffusion rate. By

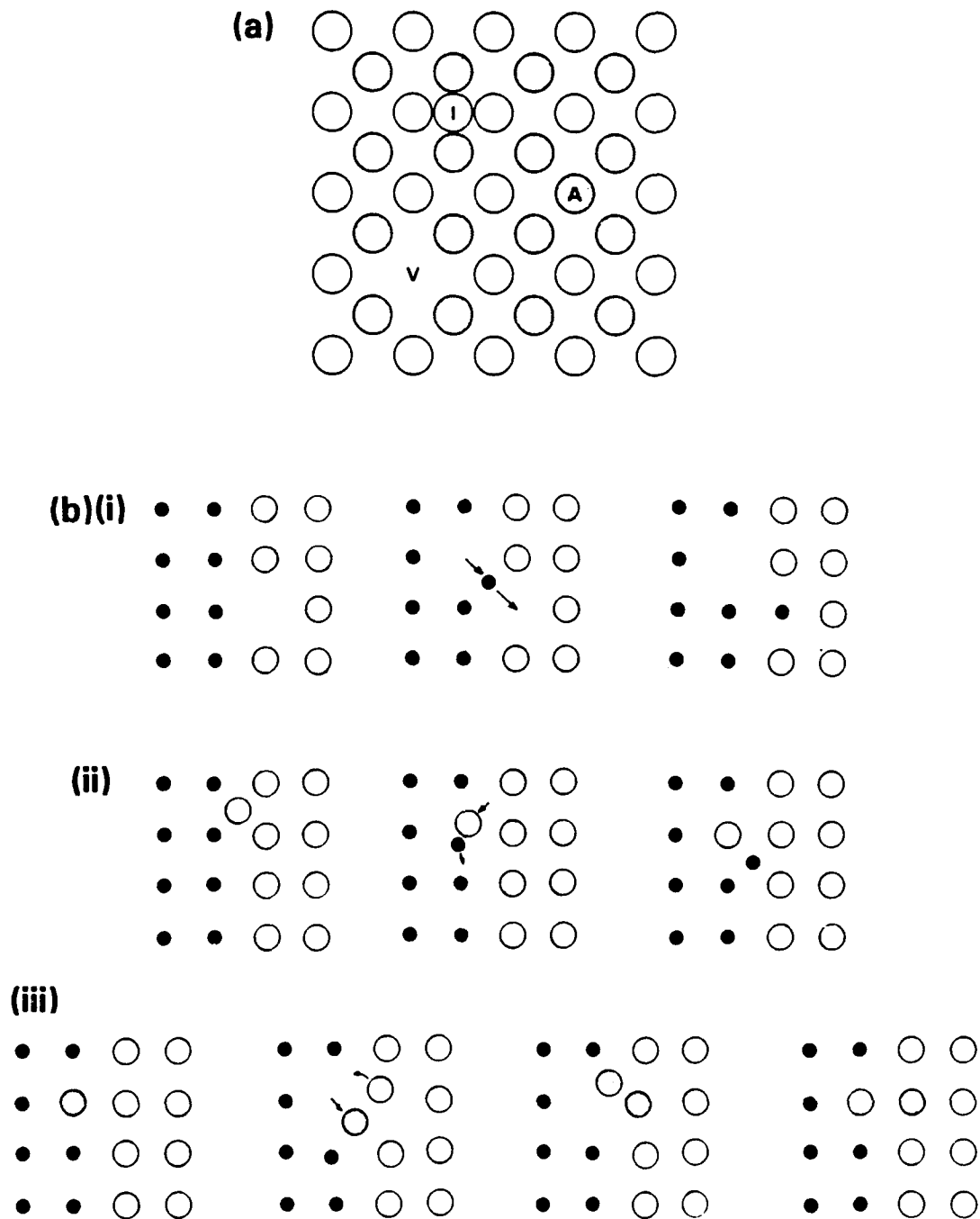


**Figure 2.1** Schematic of the interdiffusion process. (a) The major point defects are shown, including the Group-III vacancy ( $V_{III}$ ) and interstitial ( $I_{III}$ ), and the antisite defects  $As_{III}$  (shaded circle). (b) Schematic of (i) vacancy, (ii) interstitial, and (iii) antisite interdiffusion processes. The filled circles can be considered to be gallium atoms, the open circles aluminum, and shaded circles arsenic. Only the Group-III sublattice is depicted.

controlling  $[V_{III}]$  or  $[I_{III}]$ , the diffusion coefficient can be controlled. This can be done by adjusting the crystal Fermi level<sup>[23,24]</sup> with impurities, or by controlling the stoichiometry of the crystal near the surface with various overpressures.<sup>[14]</sup>

Because  $V_{III}$ 's are negatively charged, the concentration of vacancies tends to follow the concentration of donor impurities, or more precisely, the crystal Fermi level. Since ionized donors are positively charged, more vacancies will be created by the crystal in order to preserve charge neutrality. The argument is similar for negatively-charged ionized acceptors and positively-charged interstitial defects. Tan *et al.* recently published a review in which they claim that Al-Ga interdiffusion is controlled by triply negative Group-III vacancies,  $V_{III}^{3-}$ , under intrinsic and n-type conditions, while the doubly-positive Group-III interstitial,  $I_{III}^{2+}$ , dominates for heavy p-type doping.<sup>[25]</sup> Baroff and Schluter, however, predicted that the arsenic antisite defect  $As_{III}^+$ , a stable donor in p-type GaAs, was the dominant defect.<sup>[26]</sup> In the same review by Tan *et al.*, data from several authors were compiled which resulted in the intrinsic gallium self-diffusion coefficient of

$$D_{Ga} = D_0 e^{-\frac{Q}{k_B T}} \quad (2.2)$$

where  $D_0 = 2.9 \times 10^8 \text{ cm}^2 \text{s}^{-1}$  and the activation energy  $Q = 6 \text{ eV}$ . Earlier work by Goldstein determined that the coefficients for self-diffusion were  $D_0 = 10^7 \text{ cm}^2 \text{s}^{-1}$ , and  $Q = 5.6 \text{ eV}$  for temperatures between 1100 and 1200°C.<sup>[27]</sup> The Ga-Al interdiffusion coefficient is a function of aluminum composition, as was shown in the early work of Chang and Koma,<sup>[28]</sup> but most authors, including Tan *et al.* take the gallium self-diffusion coefficient as the Ga-Al interdiffusion coefficient.

The dominant diffusion mechanism near the surface (within a few microns) can be controlled to some extent by controlling the conditions at the surface of the semiconductor. This is done by annealing the semiconductor in an environment with an

overpressure of gallium or arsenic. Hsieh *et al.* showed that the interdiffusion coefficient was enhanced when annealed in an arsenic overpressure, while interdiffusion was suppressed when annealed in a gallium overpressure.<sup>[12]</sup> For the case of arsenic overpressure, where the surface stoichiometry is preserved during the annealing process, the parameters that fit Equation (2.2) were  $D_0 = 4.4 \times 10^9 \text{ cm}^2 \cdot \text{s}^{-1}$ , and  $Q = 6.2 \text{ eV}$ . This data is shown in Figure 2.2.

A unique method of enhancing the interdiffusion coefficient was reported by Hwang *et al.*<sup>[29]</sup> in which they grew a GaAs buffer layer by molecular beam epitaxy at low substrate temperature (200°C). This layer is highly resistive and optically inactive due to the incorporation of excess arsenic.<sup>[30]</sup> The arsenic then acts as an effective arsenic overpressure which enhances the interdiffusion process.

In addition to the presence of the overpressure, the amount of overpressure is also important. Guido *et al.* measured the interdiffusion coefficient for As<sub>4</sub>-overpressures ranging from 0.1 atm to 10 atm.<sup>[14]</sup> Hsieh performed a similar experiment in which the gallium source weight was varied (the actual pressure is difficult to determine since part of the source remains liquid), and he showed that a minimum occurs in the interdiffusion coefficient for a 10 mg source in a 3- to 4-cm<sup>3</sup> volume at 914°C.<sup>[31]</sup> Both curves are reproduced in Figure 2.3.

The rate of interdiffusion of heterostructures can also be controlled to some degree by passivation of the surface with a dielectric such as SiN<sub>x</sub> or SiO<sub>2</sub>. Hsieh performed a diffusion study which indicated that the interdiffusion for temperatures below 850°C was effectively stopped when the wafer was encapsulated with a SiN<sub>x</sub> layer 1000 Å thick.<sup>[31]</sup> This method preserves the stoichiometry of the surface, which limits the generation of excess point defects (gallium vacancies) in the crystal.

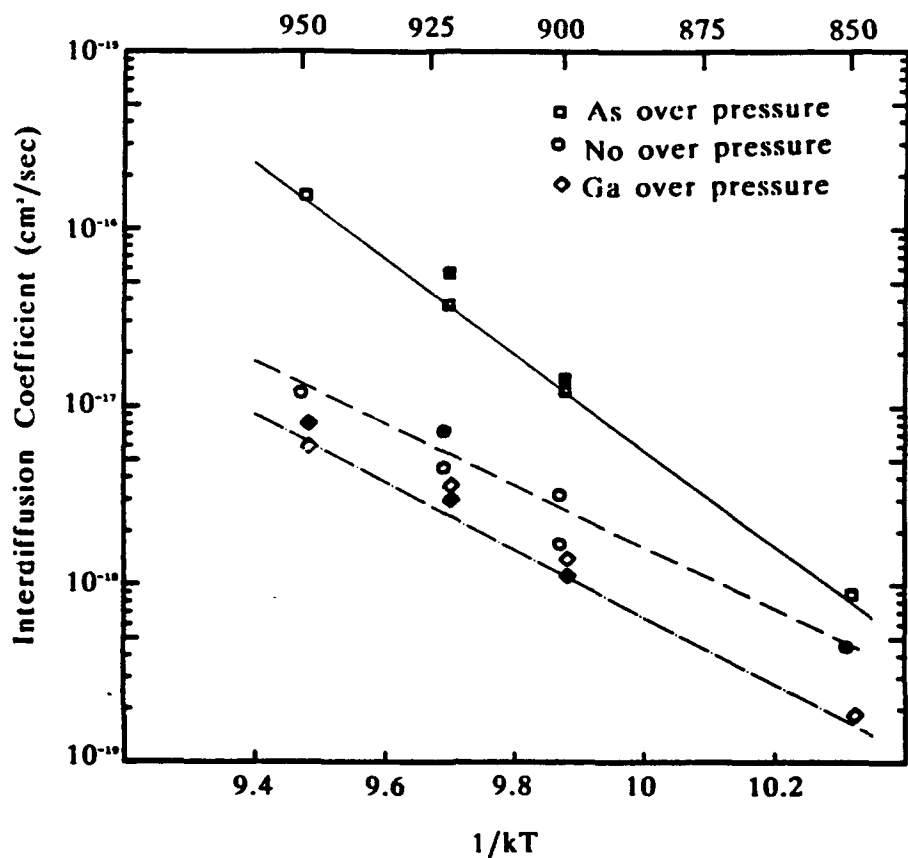


**Figure 2.2** Al-Ga interdiffusion coefficient as a function of annealing environment. The data is keyed as follows: square, arsenic overpressure; circle, no overpressure; diamond, gallium overpressure.<sup>[31]</sup>

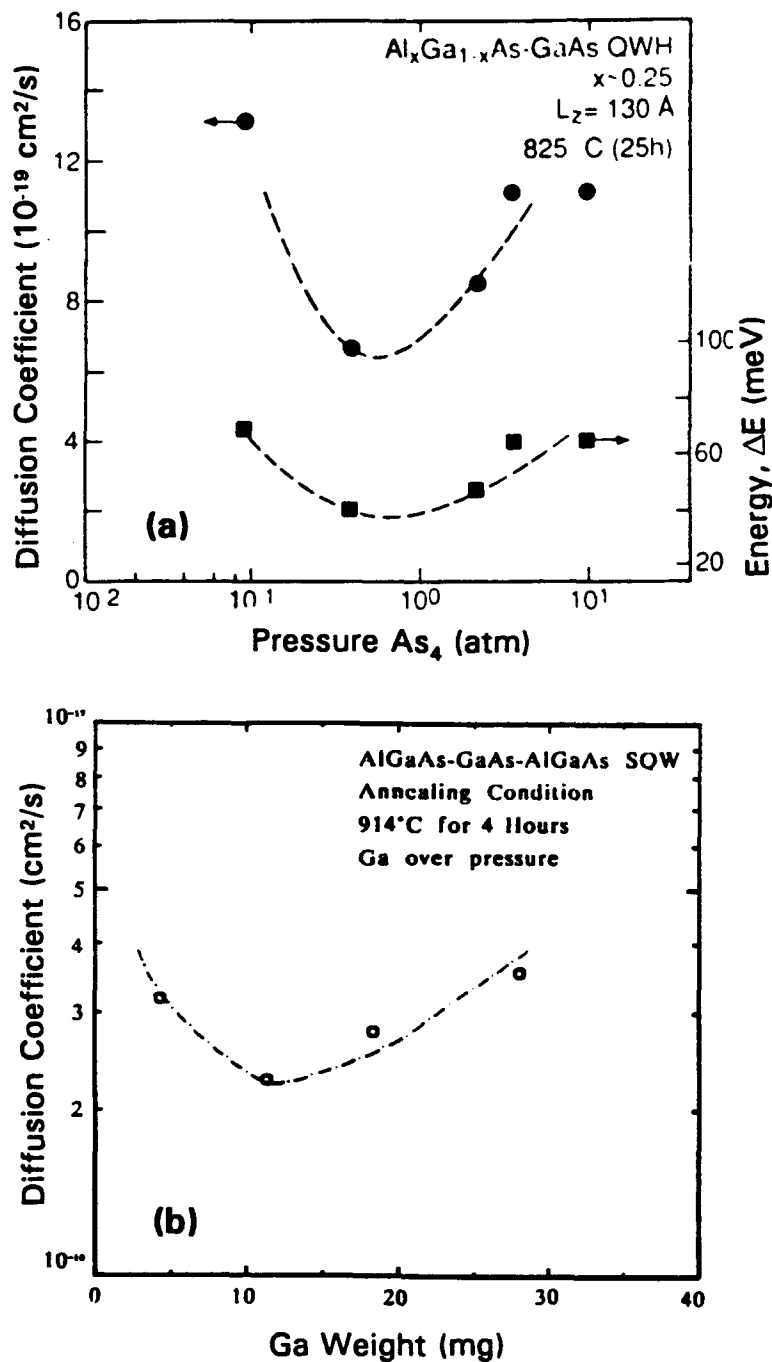


**Figure 2.3** Al-Ga interdiffusion coefficient as a function of overpressure source quantity. For arsenic overpressure (a), the interdiffusion coefficient is minimized near 1 atm (solid circles),<sup>[14]</sup> while a minimum for gallium overpressure (b) occurs for approximately 10 mg of gallium in a sealed quartz ampoule with a volume of 3-4 cm<sup>3</sup>. Gallium weight is used in (b) since all the gallium does not vaporize, so the exact overpressure is unknown.<sup>[31]</sup>

Deppe *et al.* examined both  $\text{SiN}_x$  and  $\text{SiO}_2$  as encapsulants and found that while the  $\text{SiN}_x$  was a good mask for the introduction of defects at the surface,  $\text{SiO}_2$  was a source of defects ( $V_{\text{Ga}}$ ) since the  $\text{SiO}_2$  absorbed gallium from the crystal.<sup>[32]</sup> Select areas of a wafer containing a superlattice were covered with  $\text{SiN}_x$ , then  $\text{SiO}_2$  was deposited on the entire surface. After annealing, they found that the  $\text{SiN}_x$ -covered superlattices were preserved, while the  $\text{SiO}_2$ -covered areas were intermixed. Guido *et al.*<sup>[14]</sup> performed a similar study with  $\text{SiO}_2$  as an encapsulant. They found that the dielectric acted as a source for silicon impurities if the heterostructure was too close to the surface of the wafer, thereby increasing the interdiffusion rate. Hsieh suspected the same problem from  $\text{SiN}_x$  at temperatures above  $850^\circ\text{C}$ , but didn't rule out the possibility of strain effects which arise from the different thermal expansion coefficients of the substrate and the encapsulant. In the paper by Guido *et al.*,<sup>[14]</sup> a stress field at the edge of the dielectric mask was determined to be the cause of enhanced interdiffusion. Kasahara *et al.*<sup>[33]</sup> also showed that the rate of silicon diffusion into GaAs was dependent on strain due to the thickness of the encapsulant.

Controlling the interdiffusion rate via a technique which generates defects at the surface raises the question of how fast those defects are transported to the layered structure. Guido *et al.* showed that the interdiffusion rate of a heterostructure is dependent on the depth of a structure from the surface.<sup>[34]</sup> The structures were annealed in 2 atm  $\text{As}_4$  overpressure at  $825^\circ\text{C}$ , and the diffusion coefficient for the  $V_{\text{III}}$  was  $D_{V_{\text{III}}} = 5 \times 10^{-12} \text{ cm}^2\text{s}^{-1}$ . A similar result was reported by Koteles *et al.* with samples that were capped with  $\text{SiO}_2$  and rapid-thermal annealed in a nitrogen atmosphere at 800 to  $900^\circ\text{C}$  for 15 seconds.<sup>[35]</sup> They showed that a coupled quantum well exhibited asymmetric interdiffusion after the annealing step, and proposed that it was due to the unidirectional diffusion of vacancies generated near the surface.

One way to control the location from which the defects are generated is to implant constituent atoms into the semiconductor to generate internal "overpressures." By using the same atoms as the host for implantation, impurity effects in the final device are avoided. The intermixing mechanisms depend on defects from both excess atoms (interstitials) and damage from collisions. Hirayama *et al.*<sup>[36]</sup> performed a study of gallium implantation into GaAs/AlGaAs in which they found the intermixing to be a function of ion dose. The structures studied were within 60 nm of the surface, and implant energy was 100 keV. This energy corresponded to about 35 nm penetration depth, so the ions were implanted into the structures. For low doses (less than  $10^{14} \text{ cm}^{-2}$ ), both implant damage and stoichiometric disturbances were important, while implantation damage dominated for higher doses. The ion dose used by Hirayama was from  $10^{12}$  to  $10^{16} \text{ cm}^{-2}$ , most of which was in the quantum well structure, making the excess gallium concentration on the order of  $10^{20} \text{ cm}^{-3}$ . At that level, the Group-III interstitials (primarily  $I_{\text{Ga}}$ ), and  $\text{Ga}_A$  antisite defects are the most probable sources for enhanced intermixing.

Cibert *et al.* did a similar study in which  $\text{Ga}^+$  ions were implanted at 210 keV with doses of  $5 \times 10^{12} \text{ cm}^{-2}$  to  $5 \times 10^{13} \text{ cm}^{-2}$  which resulted in an excess gallium concentration of  $6 \times 10^{17} \text{ cm}^{-3}$  to  $6 \times 10^{18} \text{ cm}^{-3}$ , respectively, centered on the heterostructure under study.<sup>[16]</sup> Subsequent rapid thermal annealing (RTA) steps at 950°C showed an increase in the Al-Ga interdiffusion coefficient of up to two orders of magnitude compared to the un-implanted regions at the beginning of the RTA. After the first 15-second RTA step, the interdiffusion coefficient in the implanted structures began to decrease again. The implantation generated vacancies, interstitials, and defect complexes which were annealed out, thereby reducing the defects responsible for the enhanced interdiffusion.

While the previous examples of ion implantation deal with ions (and hence damage) placed at the layer interfaces, Elman *et al.* studied the effect of ions implanted away from the structure.<sup>[37]</sup> In this experiment, the layers were buried approximately 3000 Å from the surface and low energy As<sup>+</sup> ions were implanted approximately 160 Å from the surface using a low implant energy of 35 keV in doses of  $5 \times 10^{13} \text{ cm}^{-2}$  to  $5 \times 10^{15} \text{ cm}^{-2}$ . Ion doses of  $2 \times 10^{14} \text{ cm}^{-2}$  produced the largest Al-Ga interdiffusion coefficient, which was attributed to the generation of vacancies which diffused down to the layers. Above that dose, defect complexes were generated in the implanted region. These complexes had low mobilities compared to point defects, so they didn't reach the layers fast enough, and the interdiffusion coefficient was gradually reduced as the dose was increased.

In order to create useful devices for integrated optics, a method of selectively disordering regions of quantum semiconductor structures without creating light-scattering or absorption centers must be developed. The underlying task in selective disordering is to locally control the concentration of point defects around the quantum well. There are several ways to do this. The first method is impurity-enhanced diffusion, either by thermal diffusion<sup>[9,38]</sup> or ion implantation<sup>[39,40]</sup> of impurities with the regions to be preserved masked. In impurity-induced disordered structures, however, the optical absorption due to impurities is high compared to undoped heterostructures. Although this is not a problem for lasers, which are lossy by their very nature, losses must be reduced in passive waveguides in order to make integrated optics a viable technology. For this reason, the use of host-type atoms to control intermixing such as applying local gallium or arsenic overpressure needs further study. By using these constituent atoms as an overpressure or implant source, impurity effects in the final device are avoided.

Selective layer intermixing (SLI) using IILD is well documented (see the review by Burnham *et al.*,<sup>[41]</sup> for instance), but work on impurity-free SLI is only beginning. In early work, Deppe *et al.*<sup>[32]</sup> demonstrated a stripe-geometry laser with active regions laterally defined by defect diffusion. In that case, 11- $\frac{3}{4}$  m SiN<sub>x</sub> stripes were used to protect the surface from SiO<sub>2</sub> which was deposited on the surface. During the annealing process, gallium vacancies were generated at the GaAs-SiO<sub>2</sub> interface, which diffused down to a superlattice. These regions were intermixed more than under the stripes, resulting in a higher bandgap than under the SiN<sub>x</sub>, thereby confining the carriers and, to some extent, the optical field in the active region.

Gallium or arsenic ions can also be used to delineate structures either by masking and implanting ions into the surface, or by direct-writing of the ions using a focused ion beam. Hirayama *et al.* claimed to have fabricated selectively disordered quantum wells with lateral dimensions of the preserved strips small enough to quantize the carriers in a second dimension, thus creating a quantum wire.<sup>[42]</sup> They used a 100 keV gallium focused ion beam to write 1000 Å lines separated by 2000 Å using doses from  $1 \times 10^{14}$  cm<sup>-2</sup> to  $2 \times 10^{14}$  cm<sup>-2</sup>. A thermal annealing step at 750 to 800°C for 60 minutes resulted in a lateral spreading of the disordered region of several hundred angstroms in each direction. Photoluminescence excitation was used to identify the quantized states resulting from the lateral confinement.

### 2.1.2 Intermixed Heterostructure Potential Wells

The shape of the potential of a heterostructure is defined by the bandgaps of the materials comprising its layers. For instance a quantum well defined by a thin GaAs layer surrounded by AlAs barriers has a potential well in the conduction band which has a depth defined by the difference between the  $\Gamma$ -bandgaps of the GaAs and AlAs, scaled by the band offset between the two materials. The valence band also has a

potential well for the holes with a depth given by the bandgap difference scaled by the valence band offset. When the interfaces of these materials are intermixed by the processes described above, they become graded in composition, which changes the abrupt, square quantum well to a well with a graded potential as depicted in Figure 2.4. The shape of this modified well depends on the diffusion coefficient, which, in general, is a function of both the temperature and the composition of the diffusing atoms.

The concentration profile of the intermixed quantum well can be found by solving Fick's Second Law, which is given by<sup>[43]</sup>

$$\frac{\partial C(z, t)}{\partial t} = \frac{\partial}{\partial z} \left( D(C, T) \frac{\partial C(z, t)}{\partial z} \right) , \quad (2.3)$$

where  $C(z, t)$  is the composition of aluminum in the  $z$  direction (perpendicular to the layers),  $t$  is time,  $D(C, T)$  is the diffusion coefficient and  $T$  is the diffusion temperature. In general, the derivative of  $D$  must be taken since  $D$  is related to  $z$  through the concentration. If this dependence is absent, then Equation (2.3) becomes

$$\frac{\partial C(z)}{\partial t} = D(T) \frac{\partial^2 C(z)}{\partial z^2} . \quad (2.4)$$

The solution to Equation (2.4) for a single interface between two semi-infinite layers is the complementary error function ( $erfc$ ), which is given by

$$C(z, t) = \frac{1}{2} C_0 erfc \frac{z}{2\sqrt{Dt}} \quad (2.5)$$

where  $C_0$  is the initial aluminum composition (or the difference in composition if the two layers have different aluminum compositions).

For a quantum well with two interfaces close enough for their composition profiles to cross, the results from the two semi-infinite layers are added with the origins of each case displaced by half the width of the well,  $L_z$ . The composition across a well centered at  $z = 0$  is then

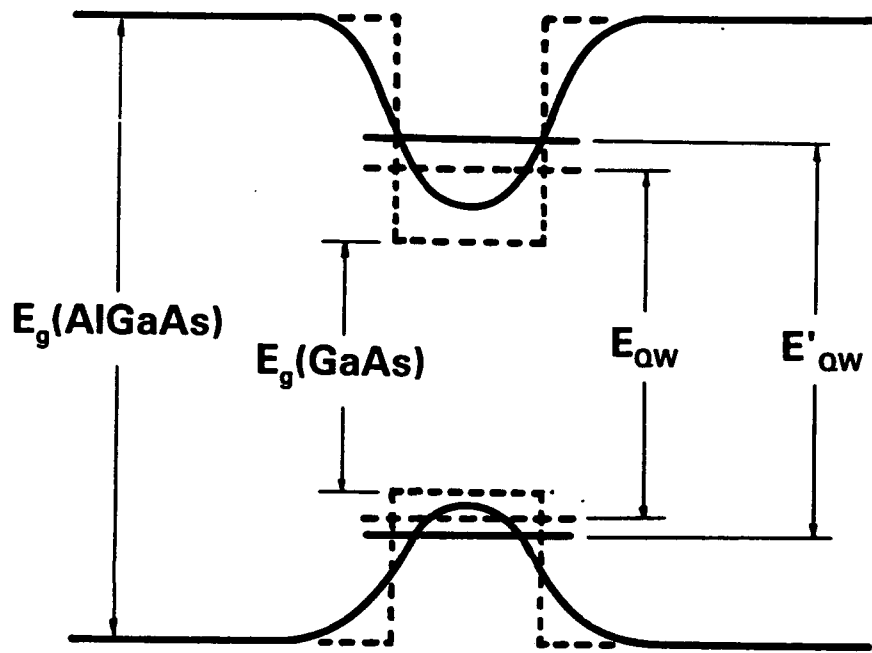


**Figure 2.4** Energy diagram of an intermixed GaAs/AlGaAs quantum well. The dotted lines represent the as-grown potential well with  $e_1$ - $hh_1$  transition labeled as  $E_{QW}$ . The solid line is the intermixed well with the new  $e_1$ - $hh_1$  transition,  $E'_{QW}$ .

$$C(z, t) = C_0 \left[ 1 + \frac{1}{2} \operatorname{erfc} \left( \frac{z + \frac{L_z}{2}}{2\sqrt{Dt}} \right) - \frac{1}{2} \operatorname{erfc} \left( \frac{z - \frac{L_z}{2}}{2\sqrt{Dt}} \right) \right]. \quad (2.6)$$

For a superlattice,  $C(z, t)$  is a superposition of all the interfaces in the structure.

While the diffusion coefficient is taken by many researchers as a constant with respect to aluminum composition, Chang and Koma showed that there is such a dependence, and their data is reproduced in Figure 2.5.<sup>[28]</sup> If the appropriate conditions are met, the Boltzmann-Matano method can be used to find  $D(C)$ .<sup>[44]</sup> Once this known, the composition profile can be found using a first-order Taylor series expansion<sup>[45]</sup> where

$$C(z, t_0 + \Delta t) = C(z, t_0) + \frac{\partial}{\partial z} \left( D(z) \frac{\partial C(z, t_0)}{\partial z} \right) \Delta t. \quad (2.7)$$

This is solved numerically for each position of  $z$ , then incremented by  $\Delta t$  until the total diffusion time is reached.

With the composition profile determined, the potential well profile is obtained by dividing the well into many layers, or regions, each of which has a bandgap characteristic of its average composition. The bandgaps are scaled by the appropriate band offset to yield a good approximation of the intermixed well potential. The remaining task is to determine the electronic properties of the new quantum well.

### ***Quantum Wells***

Solutions of bound states in finite, square quantum wells require either graphical or numerical techniques. One such method was developed by Kolbas and Holonyak in which energies are found by numerically solving the Schrödinger Wave Equation using the boundary conditions of the wavefunction and its derivative at the interfaces.<sup>[46]</sup> This method also provided information about the carrier envelope wavefunctions, and could

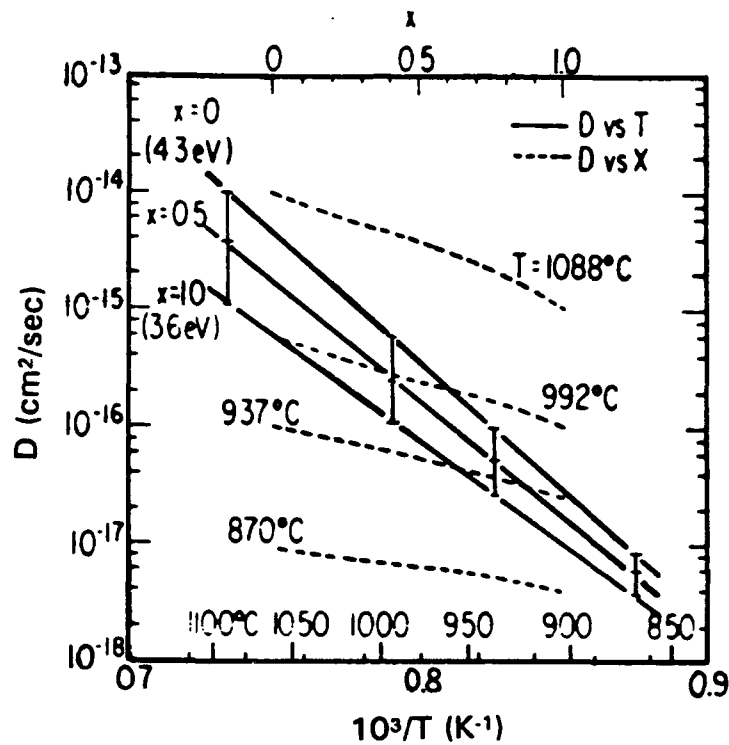


**Figure 2.5** Al-Ga interdiffusion coefficient as a function of temperature and aluminum composition. The solid lines indicate the range of the interdiffusion coefficient between GaAs (top line) and AlAs (bottom line). Each range at a specific temperature is indicated by a bar, and the interdiffusion coefficient as a function of aluminum composition (upper abscissa) is shown by the dotted lines.<sup>[28]</sup>

be extended to multiple wells with varying well depths and barrier heights. For solutions to disordered quantum wells, the potential well shape must be approximated by a finite number of layers with constant potentials.

To calculate the bound-state energy analytically, Camras *et al.*<sup>[47]</sup> used a modified Poschel-Teller potential<sup>[48]</sup> of the form

$$V(z) = \frac{\hbar^2}{2m^*} \lambda(\lambda - 1) \frac{\alpha^2}{\cosh^2(\alpha z)} , \quad (2.8)$$

Where  $m^*$  is the effective mass,  $\hbar$  is Planck's constant, and the other variables are defined below. Using the well depth from the error function profile as  $V(z = 0) = -\Delta E$ ,  $\lambda$  is determined by

$$\lambda = \frac{1}{2} + \sqrt{\frac{1}{4} + \frac{2m^* \Delta E}{\hbar^2 \alpha^2}} . \quad (2.9)$$

The other parameter,  $\alpha$ , is chosen such that the Poschel-Teller potential best fits the error function profile. The energy of the  $n^{\text{th}}$  bound state is then given as

$$E_n = -\frac{\hbar^2 \alpha^2}{2m^*} (\lambda - n)^2 ; \quad n \leq \lambda . \quad (2.10)$$

The advantage of this approximation is that it yields an analytical solution for the energies. The problem with this approach is that the Poschel-Teller potential is a good fit only for a well that has been intermixed to a great extent. For a well that has only been slightly intermixed, a more precise method is required.

In previous work, a "shooting" method<sup>[49]</sup> was employed to calculate the bound state of an error function quantum well.<sup>[31]</sup> Hsieh used this model where the wavefunction corresponding to a particular energy was found by numerically integrating the Schrödinger Wave Equation. The energy was adjusted until the wavefunction generated using the boundary conditions of the left-side of the well matched the wavefunction using the right-side boundary conditions, resulting in an

energy eigen state. In this model, the wave equation includes a factor which is a measure of the classical nature of the square-well potential,<sup>[50]</sup> and Hsieh assumed that the square-well factor was a good enough approximation for the error function profile. This factor was a function of well width, so as a well becomes more disordered, the well width is modified and this factor should be adjusted accordingly.

Another problem with the shooting method was discovered with ultrathin wells. Since the wavefunction of such a well has a large spatial extent, and this entire space is numerically evaluated, the actual well region accounts for only a small part of the total space. In order to keep the total number of divisions, and hence the computation time, reasonable, few divisions are left in the actual well which reduces the accuracy of the model.

### *Superlattices*

For superlattices the Kolbas-Holonyak approach is well-suited for a finite number of coupled square wells which have few divisions per period. To handle an intermixed superlattice, each period would have to be divided into many regions. This further limits the number of coupled wells the Kolbas-Holonyak model can accommodate due to practical computation considerations. Therefore, an alternate approach is required using a periodic potential. Two methods which have been used for square-well superlattices are the tight-binding approximation and the Kronig-Penney model.

The tight-binding calculations for superlattices in the envelope-function approximation have been limited to a simple square well basis.<sup>[51,52]</sup> A periodic potential,  $U(z)$ , is used where  $U(z) = U(z + r\alpha)$  with  $\alpha$  being the length of the period and  $r$  an integer.

With the single well potential and bound state energy given by  $V(z)$  and  $E_n$ , respectively, the dispersion relation is given by

$$E = E_n + \sum_{r=-\infty}^{\infty} e^{irqa} \int_{-\infty}^{\infty} \psi_n^*(z - r\alpha) [U(z) - V(z)] \psi_n(z) dz , \quad (2.11)$$

where  $\psi_n$  is the wavefunction of the bound state  $E_n$ , both of which are found using the single well calculation described earlier, and  $q$  is the superlattice wavevector. With nearest neighbor interactions only ( $r = 0, \pm 1$ ), this reduces to

$$E = E_n - \alpha - 2\beta \cos(q\alpha) , \quad (2.12)$$

where  $\alpha$  describes the integral in Equation (2.11) for  $r = 0$ , and is the shift to  $E_n$  due to the coulombic interaction of the coupled wells. The integral for  $r = \pm 1$  is described by  $\beta$ , which is the exchange energy that accounts for the broadening of the bound state into an energy band.

While the envelope function approximation is valid as long as the spatial extent of the wavefunction is large compared to the atomic spacing, it becomes invalid when a superlattice period is only a few atomic layers. For thin single wells, the wavefunction extends far into the barriers, making it large overall. But in a short-period superlattice, the wavefunction is periodic with the same period as the structure. In this case, an atomic tight-binding calculation is more appropriate, such as that done by Rucker *et al.*<sup>[53]</sup>

Another method to find the energy dispersion relation for a square-well superlattice is the Kronig-Penney model.<sup>[54]</sup> In the effective mass approximation this model gives an exact solution to the periodic square-well potential,<sup>[55]</sup> but for more than two layers, the usual method of solution becomes impractical. An approach described by Yuh and Wang<sup>[56]</sup> defines a  $2 \times 2$  transfer matrix for each layer in the basis, given by

$$S_i = \begin{bmatrix} \cos(k_i L_i) & \frac{m_i^*}{k_i} \sin(k_i L_i) \\ -\frac{k_i}{m_i^*} \sin(k_i L_i) & \cos(k_i L_i) \end{bmatrix} , \quad (2.13)$$

where  $i$  denotes the layer,  $L_i$  is the layer thickness, and

$$k_i = \frac{\sqrt{2m_i^*(E - V_i)}}{\hbar} . \quad (2.14)$$

The transfer matrices of each region are multiplied together to give the total matrix,  $S$ . Using  $\Gamma(z)$ , a vector with elements  $\Gamma_1(z) = \psi(z)$  and  $\Gamma_2(z) = \psi'(z)/m^*$ , the eigenvalues of  $S$  are found using

$$\Gamma(r + a) = S\Gamma(z) = \lambda I\Gamma(z) . \quad (2.15)$$

Along with the Bloch theory, which gives  $\lambda = e^{*iq_a}$ , we find

$$S_{11} + S_{22} = e^{iq_a} + e^{-iq_a} = 2\cos(qa) , \quad (2.16)$$

where  $q$  is the superlattice wavevector. If a simple two-layer basis is used, the result is the familiar Kronig-Penney solution.

## 2.2 Optical Properties of Semiconductor Quantum Structures

The optical properties of a semiconductor are contained in the complex dielectric constant,  $\epsilon(\omega)$ , which is given by

$$\epsilon(\omega) = \epsilon_1(\omega) + i\epsilon_2(\omega) . \quad (2.17)$$

Once either the real or imaginary part is known, the other part can be found using the Kramers-Kronig transformations.<sup>[57,58]</sup>

The usual method for determining the dielectric properties below the bandgap is to measure the reflectance at the surface to first obtain the index of refraction. This was performed for AlGaAs by Casey *et al.*<sup>[59]</sup> where the index was found for energies below as well as slightly above the bandgap. The extinction coefficient was neglected since it was still small and only gave an error of about 1% in the worst case. Aspnes *et al.* measured the complex reflectance ratio for various angles using a rotation analyzer spectroellipsometer, from which they calculated the real and imaginary parts of the

dielectric constant.<sup>[60]</sup>

Several empirically determined formulae exist for the index of refraction of AlGaAs below the bandgap,<sup>[61-63]</sup> one of which (given by Hunsperger) is

$$n^2 = A(x) + \frac{B}{\lambda_o^2 - C(x)} - D(x)\lambda_o^2 \quad , \quad (2.18)$$

where  $x$  is the aluminum fraction in the  $\text{Al}_x\text{Ga}_{1-x}\text{As}$  alloy,  $\lambda_o$  is the free-space wavelength in microns, and

$$A = 10.9060 - 02.92x$$

$$B = 0.97501$$

$$C = (0.52886 - 0.735x)^2 \quad ; x \leq 0.36$$

$$C = (0.30386 - 0.105x)^2 \quad ; x > 0.36$$

$$D = 0.002467(1 + 1.41x) \quad .$$

Recently, Jensen and Jensen presented a model in which the real index near the band edge can be calculated directly from experimentally available band structure parameters.<sup>[64]</sup>

To calculate the dielectric function, one usually starts with the imaginary part,  $\epsilon''(\omega)$ , which is proportional to the square of the optical matrix element and the joint density of the states for the electronic transitions.<sup>[21,65,66]</sup> Once  $\epsilon''$  is calculated,  $\epsilon'$  is found using the Kramers-Kronig transformations, then the index of refraction, extinction coefficient, or absorption coefficient may be determined.

An alternate method for calculating the dielectric constant is to treat the electronic system as a collection of oscillators and add the contributions of each. In this manner, both  $\epsilon'$  and  $\epsilon''$  are calculated separately since the energy spectrum is too narrow to accurately apply the Kramers-Kronig relations. Kahan and Leburton used such an approach<sup>[20]</sup> where they calculated the band structure using the Kane model,<sup>[67]</sup> then used the calculated properties of the band edges for the characteristics of the oscillators.

This method was later applied to superlattices and multiple quantum wells in which the energy dispersion in the quantized direction was given by a tight-binding-like expression.<sup>[19]</sup> The oscillator approach is well suited for calculating the dielectric constants of quantum wells as performed by Tsu and Ioriatti<sup>[68]</sup> since their energy levels are discrete.

In the oscillator approach, the complex dielectric constant for a system of  $N$  is

$$\epsilon(\omega) = \epsilon_0 + N \sum_j \frac{e^2}{m_0} \frac{f_j}{(\omega_j^2 - \omega^2) - i2\gamma_j\omega} . \quad (2.19)$$

The dielectric function is then the sum of the dielectric responses of all the oscillators in the atomic system, each with a resonant frequency,  $\omega_j$ , oscillator strength  $f_j$ , and damping coefficient  $\gamma_j$ . The oscillator strength is

$$f_j = \frac{2}{m_0 \hbar \omega_j} |M|^2 \quad (2.20)$$

where  $|M|^2$  is the momentum matrix element of the oscillator squared.

The properties of the quantum well are then dependent on the oscillator frequency, its damping coefficient and the matrix element. The frequency can be calculated by solving for the energy levels in the quantum well. This should also yield the envelope wavefunctions of the electron and hole states, which is useful for calculating the matrix element.

The matrix element for a single oscillator between two states,  $m$  and  $n$ , with a single polarization is

$$M_{mn} = \langle n | m \rangle P_{mn} \delta(\vec{k}_{n11} - \vec{k}_{m11}) \quad (2.21)$$

where  $\langle n | m \rangle$  is the overlap of the electron wavefunction in state  $n$  and hole wavefunction in state  $m$ .  $P_{mn}$  is the interband matrix element including the selection

rules, and the delta function conserves momentum in the directions parallel to the layers in the quantum well. The interband matrix element in III-V semiconductors for electron to heavy-hole (TE, transverse electric) transitions at  $k_z = 0$  is<sup>[69]</sup>

$$P_{mn} = -\frac{m_o}{j\hbar} P_o \sqrt{\frac{1}{4}} \quad (2.22)$$

where the factor of  $\frac{1}{4}$  comes from  $\frac{1}{2}$  for the average over all directions ( $\frac{1}{6}$  for bulk) and  $\frac{1}{2}$

for the conservation of spin<sup>[70]</sup> (since the transition can only occur to the band with the same spin).  $P_o$  is found using<sup>[67]</sup>

$$P_o^2 = \frac{m_o E_g}{2} \left( \frac{m_o}{m_c^*} - 1 \right) \frac{E_g + \Delta}{E_g + \frac{2}{3}\Delta} \quad (2.23)$$

where  $m_o$  is the free-electron mass,  $E_g$  is the bandgap energy,  $m_c^*$  is the conduction-band effective mass, and  $\Delta$  is the split-off energy for the split-off valence band. For GaAs at room temperature, the squared matrix element is estimated by Casey and Panish<sup>[71]</sup> as

$$|M_{bulk}|^2 = 1.33 m_o E_g, \quad (2.24)$$

the quantum well value being  $3/2 |M_{bulk}|^2$ . The value is generally considered to be constant between the materials of a heterostructure.<sup>[72]</sup>

The value for the damping coefficient can be measured from luminescence data,<sup>[73]</sup> where  $2\gamma = \Delta\omega$  is the full width at half maximum (FWHM) of the luminescence spectrum. The line-width broadening is due to the finite lifetimes of the electronic states and is related to the lifetime through the uncertainty relation  $\hbar\Delta\omega\tau \approx \hbar$ ,<sup>[74]</sup> where  $\tau$  is the lifetime of the excited state. The lifetime can be either measured or calculated, but if calculated, both radiative and non-radiative processes should be considered.

### 3 Experimental Methods

#### 3.1 Crystal Growth

The structures described in this work were grown by molecular beam epitaxy (MBE). The MBE system used is a commercial Varian 360. Since the emphasis of this study is to ascertain the effects of thermal processing on the optical properties of quantum wells, the details of crystal growth are beyond the scope of this thesis. The interested reader is referred to an excellent description of the system by Andersen,<sup>[75]</sup> but the sample preparation and growth conditions of the samples grown for this work are specified below.

The samples are prepared by degreasing, etching, and mounting them on molybdenum blocks. Unless otherwise stated, all substrates are semi-insulating (SI), (100)-oriented GaAs wafers. The substrates are degreased by rinsing for five minutes each in trichloroethane (TCE), acetone, and methanol in order, with a final rinse in deionized water (DI-H<sub>2</sub>O). The surface is then etched with a solution of 7:1:1 H<sub>2</sub>SO<sub>4</sub>:H<sub>2</sub>O<sub>2</sub>:H<sub>2</sub>O. The substrates are then mounted on the molybdenum blocks using molten indium, and immediately loaded into the preparation chamber of the MBE via a load-lock. The samples are then heated to outgas the surface, and just before beginning the growth of the epitaxial layers, the wafers are heated to 575°C in the growth chamber for five minutes under an arsenic overpressure to remove any oxide that may have formed on the surface.

The growth conditions consist of a combination of molecular beam fluxes, which are measured before and after layer growth, and substrate temperature, which is monitored during growth. The growth rates and alloy compositions are calibrated using calibration samples just prior to the growth of the desired structures. The crystal quality is determined using reflection-electron diffraction and is verified, along with

material composition, using photoluminescence spectroscopy. The substrate temperature is 200°C for low-temperature growth of GaAs. For the  $\text{Al}_x\text{Ga}_{1-x}\text{As}$  the temperature ranged from 640°C for GaAs to 700°C for AlAs, and the  $\text{In}_{0.2}\text{Ga}_{0.8}\text{As}$  is grown at 520°C.

### 3.2 Optical Characterization

The optical characterization performed in this study was photoluminescence spectroscopy. Two techniques used were standard (time-integrated) photoluminescence (PL) in which no temporal information was collected, and time-resolved photoluminescence (TPL) in which temporal data was taken with a resolution of about 15 ps. Both PL and TPL were used to examine the characteristics of the spontaneous emission of optically excited samples in order to probe their electronic structures.

The PL process shown in Figure 3.1 begins with the creation of electron-hole pairs in a semiconductor via the absorption of photons of energy higher than that of the electronic bandgap of the semiconductor. This process is referred to as photopumping the sample. The scattering times of the electrons (holes) within the conduction (valence) band are much shorter than the lifetime for the electrons and holes to recombine, so they quickly scatter to the conduction (valence) band edge before recombining. Momentum and energy is conserved as the carriers thermalize to the band edges through the emission of phonons. The carriers then recombine across the bandgap, emitting photons equal in energy to that of the gap, thereby conserving energy. If these photons are not re-absorbed, then they will escape from the sample, where they can be collected and detected. In the case of TPL, the excitation pulselwidth must also be much shorter than the recombination time in order to observe the temporal characteristics of the electronic system.

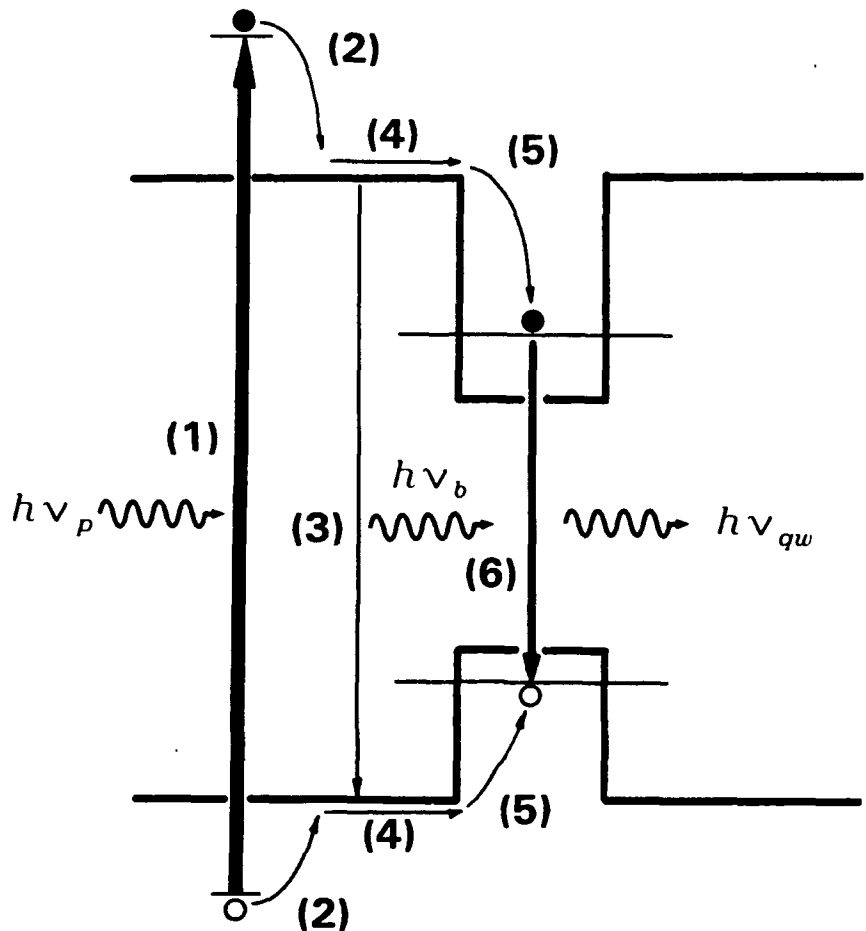


**Figure 3.1** The photoluminescence process. The sample is photopumped with photons of energy  $h\nu_p$  (1) creating an electron-hole pair. The carriers then thermalize to the band edges (2) where some recombine, giving off photons of energy  $h\nu_b$  (3) while others diffuse toward the well (4). The carriers are then captured by the well (5) where they thermalize to the bound states from which they recombine to give off photons of energy  $h\nu_{qw}$  (6).

The detection apparatus measures the intensity of the emitted photons as a function of wavelength, which is easily converted to energy. In the case of TPL, the temporal characteristics of the photon emission process is measured as well. The PL spectrum contains information about the electronic band structure of the structure, and the time-resolved data from TPL adds to it information about the carrier recombination lifetimes.

### ***3.2.1 Standard Photoluminescence (PL) Spectroscopy***

The standard (or time-integrated) PL system used a Coherent Inova 90 argon-ion laser with a Coherent 7208 cavity dumper to pump the samples. The laser is capable of 5 W of continuous wave (CW) laser power at the wavelength  $\lambda = 5145 \text{ \AA}$ , and is capable of much higher peak power when used in pulsed mode. The pulse rate is selected using a Model 7200 Cavity Dumper Driver, and the pulse width is approximately 4 ns full-width-at-half-maximum (FWHM). The lower power CW operation allows the photopumped electron-hole pairs in the sample to thermalize and recombine before the energy band fills up. Conversely, the pulsed mode concentrates more photons on the sample during the pulse so that radiative recombination from higher energy features can be detected, such as the barrier energy in a quantum well structure.

The samples are cleaved pieces of the original wafer, and measure from a few millimeters to as much as a centimeter on a side, and are mounted on a heat-sinking "plug." The plug is a solid copper cylinder with an indium cap soldered on top of it which is pressed flat to accept the sample. The sample is either pressed into the indium or is held in contact to the indium with radio-TV service cement. The plug is then bolted to a copper block which is attached to the bottom of a stainless steel dewar. The dewar then fits on top of a lighthouse, or a vacuum chamber with three quartz windows

which allow optical access to the isolated sample. The lighthouse is evacuated with a mechanical pump to less than 20 mTorr, and liquid nitrogen is poured into the dewar to cool the sample to 77K.

Light from the laser is focused to a spot size of about  $20 \frac{1}{4}$  m to  $100 \frac{1}{4}$  m on the sample's surface, which is held approximately  $20^\circ$  from normal incidence to the pump. The emitted light is collected  $90^\circ$  for the direction of the input beam (about  $70^\circ$  from the sample), the pump light is filtered out, and the remaining light is focused through the input slit of a 0.5-m Jerrel Ash Model 82-020 spectrometer with a dry-iced-cooled S-1 photomultiplier tube at 1000 V to detect the spectrally dispersed signal. The output of the photomultiplier is amplified by a Keithly 602 electrometer which drives a chart recorder to record the data.

### ***3.2.2 Time-Resolved Photoluminescence (TPL) Spectroscopy***

The basic apparatus for TPL is similar to that for standard PL except for the addition of a streak camera to measure the time response of the optical emission. Following is a brief description of the TPL system. A more detailed description with the theory of operation is given by Benjamin.<sup>[76]</sup>

The excitation source in this case is a Spectra Physics Model 375B dye laser which emits tunable laser radiation in 5- to 6-ps pulses at an 82 MHz repetition rate. The wavelength range of the dye laser is 6200 to 6900 Å using DCM dye, which is synchronously pumped by a frequency-doubled Model 3460 Nd:YAG laser. The Nd:YAG is mode-locked to produce 120-ps pulses at 1064 nm, which is then frequency-doubled to 85-ps pulses at 532 nm by passing through a KTP crystal. The final output of the laser system is monitored using a Spectra Physics Model 409 autocorrelator, which displays the pulselwidth on an oscilloscope.

Sample plugs are mounted on the cryotip of an Air Products closed-cycle helium refrigeration system (Model DE202 expander and Displex-type compressor). The refrigeration system is capable of holding the sample plug at between 15K and 300K, but all data in this study was taken at 77K. The excitation source is focused on the sample through a quartz window in a vacuum shroud that isolated the sample, which is held at approximately  $10^{-4}$  Torr via a mechanical pump. The sample luminescence emitted through a second quartz window is collected, collimated and focused on a spectrometer slit using a dual-lens system.

For spectral analysis, an Instruments SA DHR320S spectrometer with a 1200-grooves-per-millimeter diffraction grating is used. It employs a double-grating configuration to eliminate temporal broadening due to the optical path length difference existing in single-grating spectrometers, which can be on the order of the carrier lifetimes of the samples being studied.

The output of the spectrometer is collimated and focused onto the input slit of a Hamamatsu C1587 streak camera. The light is then focused on an S-1 photocathode where it is converted to an electron image. The electrons are accelerated by a mesh electrode into a deflecting electric field. A high-speed-ramp voltage, which is triggered by the excitation source via a high-speed detector, is applied to the deflecting plates, which sweeps the electron beam from top to bottom. The electron image is amplified by a microchannel plate, then strikes a phosphor screen, which displays temporal dispersion vertically, and spectral dispersion horizontally.

The phosphor image is sent to a Hamamatsu C1000 High Sensitivity Video Camera, which passes its video signal to a Hamamatsu C1098 Temporal Analyzer. The temporal analyzer displays the screen image on a video monitor, where a vertical

window representing a narrow spectral band can be selected for analysis. The intensity versus time data centered at various wavelengths is then stored in a Hewlett Packard 310 computer for analysis and presentation.

The time resolution of the streak camera is limited by the time spread of photoelectrons, spatial spread of the input slit and resolution of the readout system, and the deflection electric field. The total resolution is limited further by the time spread of the collection optics, and that of the trigger jitter for low-level signals where multiple integrations are performed. The total resolution of the detection system is approximately 15 ps, which is sufficient for measuring the temporal responses of the samples in this study, which range from about 150 ps to over 1000 ps.

### 3.3 Thermal Annealing

Thermal annealing of the quantum well structures results in intermixing the materials of the heterostructures at their interfaces. This process modifies the shape of the potential well, which in turn changes the optical and electronic properties of the structure. This phenomenon is the general focus of this thesis, and will be addressed in detail in later sections. The overall process to anneal a sample is to clean it and any source of overpressure, seal it with the overpressure source in an evacuated ampoule, heat it to the annealing temperature for a predetermined time, cool it, and remove it from the ampoule.

The first step in preparing the samples is to remove any indium that is on the back side of the wafer. This is done by mounting the sample top-down on a pre-cleaned glass slide using melted black (apiezon) wax. Large pieces of indium are then scraped off, and the remaining indium is etched off in HCl for 2-3 hours. The slides are rinsed,

then the wax is re-melted, and the samples are immersed in TCA to dissolve the remaining wax. The cleaning step for the samples consists of standard degreasing steps described in the section on Crystal Growth.

For anneals using arsenic, a solid piece of arsenic is loaded into a quartz tube, which is evacuated to  $10^{-5}$  Torr. The arsenic, which is dark from arsenic oxide, is then heated in excess of the sublimation temperature using a hydrogen-oxygen torch. The oxide is driven from the surface, along with the top layers of pure arsenic, leaving behind pure solid arsenic with a shiny, silver-colored surface. The sublimated material condenses at the opposite end of the ampoule, which is kept cool with a towel which is soaked with cool tap water. When the sample and the ampoule to be used in the anneal is ready, the arsenic is removed from the vacuum, cut and weighed, and loaded along with the prepared sample into the ampoule in which the annealing will take place. This way, the clean arsenic is exposed to the air for a minimal amount of time.

For anneals using a gallium overpressure, the gallium source must be crystallized first, since it is a liquid near room temperature with a melting point of 29°C. First, a beaker of gallium (99.9999%) is warmed to ensure it is a liquid, and the top layer is skimmed to remove any debris that may have fallen or adsorbed onto the surface during storage. A pre-cleaned microscope slide is then dipped into liquid nitrogen to cool it to well below the melting point of the gallium. The slide is then immersed in the liquid gallium, where the gallium crystallizes on the slide. If the slide is removed from the liquid just before the crystals warm and start to re-melt, large gallium crystals can be formed, measuring up to about 5 mm long and weighing as much as a gram. These crystals are hard and brittle, which makes them easy to handle and cleave into pieces of the desired size. As with the arsenic, the gallium sources are loaded into an ampoule with the sample and evacuated as soon as possible.

Both sources are cut with clean stainless steel razor blades, then weighed on a Seederer-Kohlbusch balance. If needed, the sources are re-cut and weighed several times until the required weight is obtained. For arsenic, that weight is determined by the desired overpressure (P), the annealing temperature (T), and volume of the sealed ampoule (V). Assuming that all the solid arsenic becomes a vapor at the annealing temperature, and at high temperatures (800 to 900°C), the  $\text{As}_4$  pressure is much higher than the  $\text{As}_2$  pressure, then the overpressure is composed of  $\text{As}_4$  with a molar weight (M) of  $4(74.922)$  g-mole $^{-1}$ . The weight (W) of the solid source is obtained using the Ideal Gas Law,

$$PV = nRT \quad , \quad (3.1)$$

where R is the gas constant and  $n = W / M$ . Because the smallest tare weight available in our lab is 5 mg, the length of the ampoule is easier to adjust than the weight in order to get the desired overpressure. In this study, all anneals involving arsenic overpressure were done at 850°C (1123K) with 1 atm  $\text{As}_4$ . Using a 15 mg source and an ampoule with an inside diameter of 7.5 mm, the length of the sealed ampoule is 10.4 cm. This size is small enough to handle easily, and large enough to minimize the error in the assumption that the ampoules are cylinders with flat ends.

For gallium overpressure experiments, the vapor pressure in the ampoule is difficult to ascertain, since part of the source remains a liquid at the annealing temperature. Since the intent of such an experiment in the context of this thesis was to minimize the interdiffusion rate at the interfaces, data reported by Hsieh<sup>[31]</sup> was used to determine the source weight for the minimum interdiffusion coefficient. In his work, Hsieh found that a source weight of 10 mg in an ampoule with a volume between 3-4 cm $^3$  yielded the minimum interdiffusion coefficient of about  $2 \times 10^{-19}$  cm $^2$ s $^{-1}$ . In this work, the volume used was about 1.5 times that used by Hsieh, so a source weight of 15 mg was used to yield the smallest interdiffusion coefficient. Although this

estimation is rather crude, halving or doubling the source weight resulted in less than a 50% increase in the interdiffusion coefficient. Also, gallium overpressure was used only in a proof-of-concept experiment where order-of-magnitude differences between gallium-, arsenic-, and no-overpressure anneals were being sought.

The ampoules into which the samples and sources were loaded are fashioned from 9-mm (outside diameter) quartz tubes. The tubes are approximately 15 inches long with one end sealed using a hydrogen-oxygen torch. The insides of the tubes are etched with 1:10 HF:DI-H<sub>2</sub>O for 10 minutes, and rinsed with DI-H<sub>2</sub>O. The tubes are dried and stored in a bakeout oven at 200°C. When needed, a tube is removed from the oven, the samples and source are loaded into it, and it is loaded onto the vacuum station to be evacuated.

Rough-pumping at the vacuum station is accomplished by a mechanical pump which achieves vacuums of about 40 mTorr. At that point, the mechanical pump is isolated from the ampoule, and a diffusion pump evacuates the ampoule to approximately 10<sup>-5</sup> Torr, where the ampoule can be sealed.

The ampoules are sealed in several steps. First, any water that has adsorbed onto the inside surface of the ampoule is driven off using a hydrogen flame. Next, if a source is being used, a dimple is made with the torch (now mixed with oxygen) near the end of the tube. The dimple keeps the source and samples separated while loading it into the furnace. Finally, the tube is collapsed at the appropriate length from the end until the ampoule is closed off from the rest of the tube. The torch is then used to separate the ampoule from the tube.

After carefully shaking the ampoule so that the source and samples are separated by the dimple and samples are top-side-up, it is loaded into a Lindberg Hevi-Duty 36" 3-zone furnace which has been set to the proper temperature. The ampoules are slid into the center zone where the temperature is monitored by a chromel-alumel

thermocouple connected to an Omega Model 660 Thermocouple Thermometer. After annealing for 30 minutes to 5 hours, the ampoule is removed from the furnace by pulling it to the edge and grasping it with a wet towel. The wet towel quenches one end of the ampoule (without the sample) onto which the vapors condense. The rest of the ampoule is then quenched under tap water. The ampoules are then cut and the samples are removed for characterization.

### 3.4 Device Processing

Device processing for this work consisted of fabricating stripes layers of either  $\text{SiN}_x$  or GaAs epitaxial layers grown at low substrate temperature (LT-GaAs).

The  $\text{SiN}_x$  film is deposited on GaAs wafers by plasma-enhanced chemical vapor deposition using an LFE Corporation Model PND-310 plasma nitride deposition system. Surface oxide is removed from the samples prior to nitride deposition by etching in HCl for 15 seconds, rinsing with DI- $\text{H}_2\text{O}$  for 2 minutes, dipping in  $\text{NH}_4\text{OH}:\text{DI-}\text{H}_2\text{O}$  (1:15) for 20 seconds, and then rinsing in DI- $\text{H}_2\text{O}$  for another 2 minutes. The samples are then loaded into the PND-301 vacuum chamber where they are heated to 300°C in a vacuum of less than 20 mTorr.  $\text{SiH}_4$  (1.7%, diluted with argon) is introduced with ultra high purity  $\text{N}_2$  into the chamber for deposition. A 100 W radio frequency (RF, 13.56 MHz) plasma is generated in the chamber for 5 minutes. Under ideal conditions, a 1000 Å-thick  $\text{Si}_3\text{N}_4$  film is deposited on the surface of the wafers.

The quality of the  $\text{SiN}_x$  is checked using a computer-controlled ellipsometer. The ellipsometer measures the thickness of the film and the index of refraction, which should be as close as possible to 2.02. The film is then checked under an optical microscope to ensure that the surface is clear of defects.

Standard photolithography is used to define stripes on both the  $\text{SiN}_x$  films and LT-GaAs. The samples are pre-baked at 120°C for 15 minutes to dehydrate the surface. Each sample is loaded on a Headway spinner fitted with a 0.5-inch vacuum chuck. One drop of AZ 1400-27 positive photoresist is deposited at the center of the sample, which is then spun at 4000 rpm for 40 seconds, resulting in a photoresist layer 1.35  $\mu\text{m}$  thick. The samples are then soft-baked at 90°C for 30 minutes to remove solvent from the photoresist.

After it is cool, each sample is loaded into a Karl Suss M4 mask aligner with the appropriate photoresist mask. There, the photoresist is exposed to ultraviolet light (310 nm) for 90 seconds. After exposure, the sample is removed and the photoresist is developed in one-part Shipley 351 developer diluted in five-parts DI- $\text{H}_2\text{O}$  for 24 seconds, followed by a rinse in DI- $\text{H}_2\text{O}$ . The patterns are inspected under an optical microscope fitted with a yellow filter to check the quality of the developing, and, if satisfactory, the photoresist is hard-baked at 120°C for 15 minutes.

The exposed  $\text{SiN}_x$  stripes are etched in a Technics Model PEII reactive ion plasma etcher. The samples are loaded into the chamber which is evacuated to less than 0.4 Torr, then  $\text{CF}_4$  (1.25 Torr) and  $\text{O}_2$  (0.05 Torr) are introduced. A 100-W RF plasma is generated in which the exposed  $\text{SiN}_x$  etches for 3 minutes (500-1000 Å per minute). After etching, the photoresist is removed in acetone with ultrasonic agitation for 5 minutes.

The stripes in LT-GaAs are delineated with a selective wet-chemical etch which stops at AlGaAs. The etchant is one drop of  $\text{NH}_4\text{OH}:\text{DI-}\text{H}_2\text{O}$  (1:20) in  $\text{H}_2\text{O}_2:\text{DI-}\text{H}_2\text{O}$  (22:100). Small amounts of  $\text{H}_2\text{O}_2:\text{DI-}\text{H}_2\text{O}$  are then added to adjust the pH to 7.0. The etch rate is approximately 40 Å per minute with constant stirring, and the LT-GaAs is completely removed when the stripes take on a blue color characteristic of AlGaAs. The photoresist is then removed in acetone as above.

### 3.5 Hall Mobility Measurements

The electron mobility in modulation-doped field effect transistor (MODFET) structures is measured using the Vander Paw-Hall technique. The samples are cleaved into 1-cm squares, and small indium dots are placed on the corners of the surface. Each sample is then loaded on a heater element in a vacuum chamber which is purged with nitrogen three times. With a small flow of nitrogen passing through the chamber to keep it at 1 atm pressure, the sample is heated to 400°C for 4 minutes to drive the indium into the surface and make on ohmic contact with the two-dimensional electron gas in the MODFET structure. After it is cool, the sample is removed from the chamber and the ohmic contacts are checked with a curve tracer.

Gold wire is soldered to the indium dots and the sample is loaded into the Hall mobility measurement system. The system consists of a Varian Model V 4005 electromagnet driven by a Varian Fieldial Mark I field regulated magnet power supply. Electric current is supplied by a Keithley Model 225 current source, and voltages are measured by an HP 3468A multimeter. The position and polarity of the current source is manually changed with a switch box, and the polarity of the magnetic field is manually switched from the power supply.

The measurements are made at 77K by pouring liquid nitrogen into the sample chamber. The applied magnetic field is 3 kG, and the current source ranges for 1  $\frac{3}{4}$  A to 1 mA. The voltages are read from the multimeter and entered on a data sheet. The data sheet contains formulae which reduce the data to sheet resistance, sheet charge density, and mobility.

In this study, the effects of annealing on the mobility was studied, so the indium dots were cleaved off to avoid the effects the indium would have in the annealing process. After annealing, the samples were 6.5 mm square, and the mobility measurement was performed again. To compensate for differences in the mobility due

to the different sized samples, several samples were measured at 1 cm and 6.5 mm without annealing, and the mobilities for the annealed samples were normalized to the pre-annealed condition.

All the above experiments were performed at the various facilities within Daniels Hall on the North Carolina State University campus. The results of these experiments are presented in the following chapters.

## 4 Heterostructure Intermixing

Before the effects of thermal disordering of quantum wells and superlattices can be characterized, an accurate method for computing the electronic structure of appropriately shaped potential wells must be developed. This chapter describes the computational models developed in this work which were used in the studies discussed in subsequent chapters.

### 4.1 Error Function Model for Intermixed Quantum Wells

The most convenient model of an intermixed layer interface uses the error-function-shaped composition profile. This solution assumes no aluminum composition dependence in the Al-Ga interdiffusion coefficient. The computer algorithm for this model which was originally used by this group was replaced with a faster, more accurate one in this work. The shape of the potential well is a function of the aluminum composition,  $x$ , which is a superposition of the error function profiles of each interface. Each interface is treated as the junction of two semi-infinite layers, then the profiles of each interface are added to give

$$C(z, t) = C_0 \left[ 1 + \frac{1}{2} \operatorname{erfc} \left( \frac{z + \frac{L_z}{2}}{2\sqrt{Dt}} \right) - \frac{1}{2} \operatorname{erfc} \left( \frac{z - \frac{L_z}{2}}{2\sqrt{Dt}} \right) \right] , \quad (4.1)$$

where  $z$  is the displacement measured in the direction perpendicular to the layers,  $t$  is the annealing time,  $C_0$  is the initial aluminum concentration,  $L_z$  is the initial well width (centered at  $z = 0$ ) and  $D$  is the interdiffusion coefficient. The result is depicted in Figure 4.1.

In order to calculate the bound states, the intermixed potential is divided into several regions, each described by a constant potential resulting from the average aluminum composition of that region. At this point, the well is approximated by a

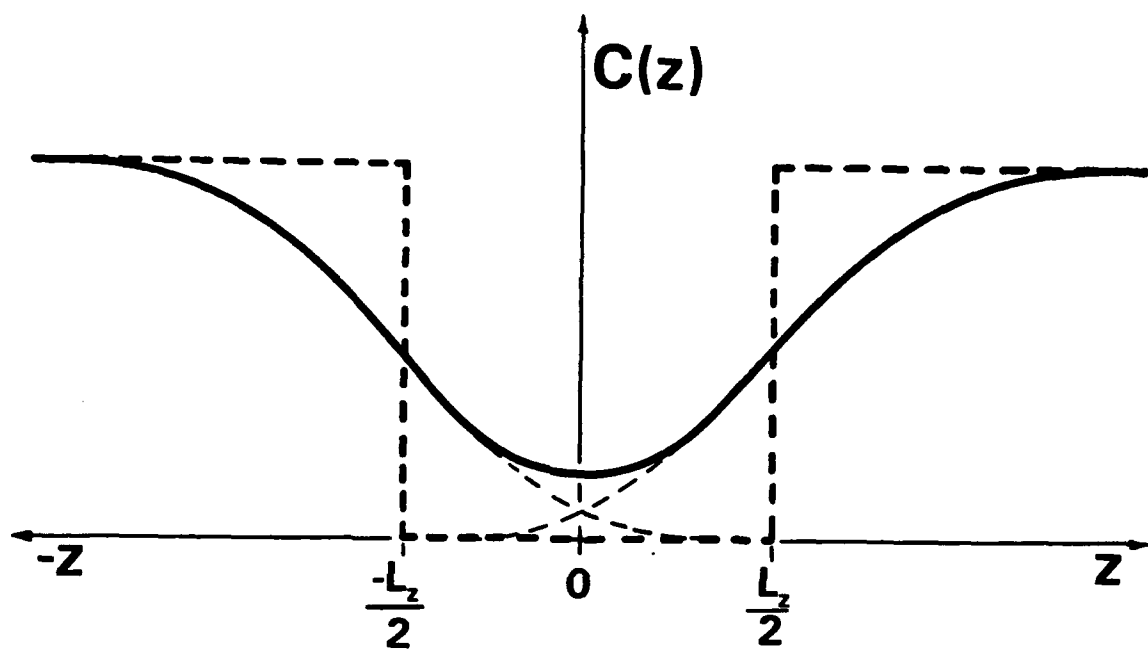


**Figure 4.1** Composition profile of an intermixed quantum well. The as-grown well is represented by the heavy dashed line. After annealing, the composition profile of the barriers spreads out, and is represented by the light dashed curves. These profiles are added, resulting in the composition profile given by the heavy solid line.

stair-step potential as seen in Figure 4.2. This information is then passed to a main program in the form of region widths and compositions. The bound state energy levels are then found by solving the Schrödinger Wave Equation using the boundary conditions of the wavefunction and its derivative at the region interfaces.

For a small number of regions in the well, the stair-step approach results in an error, which is reduced as the number of steps is increased. To keep that number reasonable, an iterative approach is used in which the bound states are calculated several times, doubling the number of regions in the well for each iteration. After a few iterations, the values start to converge to the answer which represents an infinite number of regions. An algorithm was employed which extrapolates the first few iterations to that final value.<sup>[7]</sup>

To speed up the convergence, a method was developed which concentrates more regions where the composition varies quickly (i.e., near the original heterojunction interfaces) rather than dividing the well into evenly spaced regions. This allows the calculation to converge to the bound state more quickly, as shown in Figure 4.3. The resulting speed advantage is exploited when bound states of many wells must be computed. Because this method is also more accurate for a finite number of regions, it yields a closer approximation to the actual bound state than a well evenly divided into the same number of regions. This new method is especially useful for occasions when a single iteration is used.

The transition energies between the conduction band electron state ( $e_n$ ) and the valence band states for heavy holes ( $hh_n$ ) or light holes ( $lh_n$ ) can be computed using the potential wells defined by the bandgaps of the material in each region. The bandgap of each region of  $Al_xGa_{1-x}As$  is given by

$$E_{gap} = 1.519 + 1.247x - \frac{5.405 \times 10^{-4}T^2}{T + 204} \quad , \quad (4.2)$$

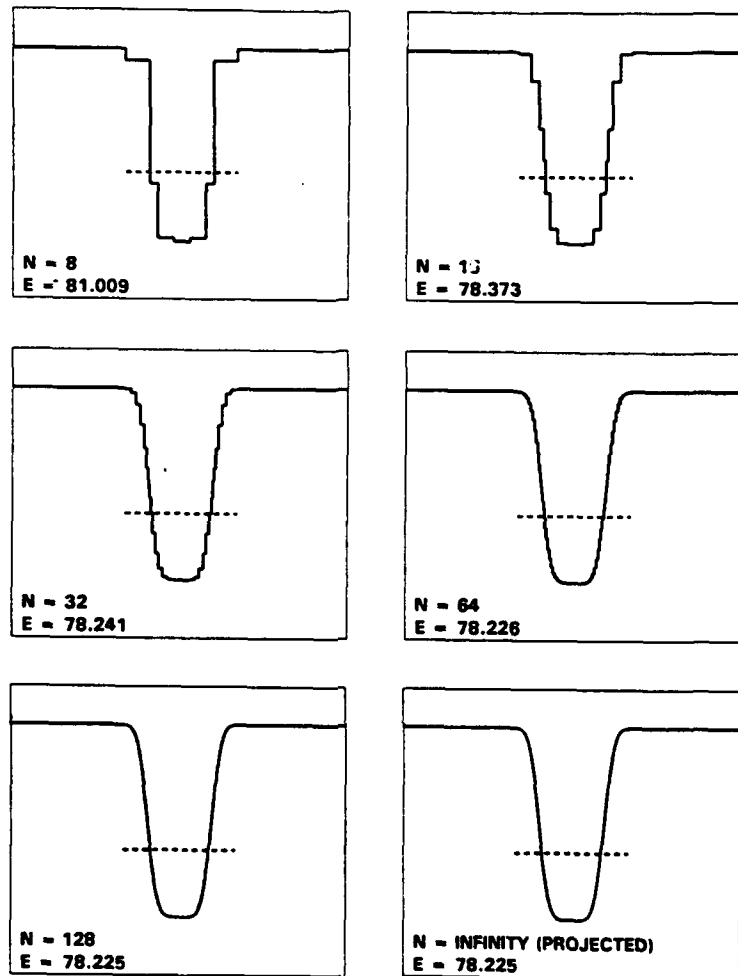


**Figure 4.2** Stair-step approximation to the intermixed quantum well. The initial approximation represents the intermixed well with 8 regions. Improvements to the calculation of the bound-state energies are achieved as the number of regions is doubled. The last frame shows the continuous profile with the projected solution to the bound-state energy for an infinite number of regions.

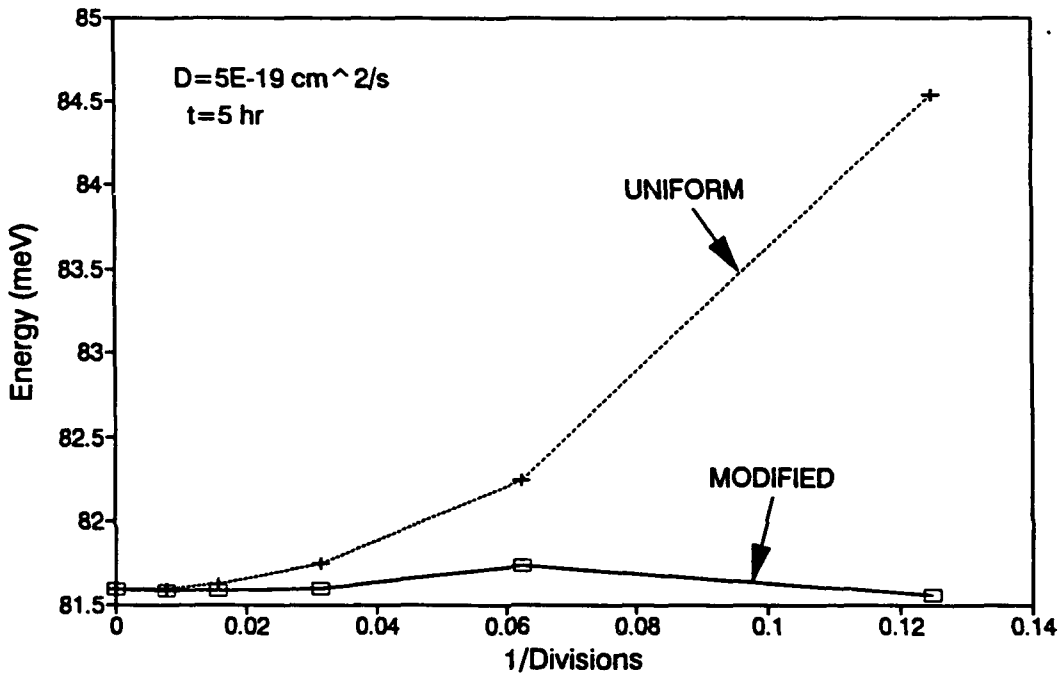


**Figure 4.3** Convergence of the calculated bound state for an intermixed quantum well. The dotted line represents the convergence for a well which is divided into uniform regions, while the solid line shows the improvement of the calculation when the regions are concentrated in areas where the composition changes rapidly in  $z$ .

and 60% of the bandgap difference between adjacent regions is assumed to be in the conduction band. This, along with the appropriate product of the interdiffusion coefficient and time, defines the potential well shape. The bound states for the electrons, heavy holes, and light holes are found separately using the following carrier effective masses,

$$\begin{aligned}m_e^* &= (0.0665 + 0.0835x)m_e, \\m_{hh}^* &= (0.45 + 0.302x)m_e, \\m_{lh}^* &= (0.08 + 0.057x)m_e.\end{aligned}\quad (4.3)$$

The gap between the wells is added to the electron and hole bound state energies in question to give the total transition energy between the conduction and valence band states, which is easily converted to a wavelength.

Using this method, the wavelength shift due to intermixing versus the well width for various times and temperatures was calculated and is presented in Figure 4.4. For thick wells, the shift was small, and as the width decreased, the shift increased. This can be explained as follows: as the well intermixes, the bottom of the well begins to fill from the edges. This causes the lowest state to be squeezed upward, which occurs faster for thinner wells. But for wells which were less than a few monolayers thick, the shift became small again, and in fact, the shift from single monolayer wells was almost negligible!

The reason for the reduced amount of shift is primarily because the lowest bound state is near the top of the well, which is actually getting wider as the well becomes disordered. This allows the state to relax to a lower energy with respect to the bottom of the well. On the other hand, the bottom is moving up in energy as the well fills in.

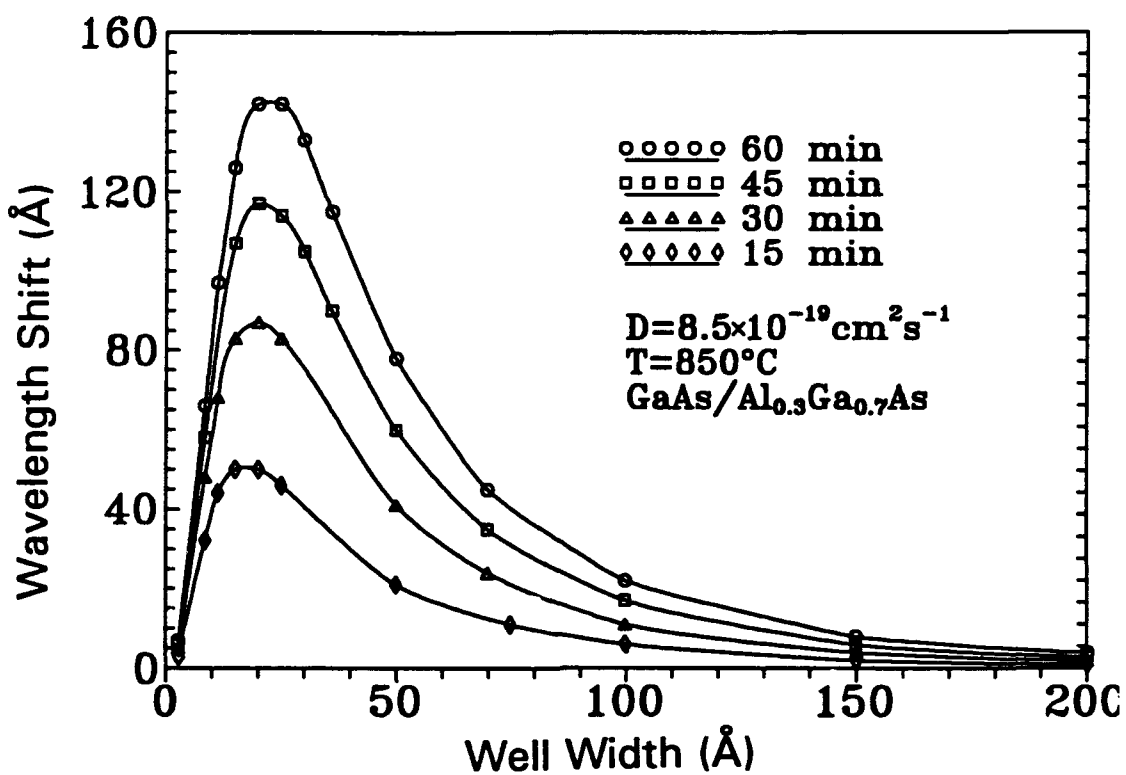


**Figure 4.4** Transition wavelength shifts for intermixed quantum wells as a function of well width. For large well widths, the shift is small since the bound states are near the bottom of the well, which takes a long time to fill as aluminum diffuses in from the barriers. For very thin wells, the bound state is pinned near the top of the well, so intermixing has little effect. Wells 10-50 Å thick, however, exhibit large shifts since the bound state is sensitive to the change in the potential well as aluminum diffuses in from the barriers.

These competing mechanisms yield a small net shift in wavelength. This result is important in designing optoelectronic devices which will be subjected to high temperature processing.

## 4.2 Compositional Dependence on the Interdiffusion Coefficient

While most of the recent work on intermixed GaAs/AlGaAs heterostructures uses an error-function-shaped composition profile, the early data by Chang and Koma<sup>[28]</sup> clearly shows a dependence of the interdiffusion coefficient on the aluminum composition in the AlGaAs alloy. They used Auger-electron profiling and the Boltzmann-Matano method of determining the composition-dependent interdiffusion coefficient,  $D(x, T)$ , to get

$$D(x, T) = D_0(x) e^{-\frac{Q}{k_B T}} \\ = 92 e^{-8.2x} e^{-\frac{4.3 - 0.7x}{k_B T}} \frac{\text{cm}^2}{\text{s}} \quad , \quad (4.4)$$

where  $x$  is the mole fraction of aluminum,  $k_B$  is Boltzmann's constant,  $T$  is the temperature in Kelvins, and  $Q$  is the activation energy in eV.

To model the composition profile resulting from a composition-dependent interdiffusion coefficient, the error function solution to Fick's Second Law is no longer valid. This is because the interdiffusion coefficient is no longer independent of displacement, and Fick's Law must be written more generally as

$$\frac{\partial C(z, t)}{\partial t} = \frac{\partial}{\partial z} \left( D(z) \frac{\partial C(z, t)}{\partial z} \right) . \quad (4.5)$$

Instead, the solution is found using the first-order Taylor series expansion,

$$C(z, t_0 + \Delta t) = C(z, t_0) + \frac{\partial}{\partial z} \left( D(z) \frac{\partial C(z, t_0)}{\partial z} \right) \Delta t , \quad (4.6)$$

where  $t_0$  is the initial time,  $\Delta t$  is the time increment, and  $D$  is the interdiffusion coefficient that depends on composition, and hence, depends on displacement as well.

In this case, the initial well profile is represented by many evenly-spaced points, each with a composition  $C$ . Starting at  $t_0 = 0$  and using an appropriate interdiffusion coefficient, the value of  $C$  for each point at  $t_0 + \Delta t$  is found. Resetting  $t_0$  to the current time ( $t_0 + \Delta t$ ), the algorithm is repeated. This continues until the time is incremented to the total diffusion time. As an example, the interdiffusion of a 40-Å  $\text{Al}_{0.35}\text{Ga}_{0.65}\text{As}$  quantum well for three hours at 850°C was modeled using Equation (4.4) for interdiffusion coefficient. The results appear in Figure 4.5. Also shown for comparison in Figure 4.5 is the case for a constant interdiffusion coefficient-error function profile using Equation (4.4) with  $x = 0$ . The difference in the wavelengths for the  $e_1\text{-hh}_1$  transitions was 15 Å.

Since the overpressure conditions and material quality were unknown in the experiments leading to Equation (4.5), an experiment was designed to determine: (1) if the concentration dependence is critical in this work, and (2) the magnitude of that dependence. Since the sizes of layers used here were too small to employ a method such as Auger-electron spectroscopy, the Boltzmann-Matano method could not be applied, and so another method was needed to determine the concentration dependence.

If the concentration dependence is exponential, then the diffusion coefficient is a function of the gallium and aluminum self-diffusion coefficients,  $D_{\text{Ga}}$  and  $D_{\text{Al}}$ , respectively, and is given by<sup>[78]</sup>

$$D(x) = D_a e^{\beta(x - \frac{1}{2})} \quad , \quad (4.7)$$

where

$$\beta = \ln\left(\frac{D_{\text{Al}}}{D_{\text{Ga}}}\right) \quad , \quad (4.8)$$

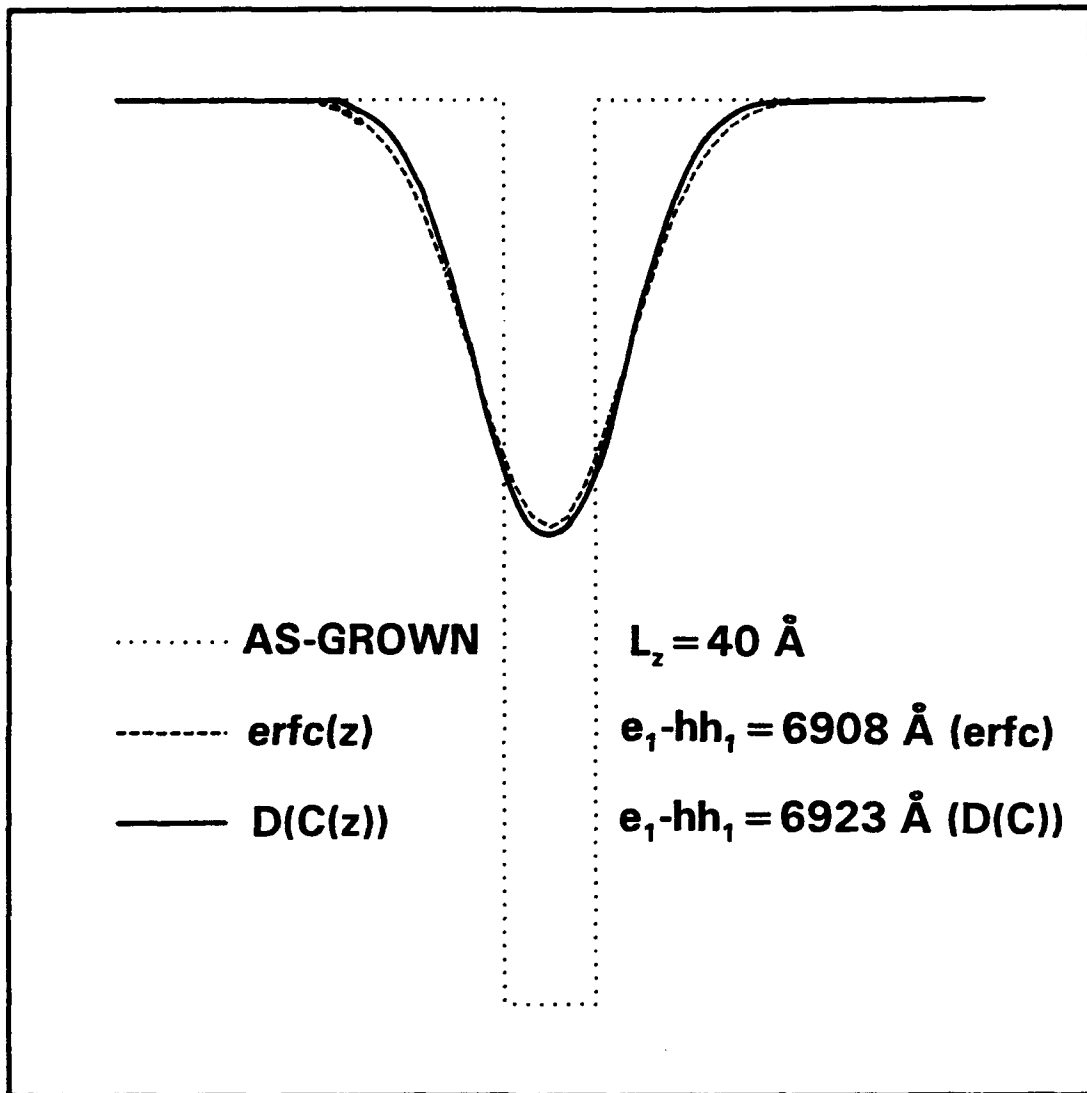


**Figure 4.5** Comparison of error function and composition-dependent diffusion of a GaAs/AlGaAs quantum well. The dashed line represents the conduction band potential well using a constant interdiffusion coefficient, while the solid line results from a composition-dependent interdiffusion coefficient. The initial well width was 40 Å and the barriers had 35% aluminum. Diffusion at 850°C for 3 hours was simulated, and the results showed a 15-Å difference in transition wavelength shifts.

and  $D_a$  is a constant for a given temperature. While  $D_{Ga}$  is well documented,<sup>[25]</sup> very little has been published on  $D_{Al}$ .

To determine if a significant aluminum composition dependence exists, an annealing experiment was designed in which the relative composition between the wells and barriers was held constant, while the absolute values were varied. If the interdiffusion coefficients were different for varying aluminum compositions using an error function analysis, then further investigation would be warranted to determine the actual composition dependence on the interdiffusion coefficient.

Three structures were grown with a nominally 10-monolayer (ML) (approximately 28 Å) quantum well of  $Al_xGa_{1-x}As$  with  $Al_yGa_{1-y}As$  barriers. The nominal composition values of (x,y) over (0,0.2), (0.1,0.3), and (0.2,0.4) for the three structures. The basic structure is shown in Figure 4.6. A 1000-Å well separated 500 Å from the 10-ML well was included in each to measure the actual well composition, since the n=1 bound state energy of such a well is negligible and does not change appreciably during the annealing steps in this study. After the wafers were grown, the compositions were checked using photoluminescence, and the (0,0.2) wafer was close to the nominal values, but the (0.1,0.3) wafer was closer to (0.1,0.35). No bound state or barrier luminescence was observed from the (0.2,0.4) wafer, and it was regrown only to produce the same results. This structure was therefore left out of the experiment, which proceeded with only the (0,0.2) and (0.1,0.35) structures.

Several samples were taken from each wafer. Their compositions and layer thicknesses were determined before annealing. The former was accomplished by measuring the barrier and 1000-Å well photoluminescence (PL) spectra. The layer thicknesses were determined by calculating the bound state of a quantum well with the

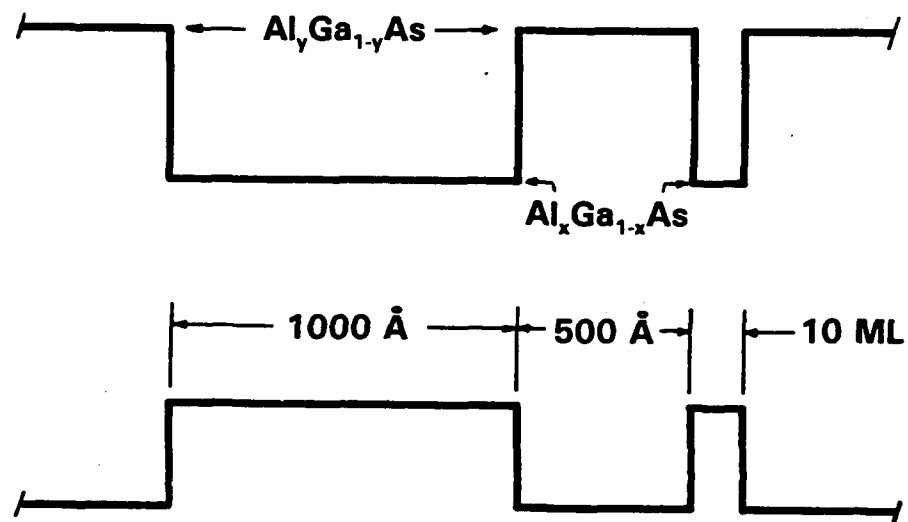


**Figure 4.6** Structure to test compositional dependence of the interdiffusion coefficient. The basic structure shown above contains a 10-ML quantum well of which the transition energies are highly sensitive to intermixing. A 1000-Å-thick well is included to monitor the initial composition of the well material, and is isolated from the thin well by a 500-Å barrier. The well material is  $\text{Al}_x\text{Ga}_{1-x}\text{As}$ , while the barriers are  $\text{Al}_y\text{Ga}_{1-y}\text{As}$  with  $(x,y)$  equal to  $(0,0.2)$  and  $(0.1,0.35)$  for the interdiffusion experiment.

measured compositions, and then varying the width of the layers until the bound state energy matched that of the measured bound state luminescence. The samples were then annealed at 850°C in 1 atm As<sub>4</sub> overpressure for 0.5, 1.75, 4, 6, and 7 hours.

The new bound states of the intermixed quantum wells were measured by photoluminescence. Using the parameters measured prior to the annealing step and the error function model described above, the interdiffusion coefficient was adjusted until the calculated bound state matched the measured bound state. The resulting interdiffusion coefficients versus annealing time are presented in Figure 4.7. The error analysis of the data is based on a 10-Å error in the photoluminescence wavelength, which corresponds to  $\pm 0.003$  deviation in the aluminum composition for the barriers and the Al<sub>0.1</sub>Ga<sub>0.9</sub>As well. For comparison, the same structures were modelled numerically and a simulation of the annealing process was performed using the composition-dependent interdiffusion coefficient given in Equation (4.4). To maintain consistency of method, the resulting shifts in bound state energies were used in an error-function analysis and plotted on the same graph.

The first thing to note in Figure 4.7 is that the error bars for both sets of experimental data overlap, which indicates that the differences due to the aluminum composition are nearly immeasurable. On the other hand, the trend of the (0.1,0.35) structure being consistently higher than the (0,0.2) samples matched the predicted trends in the calculated values. The upward trend in the experimental data may also indicate a composition dependence, since the average aluminum composition of the well increases as aluminum diffuses in. The calculated data shows this trend also, but it is very slight, which means that the magnitude of the upward slope is probably due more to temperature gradients and overpressure fluctuations in the ampoule than it is due to composition. Note that the data for each time were produced by annealing both samples in the same ampoule, so they were subjected to the same conditions.

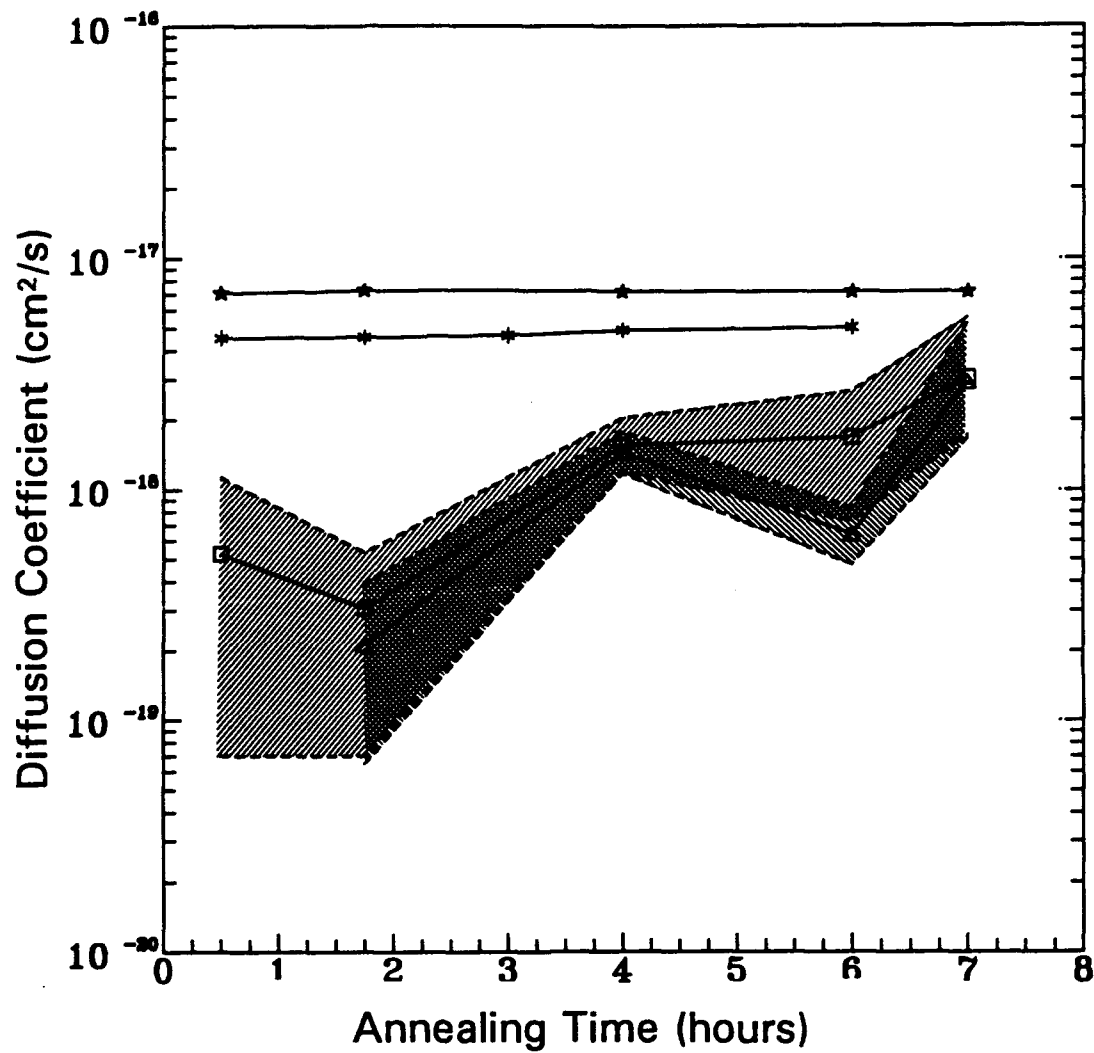


**Figure 4.7** Composition-dependent Al-Ga interdiffusion coefficient as a function of annealing time. The calculated interdiffusion coefficient for measure PL shifts is presented for a 10-ML GaAs/Al<sub>0.2</sub>Ga<sub>0.8</sub>As well (triangles) and a 10-ML Al<sub>0.1</sub>Ga<sub>0.9</sub>As/Al<sub>0.35</sub>Ga<sub>0.65</sub>As well (squares). The lines at the top are for simulated annealing using a compositionally-dependent interdiffusion coefficient and using the resulting energy shifts in an error-function analysis to find an average interdiffusion coefficient. The star corresponds to the Al<sub>0.1</sub>Ga<sub>0.9</sub>As/Al<sub>0.35</sub>Ga<sub>0.65</sub>As well and the asterisk corresponds to the GaAs/Al<sub>0.2</sub>Ga<sub>0.8</sub>As well. The cross-hatched areas in the experimental curves result from an error analysis assuming a 10-Å error in the PL data. The overlap indicates that the compositional dependence cannot be determined reliably.

Since the data does not show a strong compositional dependence, further attempts to accurately determine the composition-dependent interdiffusion coefficient were deemed unnecessary. The reasonable conclusion of this study then, is that the compositional dependence of the interdiffusion coefficient is negligible for annealing processes at 850°C in 1 atm As<sub>4</sub> overpressure. Based on the data by Chang and Koma, however, the dependence is greater at higher annealing temperatures, and a similar study at higher temperatures may show a more distinct dependence, but such an investigation is beyond the scope of this thesis.

### 4.3 Model for Intermixed Superlattices

For calculating the dispersion relationships of superlattices, the Kolbas-Holonyak method described in Section 2.1 is adequate for a superlattice with a small number of periods, each divided into only a few regions. An intermixed well requires many regions to be accurately modeled, so many periods of coupled, intermixed wells would quickly become impractical with their approach. Therefore, an alternate approach was needed which used a periodic potential based on an error function composition profile. The tight-binding approach was examined first.

The energy dispersion relation for the one-dimensional tight binding calculation in the envelope function approximation was given in Section 2.1, and is repeated here for convenience. It is

$$E = E_n + \sum_{r=-\infty}^{\infty} e^{irqa} \int_{-\infty}^{\infty} \Psi_n^*(z - r\alpha) [U(z) - V(z)] \Psi_n(z) dz , \quad (4.9)$$

where  $E_n$  is the calculated bound state for a single, interdiffused quantum well,  $r$  is an integer,  $q$  is the superlattice wave vector,  $\alpha$  is the period of the superlattice,  $\Psi_n$  is the wavefunction of the bound state,  $U(z)$  is the periodic potential defined by the

superposition of all contributing error-function-shaped layer interfaces, and  $V(z)$  is the potential of the single interdiffused quantum well. With nearest-neighbor interactions only ( $r = 0, \pm 1$ ), this reduces to

$$E = E_n - \alpha - 2\beta \cos(q\alpha) . \quad (4.10)$$

As long as the overlap of the wavefunctions from adjacent wells is small, this method provides a good approximation to the dispersion relation calculated using the Kolbas-Holynak approach with several coupled wells. For larger wavefunctions resulting from smaller dimensions, the solutions depart. Adding next nearest neighbor terms actually causes the solutions to differ even more. This suggests that the values of the calculated wavefunctions far from the immediate vicinity of the single well are not accurate enough to give consistent solutions for short periods.

A Kronig-Penney-type calculation was examined next. For this study, a method used by Yuh and Wang,<sup>[56]</sup> and introduced in Section 2.1, was adapted to handle interdiffused superlattices. This approach defines a  $2 \times 2$  transfer matrix for each layer in the basis, given by

$$S_i = \begin{bmatrix} \cos(k_i L_i) & \frac{m_i^*}{k_i} \sin(k_i L_i) \\ -\frac{k_i}{m_i^*} \sin(k_i L_i) & \cos(k_i L_i) \end{bmatrix} \quad (4.11)$$

where  $i$  denotes the layer,  $L_i$  is the layer thickness, and

$$k_i = \frac{\sqrt{2m_i^*(E - V_i)}}{\hbar} . \quad (4.12)$$

The transfer matrices of each region are multiplied together to give the total matrix,  $S$ . Using  $\Gamma(z)$ , a vector with elements  $\Gamma_1(z) = \psi(z)$  and  $\Gamma_2(z) = \psi'(z)/m^*$ , the eigenvalues of  $S$  are found using

$$\Gamma(r + \alpha) = S \Gamma(z) = \lambda I \Gamma(z) . \quad (4.13)$$

Along with Bloch theory, which gives  $\lambda = e^{*iq\alpha}$ , we find

$$S_{11} + S_{22} = e^{iq\alpha} + e^{-iq\alpha} = 2\cos(q\alpha) \quad , \quad (4.14)$$

where  $q$  is the superlattice wavevector. If a simple, two-layer basis is used, the result is the familiar Kronig-Penney solution in the effective mass approximation.

This model was used to calculate the energy dispersion of a GaAs-AlAs superlattice with 35-Å wells and 15-Å barriers. The results are shown in Figure 4.8 representing several annealing times up to 4 hours using an interdiffusion coefficient,  $D = 8 \times 10^{-19} \text{ cm}^2\text{s}^{-1}$  (850°C, 1 atm As<sub>4</sub>). This structure was grown and annealed as well, and the PL spectra are presented in Figure 4.9. Notice that the spectra all contain several distinct peaks, and the second peak is dominant in the as-grown sample, as well as in the sample annealed for one hour.

The calculated transition wavelengths from the critical points of the  $n=1$  electron subband are also shown in Figure 4.9, which indicate that the second large peak is probably due to the  $e_1\text{-}lh_1$  transition. The relative magnitude of this peak can be explained by examining the band diagrams of Figure 4.8. For the as-grown and the 1-hour diffused case, the  $n=2$  heavy hole lines up with the  $n=1$  light hole at the mini-zone edge. As holes thermalized in the  $n=2$  heavy hole band, some will recombine at the band edge ( $e'_1\text{-}hh_2$  transition, with the prime indicating the band-edge saddle point), while most will scatter into the  $n=1$  light hole band. From there, they will either recombine at the saddle point ( $e'_1\text{-}lh'_1$ ), or thermalize further to recombine at  $q = 0$  ( $e_1\text{-}lh_1$ ).

Time-resolved photoluminescence (TPL) measurements support this explanation. In all cases above, the measured lifetime of the second peak was longer than that of the first peak, which is logical if holes are being supplied to the  $n=1$  light hole subband from the  $n=2$  heavy hole subband over a finite time. This is supported further by the

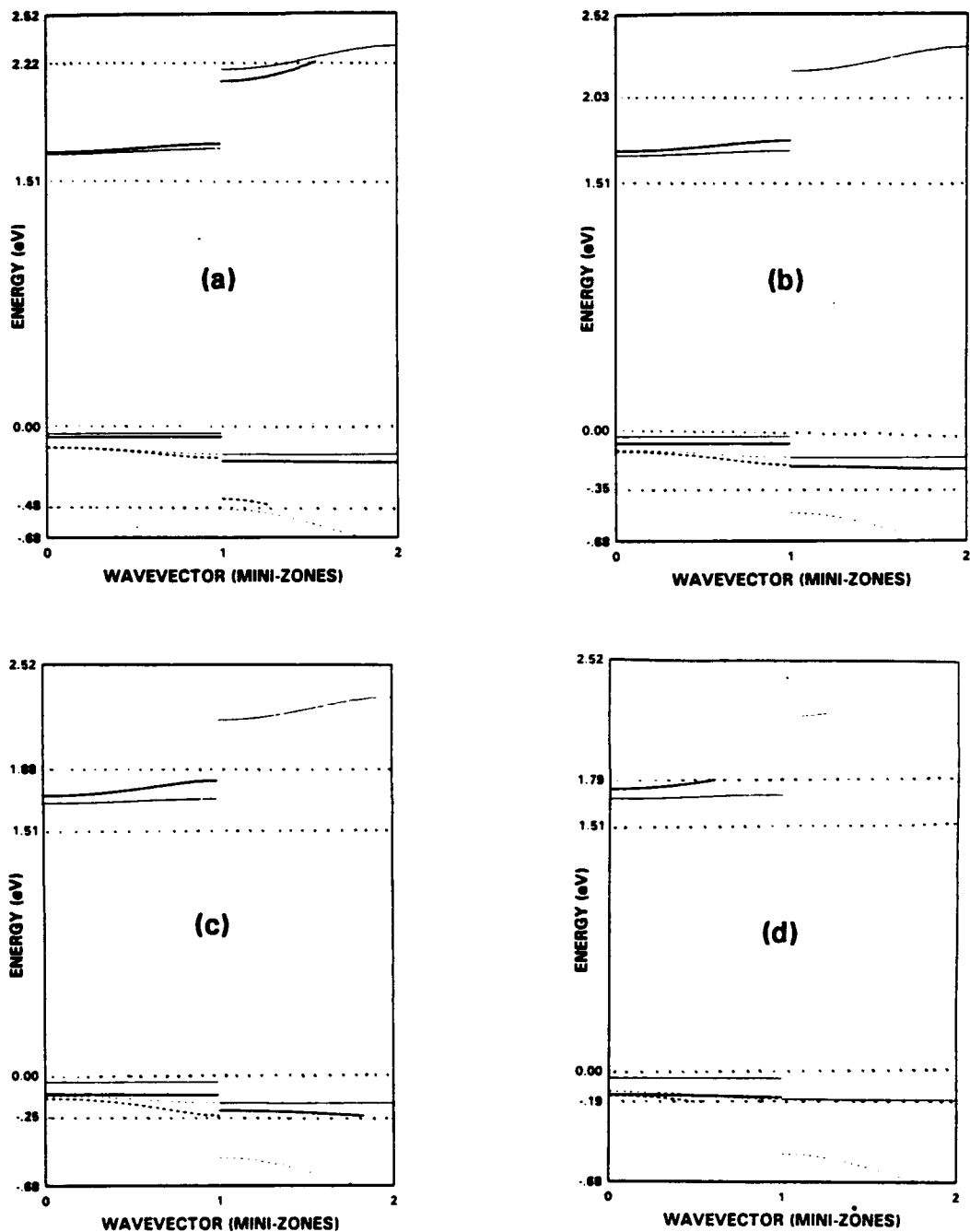


**Figure 4.8** Energy dispersion curves for an intermixed GaAs/AlAs superlattice. The frames above show the energy diagrams of a GaAs/AlAs superlattice grown with 35-Å wells and 15-Å barriers and annealed for 30, 60, 120, and 240 minutes ((a), (b), (c), and (d), respectively) for the first two mini-zones. The heavy solid lines represent the electrons and heavy holes, while the dashed lines represent the light holes. The lighter lines are for the as-grown samples. The energy spans the gap of AlAs, and the dotted lines between the AlAs and GaAs band edges are the positions of the top of the intermixed barriers.

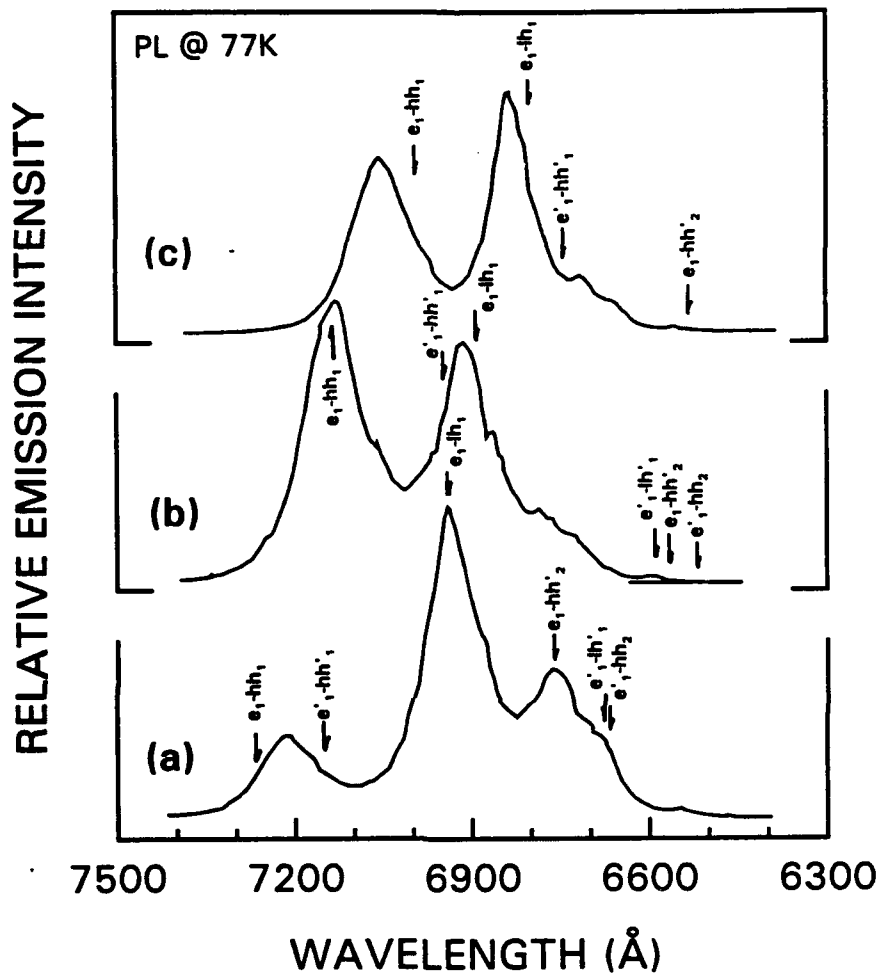


**Figure 4.9** Photoluminescence spectra of an annealed GaAs/AlAs superlattice. The PL spectra of a GaAs/AlAs superlattice grown with 35-Å wells and 15-Å barriers is shown as-grown (a) and after annealing for 30 minutes (b) and 60 minutes (c) at 850°C in 1 atm As<sub>4</sub>. The calculated transition wavelengths for critical points of the first electron subband and the first two hole subbands. The saddle points of the minibands are denoted by a prime.

measured decay of the luminescence intensity at the second-major-peak wavelength. The log of the decay, shown in Figure 4.10, indicates that the band was being with supplied with carriers during the first few hundred picoseconds, where the lifetime is very long (the slope is very small at first). After about 700 ps, the curve reaches a constant slope which yields what is presumably the  $e_1-lh_1$  lifetime after the  $n=2$  heavy hole band is empty.

While both the PL and TPL data support the superlattice model, there are several bumps in the PL spectra which do not correspond to predicted transitions between critical points of the subbands. These features, as well as the divergence of the calculated and measured critical points for longer anneal times (PL data not shown) may be explained by valence band mixing.<sup>[79]</sup> If the zones of Figure 4.8 are folded, the  $hh_2$  band and the  $lh_1$  band touch or cross. At these points, anticrossings will occur which will form new critical points, and the  $lh_1$  band will take on some characteristics of the  $hh_2$  band, and vice-versa. These effects are not included in this model.

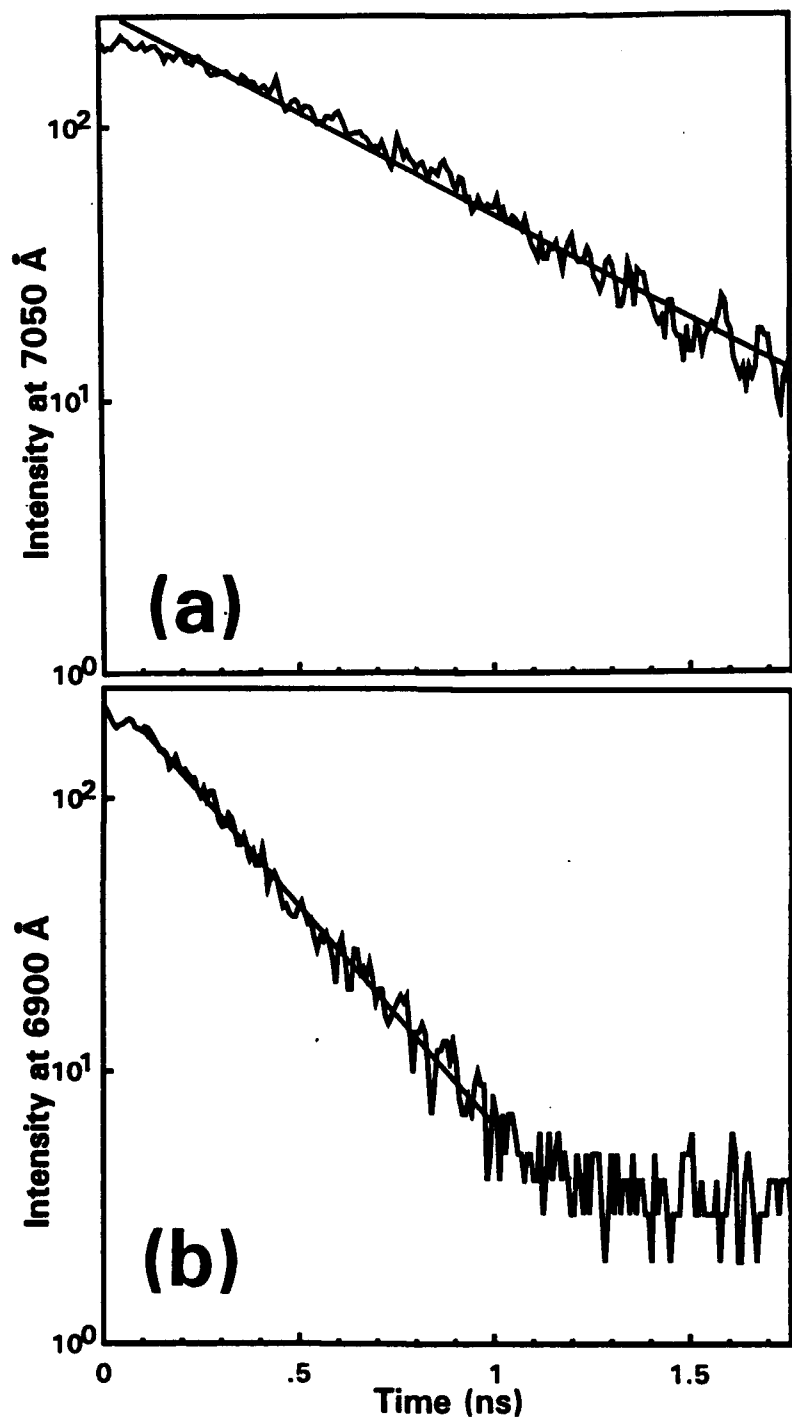


**Figure 4.10** Luminescence decay of the electron-to-light-hole transition. The decay of the second major luminescence peak of a GaAs/AlAs superlattice with 35-Å wells and 15-Å barriers is shown (a). The lifetime is estimated using a least-squares algorithm to find the slope of the decay. Notice that the data does not become linear until about 700 ps, in contrast to a more typical decay shown in (b). The data in (a) begins with a long characteristic lifetime, probably because it represents the  $e_1$ - $lh_1$  transition with the  $lh_1$  band being filled by the  $hh_2$  band at the mini-zone edge.

## 5 Selective Intermixing

In order to exploit the various attributes of intermixed quantum wells and superlattices, the methods of producing such structures must be controlled so that selected areas of a sample become intermixed, while other areas remain preserved. In this chapter, three methods of selectively intermixing semiconductor quantum heterostructures are examined. They are: (1) using a focused ion beam to create localized areas of excess gallium near a superlattice, (2) encapsulating with the dielectric  $\text{SiN}_x$ , and (3) fabricating features in GaAs grown at low substrate temperature to provide excess arsenic to local areas on a chip.

### 5.1 Localized Gallium Overpressure

The use of a gallium overpressure was shown by Hsieh *et al.* to suppress the interdiffusion of quantum wells exposed to high temperatures.<sup>[12]</sup> On the other hand, Hirayama *et al.*<sup>[36]</sup> and Cibert *et al.*<sup>[16]</sup> showed that gallium implanted into the heterostructure enhanced the interdiffusion process. In this thesis, gallium atoms were implanted near the surface, away from the heterostructure, in order to generate local gallium overpressures which should suppress the Al-Ga interdiffusion at the layer interfaces.

#### 5.1.1 Gallium Focused Ion Beam

A sample was grown with a 55-period  $\text{GaAs}/\text{Al}_{0.35}\text{Ga}_{0.65}\text{As}$  superlattice with 35-Å wells and barriers, surrounded by  $\text{Al}_{0.35}\text{Ga}_{0.65}\text{As}$ . The superlattice was 5000 Å from the surface of the sample. A gallium focused ion beam (FIB) was used to write 100 x 100  $\mu\text{m}$  squares with implant energies of 15, 20, and 25 keV in doses between  $2 \times 10^{10} \text{ cm}^{-2}$  to  $4 \times 10^{15} \text{ cm}^{-2}$ . These energies correspond to implant depths on the order of 100 Å,

so the ions were far enough above the superlattice not to cause any damage. Most of the doses were below  $10^{14} \text{ cm}^{-2}$ , which is the threshold at which implant damage becomes the dominant mechanism for generating defects as reported by Hirayama *et al.*<sup>[36]</sup>

The photoluminescence (PL) spectra of the patterns were taken as a baseline. The spectra of the implanted features showed a very broad peak for energies in the bandgap which corresponded to luminescence from the implant-damaged surface. This peak was absent in the unimplanted regions between features. The 15-keV-implanted features were annealed at  $850^\circ\text{C}$  with no overpressure for 3 hours, and the 20- and 25-keV-implanted features were annealed at  $825^\circ\text{C}$  under the same overpressure and time conditions.

The PL spectra were taken again after the annealing step and compared to the pre-annealed spectra. The broad peaks from the initial implant damage were gone. The positions of the  $n=1$  subband luminescence peaks shifted in wavelength less than  $100 \text{ \AA}$ , which corresponds to an interdiffusion coefficient of  $2 \times 10^{-19} \text{ cm}^2\text{s}^{-1}$ , and is commensurate with the peak shifts expected for annealing in a gallium overpressure.

Finally, a scan of the PL peaks across and between the 15 keV,  $2.3 \times 10^{10} \text{ cm}^{-2}$  features was taken to compare the peak shifts of the implanted and unimplanted areas. Surprisingly, was no measurable difference was noted. This means one of two things. First, the gallium implanted into the surface had no effect, and the results are due to the annealing process with no overpressure. Second, the defects generated by the implant were predominantly highly mobile gallium interstitials ( $I_{\text{G}_\text{s}}$ ) that diffused outward from the features as much as  $100 \text{ \AA}$  or more, thereby preserving the superlattice around the features as well. Since the peak shifts agree with previous data resulting from the

gallium overpressure annealing process,<sup>[31]</sup> the second explanation is worthy of further investigation when the opportunity to obtain FIB-written samples again becomes available.

### **5.1.2 *Electron Mobility Experiment***

The possibility of using FIB technology to write small areas of gallium to preserve large areas of a quantum structure suggested some ideas which led to a side experiment involving a high-electron mobility transistor (HEMT) structure (or modulation-doped field effect transistor (MODFET) structure). The HEMT device relies on the sharp interface between an n-type AlGaAs layer and an intrinsic GaAs layer. The conduction band bends as the Fermi levels of the two materials line up, which causes a notch to form at the junction. This notch contains quantum bound states into which electrons from the donors on the AlGaAs side fall. The electrons are then in a two-dimensional (2D) electron gas, which is separated from the ionized impurity scattering sites, resulting in high mobilities. If the interface is not sharp, then the quantum well smears out and the 2D electron gas is lost.

To determine the effects of a gallium overpressure on an annealed HEMT structure, an experiment was designed in which the mobility of a HEMT structure was measured before and after annealing with no-overpressure, gallium-overpressure, and, for completeness, arsenic-overpressure. An unprocessed, three-inch production HEMT wafer was provided by the Martin Marietta Corporation. The epitaxial layers consisted of a 1- $\frac{3}{4}$  m GaAs buffer grown on the substrate, followed by a 20-Å  $\text{Al}_{0.26}\text{Ga}_{0.74}\text{As}$  undoped spacer, a 400-Å  $\text{Al}_{0.26}\text{Ga}_{0.74}\text{As}$  Si-doped ( $N_D = 3 \times 10^{18}$ ) layer, and then a 400-Å Si-doped ( $N_D = 4 \times 10^{18}$ ) GaAs contact layer. This is a structure in which the channel is normally on.

The wafer was cleaved into 1-cm squares, and the mobility was measured to assess its uniformity. The mobilities were between about 21,000 and 28,000  $\text{cm}^2\text{V}^{-1}\text{s}^{-1}$  at 77K. Because the indium used for the contacts would contaminate the atmosphere inside the ampoules during annealing, either separate samples had to be used for the annealed structures or the indium contacts had to be cut off. Because of the wide range of mobilities in the as-grown samples, the latter method was chosen. First, however, several of the previously measured samples were cut down to 6.5-mm squares, and re-measured to determine if the size difference affected the measured mobility. The measured mobility of the smaller samples were on average higher by about 1000  $\text{cm}^2\text{V}^{-1}\text{s}^{-1}$ , and this difference was taken into account in subsequent tests.

The annealing steps were performed at 850°C for 20 and 60 minutes. The mobilities of the arsenic-overpressure samples could not be measured, which is probably a result of the quantum well being completely intermixed as expected. The measured mobilities of the samples without an overpressure for annealing times of 20 and 60 minutes were 10.2% and 8.0% of their original (adjusted) values, respectively. Finally, for the gallium overpressure, the mobility after 20 minutes was 10.0% of the original value, while it could not be measured after 60 minutes. The poorer mobilities for the gallium overpressure samples was puzzling at first, but since the HEMT structure is a surface device, the mobility was dominated by the effects of the annealing process on the surface. In the gallium atmosphere at high temperature, arsenic atoms come out of the surface faster than with no overpressure. (The surface morphology is commonly preserved by keeping arsenic atoms in with an arsenic overpressure.) The defects in the arsenic-poor surface will then drive the surface depletion region deeper into the structure, which eventually depletes the channel.

To assess the capability of a small gallium-implanted area to preserve a large area surrounding it, a more appropriate experiment might be to encapsulate an implanted structure in  $\text{Si}_3\text{N}_4$  to maintain the surface morphology, and then proceed with the annealing process. An alternate approach to encapsulation would be to use rapid thermal annealing with the surface of the HEMT sample in contact with a bare GaAs wafer.

## 5.2 $\text{SiN}_x$ Encapsulation

Another method which was investigated for use in selective intermixing was to pattern stripes of the dielectric  $\text{SiN}_x$  on the sample surface. This technique preserves the stoichiometry under the dielectric, which reduces the generation of point defects during high temperature processes. The exposed surfaces will react with the ambient overpressure which can generate enough defects to enhance the interdiffusion process.

To verify this, a sample was prepared which had a 21-period GaAs/AlAs superlattice with 79-Å wells and 40-Å barriers. The superlattice was bounded on either side by  $\text{Al}_{0.3}\text{Ga}_{0.7}\text{As}$  ( $1\frac{3}{4}$  m buffer and  $0.75\frac{3}{4}$  m cap). A 1000-Å  $\text{SiN}_x$  film was deposited on the sample, and  $100\frac{3}{4}$  m-thick stripes spaced  $100\frac{3}{4}$  m apart were fabricated in the film. PL spectra were taken for both the open and encapsulated surface, and were the same for both types of areas.

The sample was then annealed at  $850^\circ\text{C}$  for 3 hours with no overpressure. The PL spectra were taken again, and they are presented in Figure 5.1. The encapsulated stripes experienced a wavelength shift in the luminescence peak of only 40 Å, while the exposed stripes shifted 200 Å, or five times that of the preserved stripes. The corresponding interdiffusion coefficients were  $1.6 \times 10^{-19} \text{ cm}^2\text{s}^{-1}$  and  $6.7 \times 10^{-19} \text{ cm}^2\text{s}^{-1}$ , respectively, which resulted in a 4.2:1 selectivity ratio.

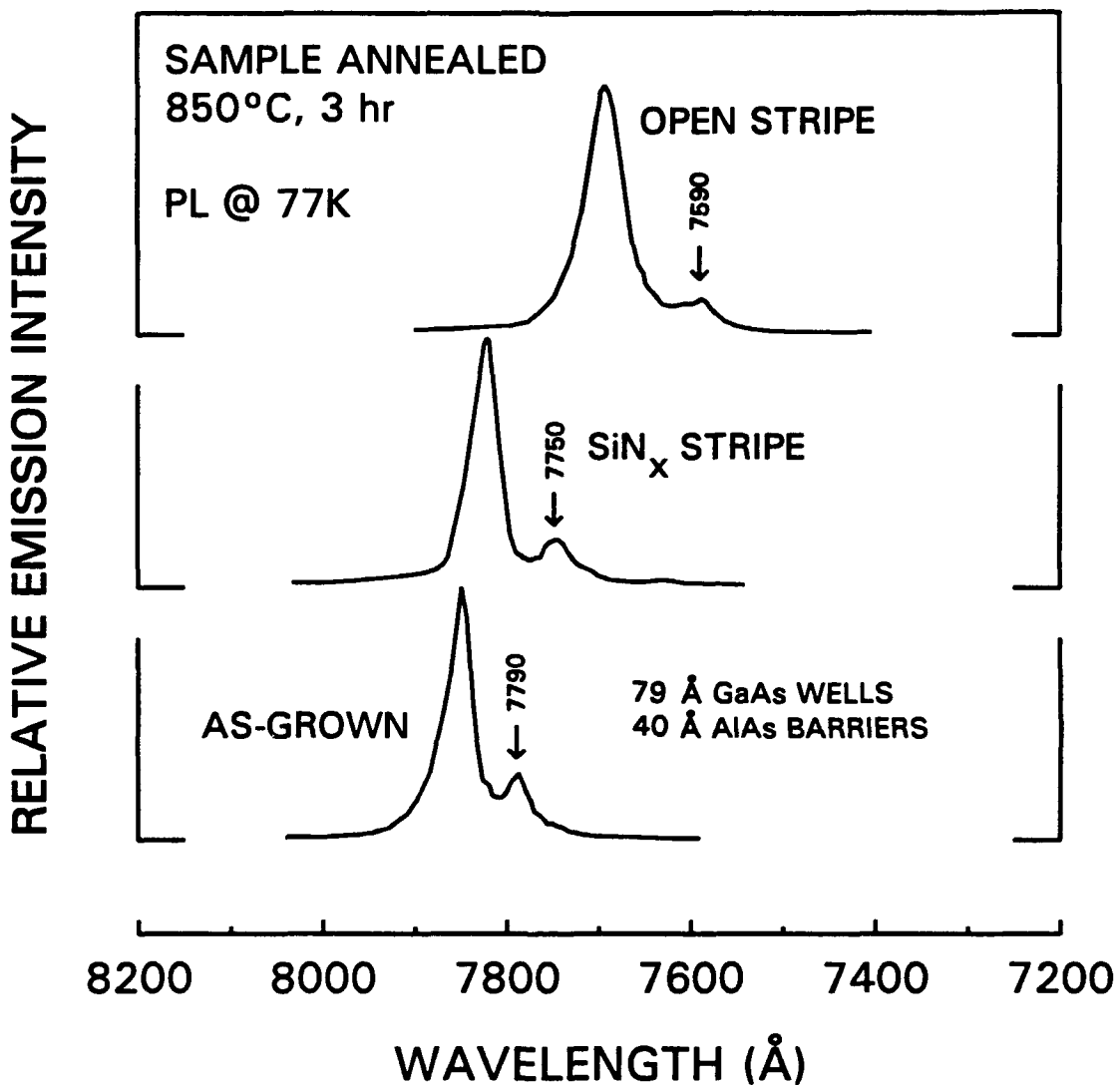


**Figure 5.1** Photoluminescence spectra of a selectively intermixed GaAs/AlAs superlattice via SiN<sub>x</sub> encapsulation. The spectra are for a GaAs/AlAs superlattice grown with 79-Å wells and 40-Å barriers, both before and after annealing at 850°C for 3 hours. The major peak is due to the lowest state of the first well of the superlattice, which was asymmetric since it was bounded by Al<sub>0.3</sub>Ga<sub>0.7</sub>As on one side. The lowest superlattice state transition wavelength shift only 40 Å when covered with a SiN<sub>x</sub> stripe, and 200 Å when uncovered. This results in a selectivity ratio of the interdiffusion coefficient of 4.2:1.

These results indicate that this method of selective intermixing is a viable technique to selectively alter the electronic properties of a superlattice. Notice that since both regions experienced shifts in the  $n=1$  subband energy levels, the optical properties would be changed in both also. This particular structure was designed to result in the largest difference in the weighted average index of refraction of the AlAs and GaAs, and the index of the corresponding alloy,  $\text{Al}_{0.33}\text{Ga}_{0.67}\text{As}$ . Since the wells were neither completely preserved nor intermixed, the indices of both the "preserved" and the "intermixed" regions must fall somewhere between the extremes. The problem of determining the index of partially intermixed wells is examined in Chapter 6.

Finally, the extent of intermixing in the lateral direction at the boundaries between the open and covered areas needs to be addressed before devices such as optical waveguides with widths of only 5 to 10  $\mu\text{m}$  can be fabricated using this technique. Methods of optimizing this technique should also be considered, such as annealing in an arsenic-overpressure, or implanting the exposed surface with arsenic ions to enhance the intermixing process.

### 5.3 Low-Temperature Gallium Arsenide

Low-temperature (LT) GaAs refers to a GaAs epitaxial layer grown by molecular beam epitaxy (MBE) at a low substrate temperature of 200°C (as opposed to 640°C). This growth process results in a layer which is arsenic-rich,<sup>[30]</sup> and has been shown to enhance the Al-Ga interdiffusion coefficient when used as a buffer layer.<sup>[29]</sup> In this work, an LT-GaAs buffer layer was patterned with stripes to provide local arsenic overpressures.

First, a 0.2- $\mu\text{m}$  LT-GaAs layer was grown on a GaAs substrate. The layer was processed using photolithography and a wet chemical etch to produce 100- $\mu\text{m}$ -wide LT-GaAs stripes separated by 100  $\mu\text{m}$  on top of the original wafer. The wafer was then

degreased and an abbreviated surface-preparation etch was used to avoid etching away the LT-GaAs stripes. The wafer was loaded back into the MBE for a second growth. A structure was grown on top of the processed wafer which consisted of a 0.5- $\frac{3}{4}$  m  $\text{Al}_{0.35}\text{Ga}_{0.65}\text{As}$  layer, an 87-Å GaAs quantum well layer, and another 0.5- $\frac{3}{4}$  m  $\text{Al}_{0.35}\text{Ga}_{0.65}\text{As}$  layer. Although most of the wafer was hazy, indicating poor crystalline structure, sufficient parts of it were clear enough to continue an annealing experiment.

The quality of the quantum wells was verified by taking the PL spectra of several stripes, which also established a baseline for the experiment. The sample was then annealed in an ampoule with no overpressure for 4 hours at 850°C. The PL peaks measured after the annealing step showed a wavelength shift of about 210 Å from the wells grown on the LT-GaAs buffer layer stripes, and about 190 Å from the other wells. The data is presented in Figure 5.2.

Although the differences are small, they are consistent between adjacent wells, which suggests that the Al-Ga interdiffusion coefficient in the structures grown on the LT-GaAs stripes was enhanced over that of the adjacent stripes. The small difference in peak shifts could be a result of the LT-GaAs stripes being thinned too much during the surface etch in the sample preparation step before the second growth, as the etch rate was not calibrated. An attempt to grow additional layers on a sample with LT-GaAs stripes without using a surface preparation etch resulted in a completely unacceptable surface. Clearly, this technique needs further refinement in order to produce samples with enough difference in the interdiffusion rates to be a useful method of selective intermixing.

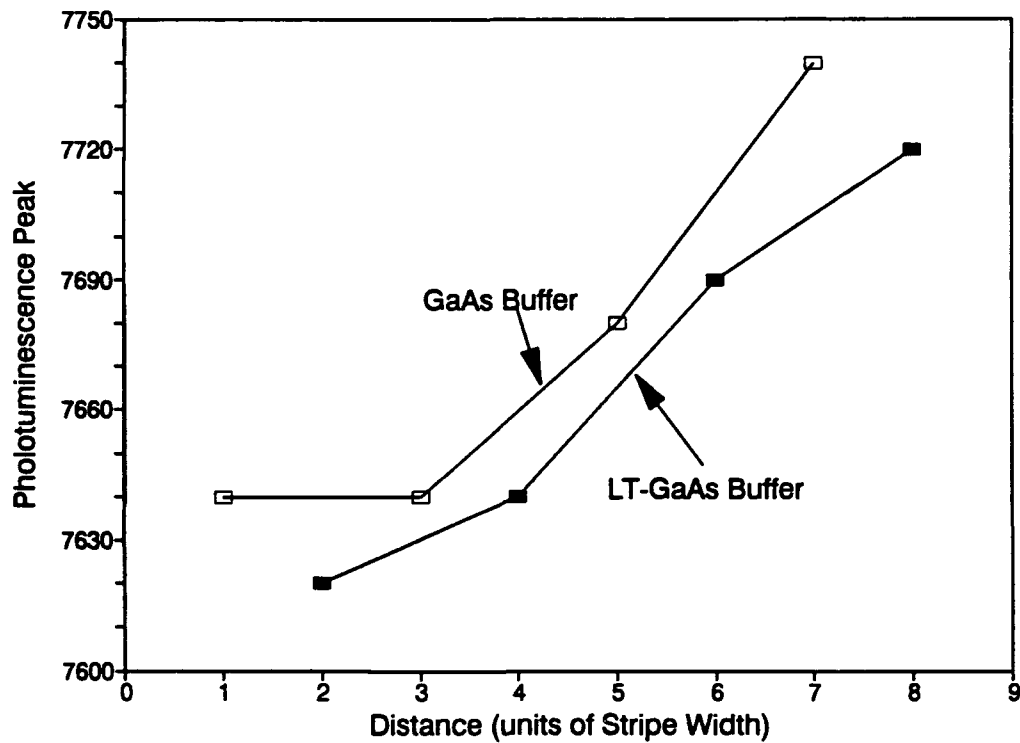


**Figure 5.2** Photoluminescence peaks of a selectively intermixed quantum well using low-temperature GaAs. The structure was an 87-Å GaAs/Al<sub>0.33</sub>Ga<sub>0.65</sub>As quantum well grown on stripes of LT-GaAs and annealed for 4 hours at 850°C. The wells over the LT-GaAs shifted to a lower wavelength than the wells grown over a conventional GaAs buffer. The overall trend in the wavelength across the wafer is probably due to non-uniformities in the growth.

## 6 Optical Properties of Intermixed Quantum Wells

All of the optical properties of an intermixed quantum well, as with any semiconductor, are contained in the complex dielectric constant

$$\epsilon(\omega) = \epsilon'(\omega) + i\epsilon''(\omega) , \quad (6.1)$$

and, in general, are a function of frequency (see Appendix A).

Absorption and reflection properties can be found by relating  $\epsilon(\omega)$  to the complex index of refraction  $n_c$  by

$$\frac{\epsilon(\omega)}{\epsilon_0} = n_c^2(\omega) = (n(\omega) + i\kappa(\omega))^2 \quad (6.2)$$

where  $\epsilon_0$  is the free-space permittivity,  $n(\omega)$  is the real part of the index and  $\kappa(\omega)$  is the extinction coefficient. The absorption coefficient  $\alpha(\omega)$  is related to the extinction coefficient by

$$\alpha(\omega) = \frac{2\kappa(\omega)}{c} \omega \quad (6.3)$$

where  $c$  is the speed of light. Using  $\epsilon''/\epsilon_0 = 2n\kappa$ ,  $\alpha(\omega)$  is related to the imaginary part of  $\epsilon(\omega)$  by

$$\alpha(\omega) = \frac{\omega}{\epsilon_0 c n(\omega)} \epsilon''(\omega) . \quad (6.4)$$

Finally, the reflectivity at normal incidence is given by

$$R(\omega) = \frac{(n(\omega) - 1)^2 + (\kappa(\omega))^2}{(n(\omega) + 1)^2 + (\kappa(\omega))^2} . \quad (6.5)$$

In order to determine the actual values of the optical properties of an intermixed quantum well, therefore,  $\epsilon(\omega)$  must be calculated. In the oscillator approach to determining  $\epsilon(\omega)$ , the complex dielectric constant is

$$\epsilon(\omega) = \epsilon_0 + N \sum_j \frac{e^2}{m_0} \frac{f_j}{(\omega_j^2 - \omega^2) - i2\gamma_j\omega} . \quad (6.6)$$

The dielectric function is, then, the sum of the dielectric responses of all the oscillators in the system, each with a resonant frequency  $\omega_j$ , oscillator strength  $f_j$ , and damping coefficient  $\gamma_j$ . The oscillator strength is

$$f_j = \frac{2}{m_0 \hbar \omega_j} |M|^2 \quad (6.7)$$

where  $|M|^2$  is the momentum matrix element of the oscillator.

The frequency is calculated by solving for the energy levels in the quantum well as described earlier. This also yields the envelope wavefunctions of the electron and hole states, which is necessary for calculating the matrix element.

In order to isolate the dielectric constant of the intermixed quantum well, the sum of all the oscillators in Equation (6.6) is restricted to the energy levels, or oscillators in the quantum well. The remaining oscillators of the system are combined with  $\epsilon_0$  to form a background dielectric constant,  $\epsilon_b$ . This assumes that the changes in the dielectric constant are due solely to the modifications of the bound states in the well, since the electronic states of the bulk barrier material remain unaffected by the annealing process.

## 6.1 The Matrix Element of Intermixed Quantum Wells

Except for the bound state energies, the matrix element is the most important factor in determining the optical properties of a quantum well. It describes the interaction between states in the conduction and valence bands, and directly influences the oscillator strength and the radiative lifetime of excited states. Following is the theoretical development of the matrix element as it relates to intermixed quantum wells, as well as the description of an experiment to observe the calculated changes to it.

### 6.1.1 Theory

The matrix element for a single oscillator between two states,  $m$  and  $n$ , with a single polarization is

$$M_{mn} = \langle n | m \rangle P_{mn} \delta(\vec{k}_{n\parallel} - \vec{k}_{m\parallel}) , \quad (6.8)$$

where  $\langle n | m \rangle$  is the overlap of the electron wavefunction in state  $n$  and the hole wavefunction in state  $m$ ,  $P_{mn}$  is the interband matrix element including the selection rules, and the delta function conserves momentum in the directions parallel to the layers in the quantum well, described by the wavevectors  $\vec{k}_{n\parallel}$  and  $\vec{k}_{m\parallel}$  (see Appendix B). The interband matrix element in III-V semiconductors for electron-to-heavy-hole (TE) transitions at  $k_z = 0$  is

$$|P_{mn}| = \sqrt{\frac{1}{4} P_0} , \quad (6.9)$$

where the factor of  $\frac{1}{4}$  comes from  $\frac{1}{2}$  for the average over all directions ( $\frac{1}{3}$  for bulk) and  $\frac{1}{2}$  for the conservation of spin.  $P_0$  is found using the Kane model<sup>[67]</sup>

$$P_0^2 = \frac{m_0 E_0}{2} \left( \frac{m_0}{m_c^*} - 1 \right) \frac{E_0 + \Delta}{E_0 + \frac{2}{3} \Delta} , \quad (6.10)$$

where  $m_0$  is the free-electron mass,  $m_c^*$  is the conduction-band effective mass,  $E_0$  is the bulk material bandgap, and  $\Delta$  is the split-off energy for the split-off valence band.

For GaAs/AlGaAs quantum wells with thicknesses greater than about 40 Å, the matrix element can be considered a constant, taking the value of GaAs, which is about  $|P_{mn}|^2 = 1.87 m_0 E_0$  for a quantum well ( $1.25 m_0 E_0$  for the bulk material). For thinner wells, a significant portion of the envelope wavefunctions extends into the AlGaAs barriers where the interband matrix element is reduced. For instance, the value of  $P_0^2$  is 1.15 times greater in GaAs than it is in  $\text{Al}_{0.3}\text{Ga}_{0.7}\text{As}$ . To include this

effect in the calculation of the matrix element for thin wells, the interband matrix element for each layer must be calculated and then weighted by the amount of overlap of the electron and hole wavefunctions for each region. Equation (6.8) must then be modified to give

$$M_{mn} = P_{mn}(I) \int_{-\infty}^{-\frac{L_z}{2}} \Psi_m^* \Psi_n dz + P_{mn}(II) \int_{-\frac{L_z}{2}}^{\frac{L_z}{2}} \Psi_m^* \Psi_n dz + P_{mn}(III) \int_{\frac{L_z}{2}}^{\infty} \Psi_m^* \Psi_n dz \quad (6.11)$$

where  $\Psi_m$  and  $\Psi_n$  are the envelope wavefunctions of the carriers, and momentum conservation is implied. A schematic for calculating  $M_{mn}$  is given in Figure 6.3. The barriers are denoted as regions I and III while the well is region II. The matrix element normalized to  $P_0^2$  for GaAs for several cases is shown in Figure 6.4. The solid line depicts the theory for a GaAs well between  $\text{Al}_{0.3}\text{Ga}_{0.7}\text{As}$  barriers. For thin wells, the overlap of the electron and hole wavefunctions is reduced because of the differences in the effective masses of the carriers, which causes the curve to diverge from the ideal 2D case of an envelope overlap of unity. Including the effect of the barrier interband matrix element results in a further reduction of the matrix element for ultrathin wells compared to the use of only the GaAs interband matrix element. The matrix elements for both the electron-to-heavy-hole (e-hh) and electron-to-light-hole (e-lh) transitions with the barrier effects as well as the GaAs-only approximation are shown in Figure 6.5.

In recent work performed by Benjamin,<sup>[80]</sup> this model of the optical matrix element was used in the calculation of the dynamics of stimulated photon emission from the  $n=1$  e-hh transitions in 54-Å and 17-Å single quantum well heterostructure lasers. When the matrix element was used to calculate the gain coefficient, a reduced value was obtained compared to a model which is valid for thick wells. Although both

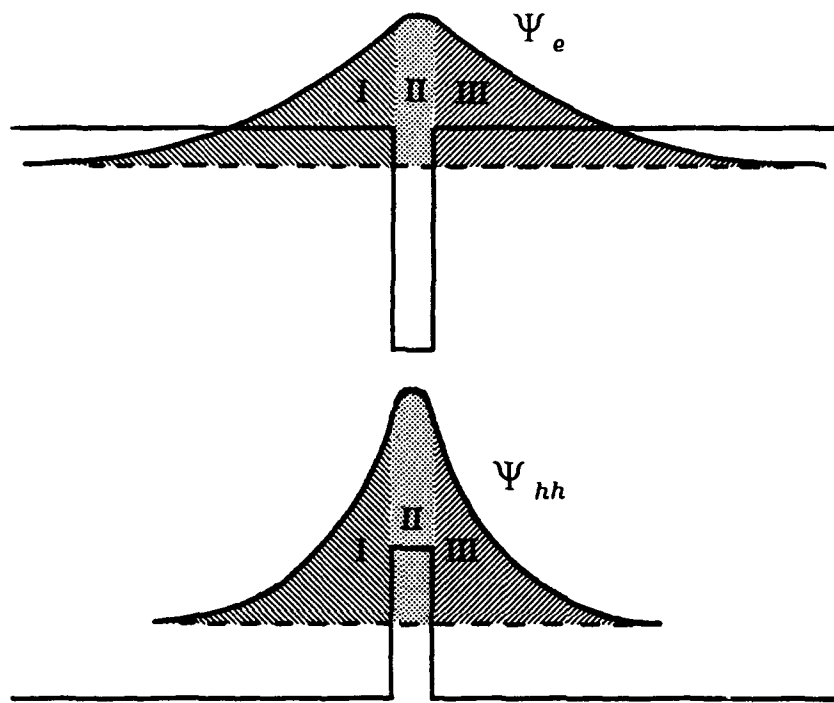


**Figure 6.1** Schematic for calculating the matrix element of a thin quantum well. The electron and hole envelope wavefunctions are shown with different shading for each region of the structure to emphasize that each region is considered separately. The overlap of the wavefunctions are calculated for each region and used as a weight to the interband matrix element of the corresponding region. The total matrix element is then the sum of the matrix elements for each region.

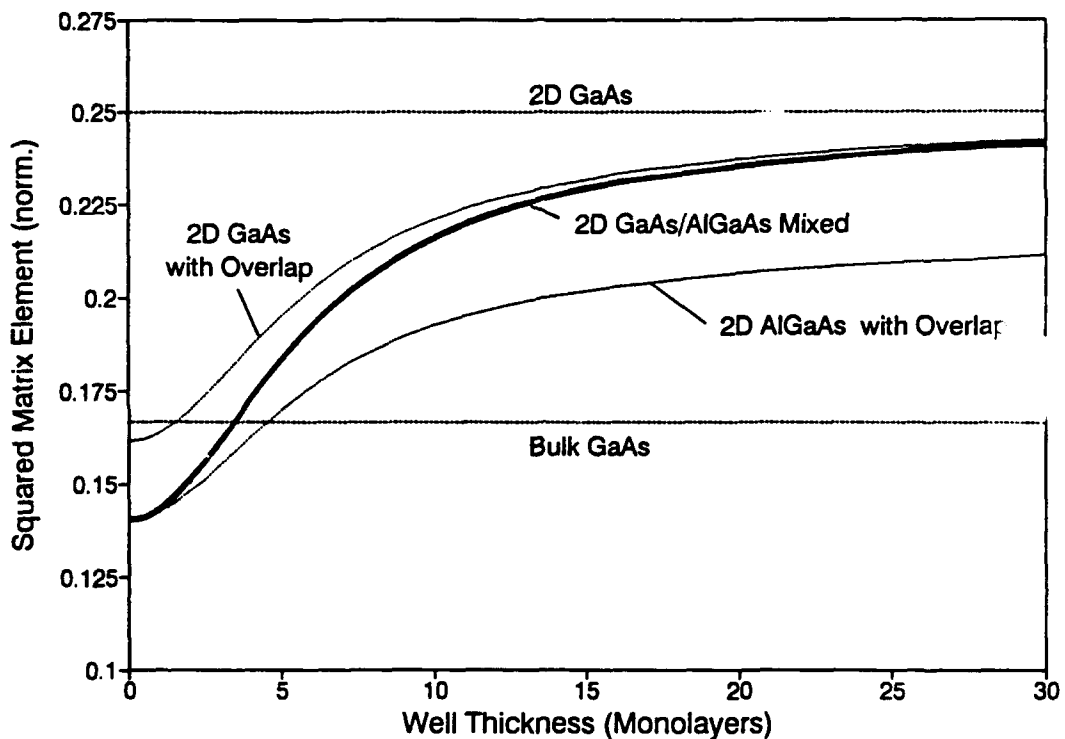


**Figure 6.2** Matrix element for  $e_1$ - $hh_1$  transitions in a  $\text{GaAs}/\text{Al}_{0.3}\text{Ga}_{0.7}\text{As}$  quantum well as a function of well thickness. The  $e_1$ - $hh_1$  matrix element (heavy solid line) is less than the ideal 2D case for thin wells because of the reduced overlap of the electron and hole wavefunctions. The consideration of the lower barrier interband matrix element causes a further reduction in the overall matrix element for ultrathin wells since the wavefunctions are almost entirely in the barriers.

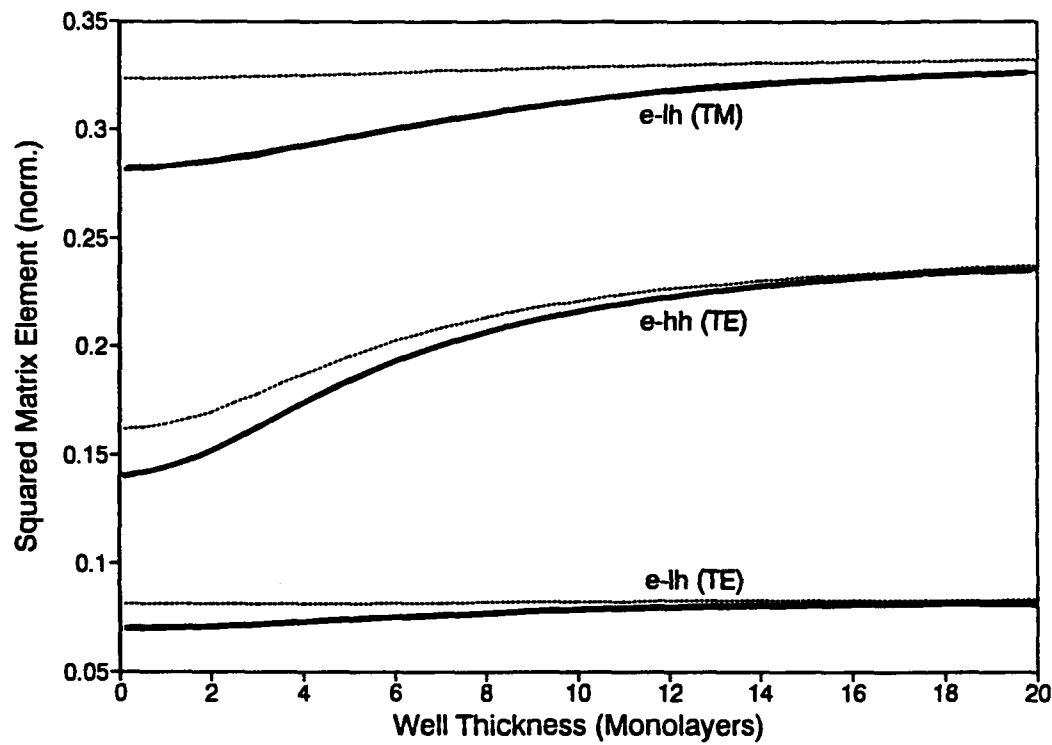


**Figure 6.3** Matrix elements as a function of thickness for  $e_1\text{-}hh_1$  and  $e_1\text{-}lh_1$  transitions in a GaAs/Al<sub>0.3</sub>Ga<sub>0.7</sub>As quantum well. Notice that the matrix elements for thin wells get smaller due to the overlap between electron and hole wavefunctions. The dotted lines are for the case where the difference in the interband matrix elements between the well and barrier materials are neglected.

models should agree for thick wells, these thin wells have carrier wavefunctions which extend into the barriers, and the overlap between electron and hole wavefunctions is reduced, which is not taken into account in the thick-well model. For the 54-Å well, the thick-well gain coefficient calculated using the thick well model was 8.52 times that of the model using this matrix element. (Benjamin reports a factor of 4.26, but he neglected spin conservation in his calculation.) To fit the experimentally measured lasing delay to the calculated delay, the gain coefficient had to be scaled down by an additional factor of 1.15. For the 17-Å well, the coefficient was scaled down by 1.60 to fit the data. The agreement would be closer, however, if the electron-hole wavefunction overlap was used instead of only the electron wavefunction in calculating the overlap between the carrier wavefunction and the optical field.

The theory is easily extended to intermixed wells by dividing the well into  $N$  regions such that

$$M_{mn} = \sum_{i=0}^N P_{mn}(i) \int_i \Psi_m^* \Psi_n dz . \quad (6.12)$$

The results for several well thicknesses as a function of annealing time are shown in Figure 6.6. Notice that the matrix element gets larger in time for the e-hh transitions in the thinnest wells, is relatively constant for e-lh transitions in the thinnest wells and e-hh transitions in the thicker wells, and decreases for e-lh transitions in the thicker wells. This can be explained by considering the aluminum composition dependence of the interband matrix element, and the overlap of the electron and hole envelope wavefunctions, which are competing mechanisms. Each case is explained separately below. Note that, in general, while an 8-monolayer (ML) well is considered thin, in this context, it is considered "thick" when compared to wells of only a few monolayers or less.

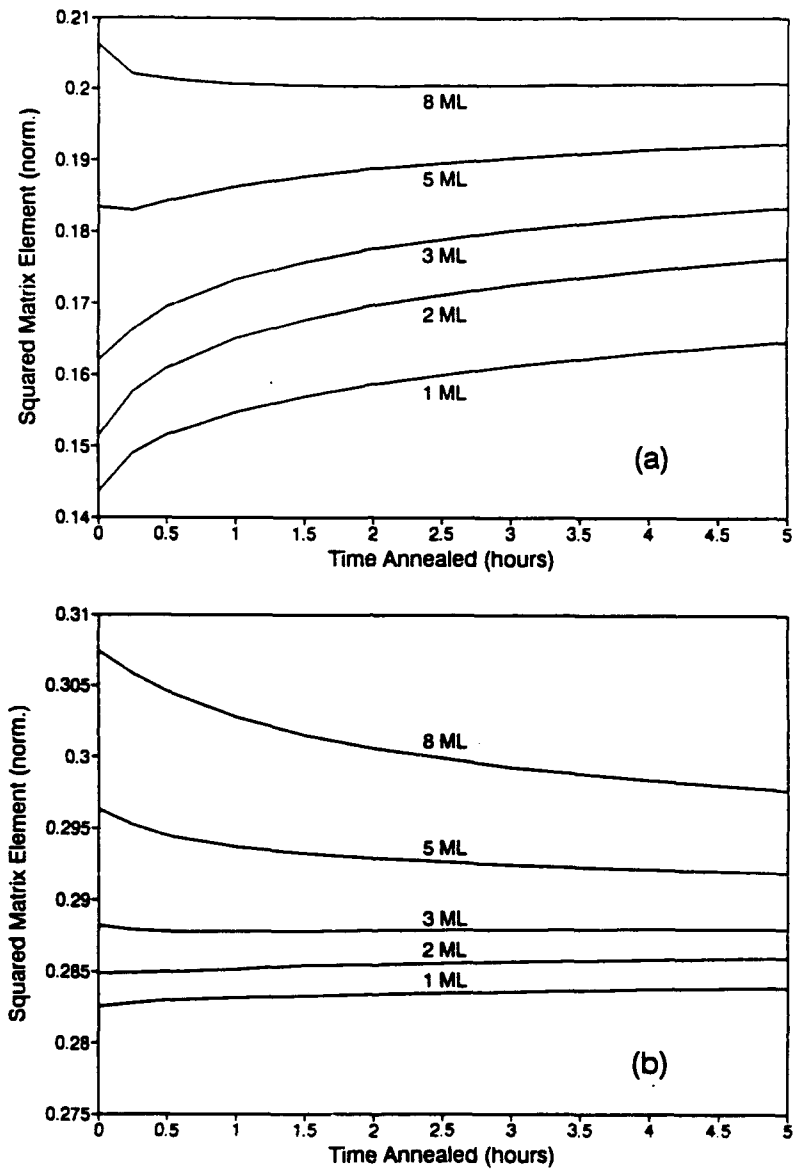


**Figure 6.4** Matrix elements for intermixed quantum wells. The  $e_1$ -hh<sub>1</sub> TE matrix elements are shown in (a) and the  $e_1$ -lh<sub>1</sub> TM matrix elements are shown in (b) for various widths of a GaAs/Al<sub>0.3</sub>Ga<sub>0.7</sub>As well.

(a) *Thin-well e-hh transitions:* In thin wells, the wavefunctions of both carriers are almost entirely in the barriers, so the interband matrix elements of the well regions are nearly insignificant. Instead, the overall matrix element is dominated by the overlap of the carrier wavefunctions, which both get larger as the well intermixes due to the heavy-hole wavefunction spreading into the barrier faster than that of the electron. The result is that the matrix element gets larger as the well intermixes.

(b) *Thick-well e-hh transitions:* For thicker wells, significant parts of the carrier wavefunctions are in the well region, so the effect of the interband matrix elements becomes important. As the well intermixes, aluminum diffuses into the well, and the interband matrix elements in the well region decrease in value. At the same time, the overlap improves, but not as quickly as for thin wells, since the carriers are more confined in the thicker wells. These competing mechanisms result in an overall matrix element which is relatively constant.

(c) *Thin-well e-lh transitions:* As with the thin-well e-hh transition, the carrier wavefunctions are almost entirely in the barrier, even more so since the light-hole effective mass is less than that of the heavy hole. Therefore, the interband matrix element is dominated by the barrier and composition changes in the well are inconsequential. The overlap in this case is also nearly constant since the effective masses of the electrons and light holes are closely matched, producing envelope wavefunctions of nearly the same size and shape. Since both mechanisms result in very small changes, the overall matrix element remains nearly constant as well.

(d) *Thick-well e-lh transitions:* The overlap in this case changes only slightly because of the nearly matched electron and light hole masses as in the thinner wells. But since significant portions of the wavefunctions are confined in the well region, the composition dependence of the interband matrix elements is important, as in the

thick-well e-hh transitions. In this case, however, the overlap does not compete, so the interband matrix elements dominate the overall matrix element. As the well intermixes, the aluminum composition increases, and the overall matrix element decreases.

### 6.1.2 Lifetime Experiment

In order to test this theory, an experiment was devised in which ultrathin quantum wells of various thicknesses were annealed, and the spontaneous emission spectra and lifetimes were measured. The radiative lifetime is related to the Einstein relations as

$$\frac{1}{\tau} = A_{mn} = \frac{8\pi n^2 \bar{n} (h\nu)^2}{(hc)^3} B_{mn} \quad , \quad (6.13)$$

where  $A_{mn}$  is the probability for spontaneous emission,  $B_{mn}$  is the probability for stimulated emission,  $n$  is the index of refraction (which must be determined iteratively),  $\bar{n}$  is the group refractive index which accounts for dispersion,  $h$  is Planck's constant,  $c$  is the speed of light, and  $h\nu$  is the photon energy. Equation (6.13) assumes that the probabilities that the upper electronic state is empty and that the lower state is filled are both unity. The group index is given by

$$\bar{n} = n + \frac{h\nu}{e} \frac{dn}{d(h\nu/e)} \quad , \quad (6.14)$$

where  $e$  is the electronic charge. Finally,  $B_{mn}$  is given as

$$B_{mn} = \frac{e^2 h}{2m_0^2 \epsilon_0 n^2 (h\nu)} |M_{mn}|^2 \quad . \quad (6.15)$$

Several samples were grown by molecular beam epitaxy (MBE) with GaAs quantum wells of varying thickness ranging from 1 ML to 8 ML. The wells were in the center of a 1000-Å  $\text{Al}_{0.3}\text{Ga}_{0.7}\text{As}$  separate confinement heterostructure bound by  $\text{Al}_{0.4}\text{Ga}_{0.6}\text{As}$  barriers. The basic structure of these samples are shown in Figure 6.7. The samples were then annealed for various times. All samples were annealed at

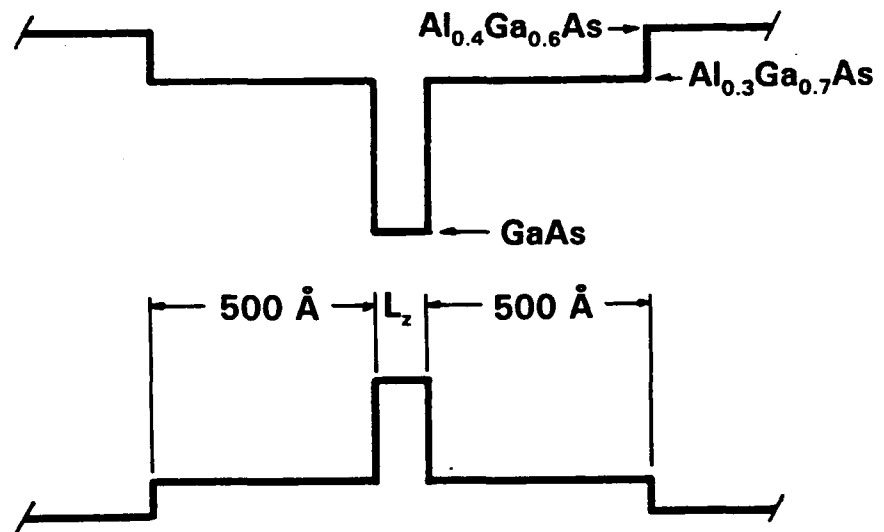


**Figure 6.5** Separate confinement heterostructure for ultrathin quantum wells. the outer barriers are  $\text{Al}_{0.4}\text{Ga}_{0.6}\text{As}$ , the inner barriers are  $\text{Al}_{0.3}\text{Ga}_{0.7}\text{As}$ , and the well is  $\text{GaAs}$ . The well widths,  $L_z$ , ranged from 1 ML to 8 ML in the lifetime experiments performed here.

850°C with one atmosphere As<sub>4</sub> overpressure, which resulted in an interdiffusion coefficient of  $8 \times 10^{-19}$  cm<sup>2</sup>s<sup>-1</sup>. The lifetime of each sample is inversely proportional to the emission energy and the matrix element, and should show a downward trend according to the theory. This trend was observed, but only after a sharp increase in the lifetime in the first 30 minutes of annealing as seen in Figure 6.8. Also, the calculated lifetimes were several times higher than experiment, which is not surprising since the effects of scattering are neglected in the theoretical calculation.

As for the sharp increase early in the annealing process, defects at the layer interfaces were most probably responsible. During the growth of the layers, a 10-second stop-growth was used in order to smooth out the layers.<sup>[81,82]</sup> In order to stop the growth, the shutters to the source furnaces in the MBE were closed. The molecular beams then heated the shutters, thereby outgassing impurities which had adsorbed on the surface of the shutters while they were cold. These impurities were then deposited on the epitaxial layer where they generated defects at the layer interfaces. During the first 30 minutes, the annealing process removed some of the defects while at the same time, smoothing out much of the interface roughness remaining despite the stop-growth.

For one sample in this set, all lifetimes were shifted up by about 200 ps. This was the 5-ML sample, and the growth record indicated that a gallium shutter was stuck open during one of the stop-growths. The growth conditions were otherwise identical to the rest of the samples in this set.

To determine if the lifetimes of the wells could be improved, a second set of samples was prepared using the same basic structure as the first set. The only differences were that the structures were grown without stopping between the layers, and the substrates were silicon-doped, as opposed to the previous set which were semi-insulating. Both changes were expected to reduce the number of defects at the layer interfaces and in the epitaxial layers as well.

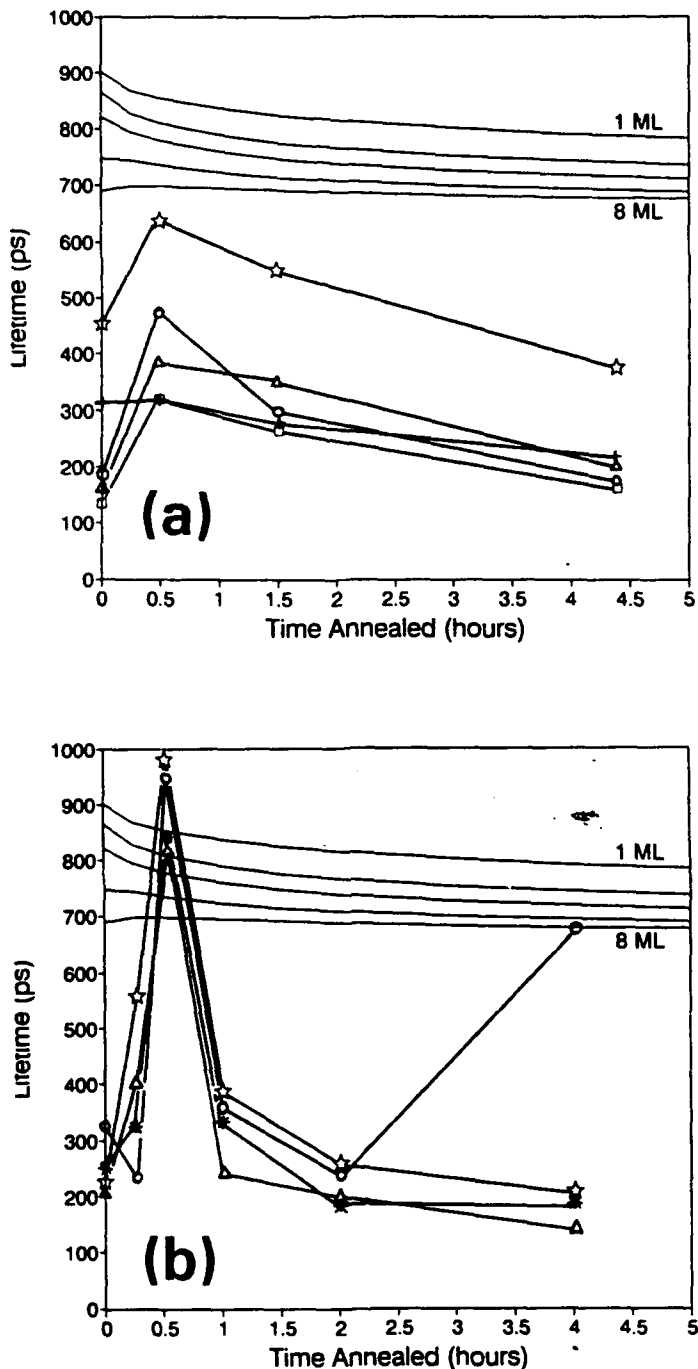


**Figure 6.6** Lifetimes of ultrathin GaAs/Al<sub>0.3</sub>Ga<sub>0.7</sub>As wells as a function of annealing time. The samples were annealed at 850°C in 1 atm As<sub>4</sub>. The data for the samples grown with a stop-growth are presented in (a), while the continuous-growth sample data are plotted in (b). Both have the theoretical lifetimes for comparison. The well widths correspond to the data as follows: plus = 1 ML, circle = 2 ML, triangle = 3 ML, square = 4 ML, star = 5 ML, and asterisk = 8 ML.

The data showed a slight increase in the as-grown lifetime, and a large increase in the lifetimes for all samples annealed for 30 minutes. Assuming that the number of impurities deposited at the layer interfaces was reduced without a stop-growth (some shutters still open and close at interfaces in order to change material composition, however), the as-grown lifetimes would be higher. However, the interfaces would be rougher in the second set of samples, thereby limiting the effect of the continuous growth. After annealing for 30 minutes, however, a dramatic increase in the lifetime was observed as the interface roughness was smoothed, which supports the assumption that there are fewer impurities deposited at the interfaces. The lifetime values at 30 minutes are also in the vicinity of the theoretical values, lending further support to this assumption.

The next 30 minutes of annealing yielded an interesting trend. Rather than following the curve for theoretical radiative lifetime, the observed lifetimes dropped sharply and approached the same values as the previous set of samples.

Several explanations of this trend are possible when it is examined in terms of non-radiative scattering. First, as the well intermixes, aluminum atoms move into the center of the well where the largest part of the carrier wavefunction can interact with the randomly fluctuating atomic potentials characteristic of the alloy. In other words, alloy scattering increases, which in turn decreases the overall lifetime of the carriers.

While alloy scattering is certainly a contributor to the trend seen in Figure 6.6, it is probably not the dominant one. If it were, the alloy scattering for the thinner wells would saturate sooner than in the thicker wells since most of their wavefunctions are in barriers, and the wells would fill with aluminum atoms faster. Such a trend is not evident in the data.

Another explanation based on non-radiative scattering that may explain the data is that, after about an hour, other types of defects diffuse into the area of the quantum wells. These defects could be gallium vacancies ( $V_{Ga}$ ) or arsenic antisite defects ( $As_{Ga}$ ) coming from the surface of the wafer, due to the  $As_4$  overpressure during the annealing process. Guido *et al.* showed that the quantum well intermixing rate was dependent on the depth of the well during an annealing step in an arsenic overpressure.<sup>[34]</sup> This indicated that the transport time of the defects from the surface had a role in determining the Al-Ga interdiffusion coefficient. They determined that the diffusion coefficients for the defects,  $D_{V_{Ga}}$  and  $D_{As_{Ga}}$ , were  $5 \times 10^{-12} \text{ cm}^2\text{s}^{-1}$  at  $825^\circ\text{C}$  with a 2-atm arsenic overpressure. The depth to which the defects diffused in 30 minutes is therefore on the order of  $1 \frac{3}{4} \text{ m}$  (10,000 Å), which is within a factor of two of the depth of the structures in this study. Similarly, they could be defects diffusing upward from the substrate. Further experiments are required to support this explanation. For instance, the well could be buried at various depths from the surface to determine when the sudden drop in lifetime occurs. If the drop occurs after longer annealing for deeper wells, then the explanation of defects coming from the surface would be supported.

A third explanation of the drop is possible by looking at the carrier dynamics between the bound states and the barrier, and then comparing their respective lifetimes. If, after an hour of annealing, the barrier became a sink for carriers, then the sudden drop in lifetime would be expected. In order for this to happen, the barrier lifetime would have to be much shorter than that of the well, and there would have to be a scattering mechanism present to kick the carriers to the barrier's higher energy level. This explanation of thermal scattering is plausible for 1- or 2-ML (and possibly 3-ML) wells, but for larger wells, the separation between the barrier and bound-state energies is several times the thermal energy at 77K. Therefore, another scattering mechanism must be considered.

Another problem with this third explanation is that if the short lifetime in the barriers was radiative, the barrier photoluminescence peak would be dominant, yet the well peak was always much stronger than that of the barrier. If the short barrier lifetime was due to non-radiative mechanisms, then the carriers would never get to the bound state and the photoluminescence peak at the bound state energy would be weak, when in fact the peak remained strong throughout the set of annealing points.

The most probable explanation of the sudden drop in the lifetime at about one hour of annealing is the second one given above. The transport of defects to the quantum well region probably yielded the data trend observed. This theory can be tested by performing a series of lifetime measurements on annealed samples with varying cladding layer thickness.

## 6.2 Damping Coefficient

The last variable needed to describe the dielectric function is the damping coefficient, which is defined by the spectral line width of the oscillator as  $2\gamma = \Delta\omega$ , where  $\Delta\omega$  is the full-width-at-half-maximum (FWHM) of the peak at the resonant frequency.

The line-width broadening is due to the finite lifetimes of the electronic states and is related to the lifetime through the Heisenberg Uncertainty Principle  $\hbar\Delta\omega\tau \approx \hbar$ ,<sup>[74]</sup> or

$$\gamma = \frac{\Delta\omega}{2} \approx \frac{1}{2\tau} . \quad (6.16)$$

If the lifetime is radiative only, then it is referred to as a natural broadening. This treatment neglects the effects of carrier scattering which may be important since the interaction time of collisions can be several orders of magnitude lower than the mean radiative lifetimes. Using Equations (6.13) to (6.16), the damping coefficient due to natural broadening is then

$$\gamma_{mn} = \frac{2\pi e^2}{\epsilon_0 m_0^2 \hbar^2 c^3} \bar{n}(\hbar\nu) |M_{mn}|^2 . \quad (6.17)$$

If non-radiative mechanisms are included, such as alloy scattering, then  $\gamma$  becomes

$$\gamma_{mn} = \frac{1}{2} \left[ \frac{1}{\tau_{rad}} + \sum_i \frac{1}{\tau_{nr,i}} \right] , \quad (6.18)$$

where  $\tau_{nr,i}$  are the non-radiative lifetimes, each of which is inversely proportional to the respective matrix elements for their processes.

### 6.3 Density of States

The oscillators over which the sum is taken in Equation (6.6) are transitions between the electronic states in the system. In a quantum well, each energy level has a corresponding density of electronic states, so if the dielectric response of each level is multiplied by the density of states (DOS) function and integrated over the energy, the dielectric constant as a function of energy becomes

$$\epsilon(E) = \epsilon_b(E) + \frac{\hbar^2 e^2}{m_0} \sum_{n,m} \int_{E_g}^{E_{nm}} \frac{f_{nm}}{(E_{nm}^2 - E^2) - i2\Gamma_{nm}E} \rho_{nm}(E' - E_g) dE' . \quad (6.19)$$

where  $\rho(E' - E_g)$  is the reduced DOS,  $\Gamma_{nm} = \hbar\gamma_{nm}$ , and the sum is now over the pairs of energy levels  $n$  and  $m$  between the conduction and valence bands, respectively. A distinction is made here between energy states and energy levels, where each level is a solution to the Schrödinger Wave Equation in the quantum well, and contains a number of states described by the DOS. Normally, the DOS for a quantum well is taken as a constant in energy, but the three-dimensional (3D) DOS can be used with the value of the bound energy level of the well used in the energy dependence (see Appendix C). To simplify the problem, the integral is taken over the DOS. By doing this, the number of oscillators contributing to each pair of energy

levels is determined, which allows the equation to retain the general form of Equation (6.6). The lineshape is broadened by  $\Gamma_{nm}$  which means the energy levels are actually spread into bands, but this approximation keeps the energy dependence in the dielectric response while greatly simplifying the calculations. The dielectric constant is then approximated by

$$\begin{aligned}
 \epsilon(E) &\approx \epsilon_b(E) + \frac{\hbar^2 e^2}{m_o} \sum_{n,m} \frac{f_{nm}}{E_{nm}^2 - E - i2\Gamma_{nm}E} \int_{E_g}^{E_{nm}} \frac{\mu^{\frac{3}{2}}}{\sqrt{2\pi^2\hbar^3}} (E' - E_g)^{\frac{1}{2}} dE' \\
 &= \epsilon_b(E) + \frac{\hbar^2 e^2}{m_o} \sum_{n,m} \frac{f_{nm}}{E_{nm}^2 - E - i2\Gamma_{nm}E} \frac{2}{3} \frac{\mu^{\frac{3}{2}}}{\sqrt{2\pi^2\hbar^3}} (E_{nm} - E_g)^{\frac{3}{2}} \\
 &= \epsilon_b(E) + \frac{\hbar^2 e^2}{m_o} \sum_{n,m} \frac{f_{nm}}{E_{nm}^2 - E - i2\Gamma_{nm}E} \frac{2}{3} (E_{nm} - E_g) \rho_{nm} \\
 &= \epsilon_b(E) + \frac{\hbar^2 e^2}{m_o} \sum_{n,m} \frac{N_{nm} f_{nm}}{E_{nm}^2 - E - i2\Gamma_{nm}E} ,
 \end{aligned} \tag{6.20}$$

where  $N_{nm}$  is the number of oscillators with the resonant energy  $E_{nm}$ . The function  $\rho_{nm}$  is the 2D DOS function derived in Appendix C without spin-degeneracy, and is given by

$$\rho_{nm} = \frac{1}{2} \frac{\mu}{\pi^2 \hbar^2} k_{nm} , \tag{6.21}$$

where  $\mu$  is the reduced mass of the combined carriers in the conduction and valence bands, which will be discussed shortly, and  $k_{nm}$  is the wavevector for the energy levels given by

$$k_{nm} = \frac{\sqrt{2\mu(E_{nm} - E_g)}}{\hbar} . \tag{6.22}$$

The energy gap,  $E_g$ , is between the bottom of the conduction band potential well and the bottom of the valence band well (highest absolute energy).

Since the material composition varies across the intermixed well, the effective mass should be the average value of the material at the bottom of the well and the barriers. This can be handled in the same manner as the interband matrix element, using the carrier wavefunction to weight the values of the mass for each region. In this case, however, only the individual wavefunctions are used instead of the overlap. For example,

$$\overline{m}_e^* = \sum_{i=0}^N (m_e^*)_i \int_i \Psi_e^* \Psi_e dz , \quad (6.23)$$

and

$$\frac{1}{\mu} = \frac{1}{\overline{m}_e^*} + \frac{1}{\overline{m}_h^*} . \quad (6.24)$$

Finally, for a superlattice, the DOS is also given by Equation (6.21), except  $k_{nm}$  is replaced by the superlattice wavevector  $q_{nm}$ , which is given by

$$q_{nm} = \frac{1}{a} \cos^{-1}(F(E)) , \quad (6.25)$$

since the superlattice dispersion relation is described by

$$\cos(q\alpha) = F(E) , \quad (6.26)$$

where  $\alpha$  is the period of the superlattice, and  $F(E)$  is a function of energy. For the intermixed superlattice,  $F(E)$  takes the form, previously derived in Section 4.3, of

$$F(E) = \frac{1}{2}(S_{11} + S_{22}) , \quad (6.27)$$

where  $S_{11}$  and  $S_{22}$  are elements of a transfer matrix that describes the superlattice period. The DOS for an intermixed superlattice is then

$$\rho_{nm} = \frac{\mu}{\pi^2 \hbar^2} \frac{1}{a} \cos^{-1} \left\{ \frac{1}{2}(S_{11} + S_{22}) \right\} . \quad (6.28)$$

## 6.4 Index of Refraction

The index of refraction of an intermixed quantum well as function of photon energy,  $E = \hbar \omega$ , is

$$n(E) = Re \left\{ \sqrt{\frac{\epsilon(E)}{\epsilon_0}} \right\} , \quad (6.29)$$

where  $\epsilon(E)$  is given by Equation (5.20). The background dielectric function defined earlier includes the effects of the barrier oscillators which do not change as the quantum well is annealed. If the frequency range of interest is far enough away from the spectral features of the background dielectric constant, then the background constant will be real. In the case of a quantum well, the background dielectric constant can be taken from the barrier material using an empirically determined index of refraction given by<sup>[63]</sup>

$$n^2 = A(x) + \frac{B}{\lambda_0^2 - C(x)} - D(x)\lambda_0^2 , \quad (6.30)$$

where  $x$  is the aluminum fraction in the  $Al_xGa_{1-x}As$  alloy,  $\lambda_0$  is the free-space wavelength in microns, and

$$A = 10.9060 - 02.92x$$

$$B = 0.97501$$

$$C = (0.52886 - 0.735x)^2 ; \quad x \leq 0.36$$

$$C = (0.30386 - 0.105x)^2 ; \quad x > 0.36$$

$$D = 0.002467(1 + 1.41x) .$$

The background dielectric constant is then given by  $\epsilon_b = \epsilon_0 n^2$ , and is a function of  $\lambda_0$  or  $E$ .

A potential problem with this method occurs when the bound states are near the top of the well, as with a 1- or 2-ML well, where  $\epsilon_b$  may be complex and can no longer be described by the index of refraction. However, if the spectral range of interest for passive waveguides is far enough away from the absorption edge of the barrier, this method should still be valid. For a passive waveguide to have acceptable losses, the frequency of the guided light must be far enough below the absorption edge of the bound state, which therefore places the frequency below the absorption edge of the barrier. As long as the dielectric properties in the barrier remain unchanged with annealing, all changes at the desired frequency will be due to changes in the bound state.

The refractive index of a 5-ML GaAs/Al<sub>0.3</sub>Ga<sub>0.7</sub>As quantum well as a function of energy for several annealing times was calculated and the results are presented in Figure 6.9. Only the effects of  $n=m=1$  e-hh transition are shown since their influence is the greatest for the energies of interest.

The abscissa covers the energies between the bottom of the as-grown well and the barrier with the lowest-energy e-hh transition of the as-grown well labeled. As the well intermixes, the transition energy increases since the bottom of the well fills in as the aluminum composition increases. The widths of the peaks at the resonance points are a function of the damping coefficient for each discrete energy level as calculated above. This is for the ideal case where the energy level is not spread out at all and the damping coefficient is due to natural linewidth broadening only. The effects of thermal broadening is shown in Figure 6.7 (b) where the damping coefficient,  $\Gamma_{11}$ , is replaced with the thermal energy at 77K (6 meV). The effects this has on the index are isolated near the resonance, so as long as this region is avoided, the actual index will be well described by the ideal theoretical case.

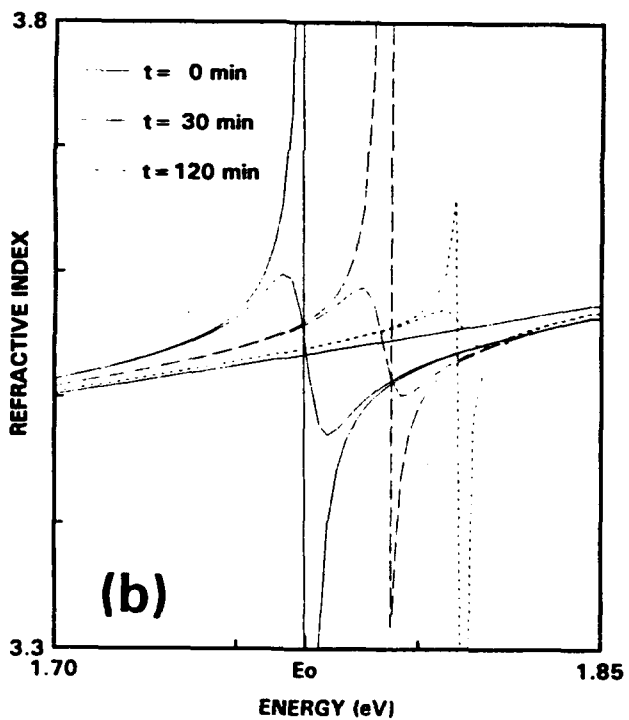
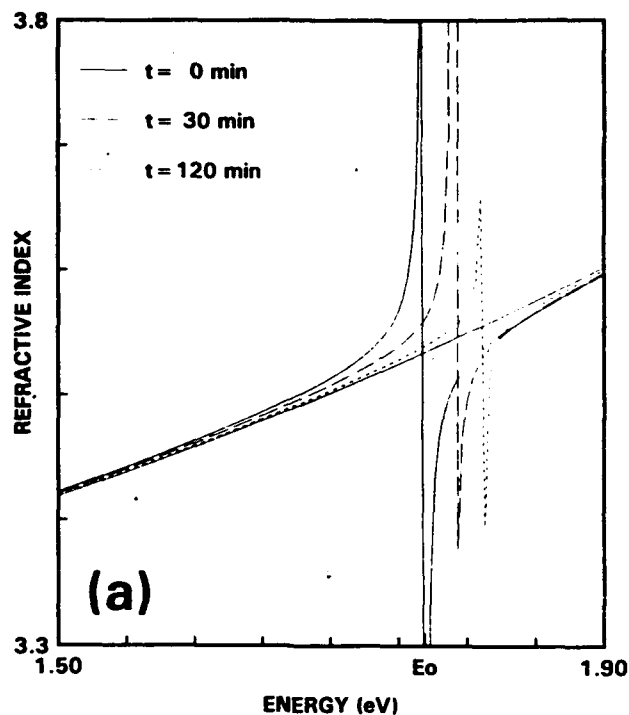


**Figure 6.7** Refractive index for an intermixed  $\text{GaAs}/\text{Al}_{0.3}\text{Ga}_{0.7}\text{As}$  quantum well. The index for a 5 ML well as grown (solid curve) and annealed for 30 minutes (dot-dash) and 120 minutes (short dashed) is shown in (a) for the energy range between the GaAs and barrier band edges. The effects of thermal lineshape broadening are included in (b) to point out that the index does not change except in the immediate vicinity of the oscillator.

Another trend to note is the decrease in the strength of the resonance as it approaches the barrier energy. While this is difficult to quantify in Figure 6.7 (a) due to the selection of plotting points near the sharp resonances, the thermally-broadened curves in Figure 6.7 (b) show this well. This makes intuitive sense because the index will eventually become that of the barrier as the well becomes completely intermixed. This is probably not a function of oscillator strength because the oscillator in the denominator increases only slightly with annealing time, which is offset by the increased matrix element in the numerator. Instead, the trend is due to the decrease in the density of oscillators at the resonant frequency as described in Equation (6.20). This number is proportional to the difference between the energy level and the bottom of the well which decreases as the well fills in.

In this particular example, if the emission energy of GaAs (1.508 eV) is assumed, then the index of refraction for a 30-minute annealing step is 3.4231, and a 120-minute annealing step results in an index of 3.4217. While these values represent different times  $t$  with the same interdiffusion coefficient  $D$ , they could also represent the same annealing times with different interdiffusion coefficients since the amount of intermixing depends on the product  $Dt$ . In that case, this example could be used to represent a selective intermixing process with a 4:1 selectivity ratio. The index difference between the "preserved" and "intermixed" regions would then be 0.0014 (0.04%), which is less than half that of the ideal case of 0.0034 (0.1%) where the well is either completely preserved or completely intermixed.

By selectively intermixing a 5-ML quantum well with a 4:1 selective interdiffusion coefficient ratio, an optical waveguide can be formed. Using the data above, the electric field distribution for a 5- $\frac{3}{4}$ m-wide waveguide would look like that shown in Figure 6.10. Such a waveguide could be useful in a directional coupler where two waveguides are placed in close proximity so that the electric field modes overlap

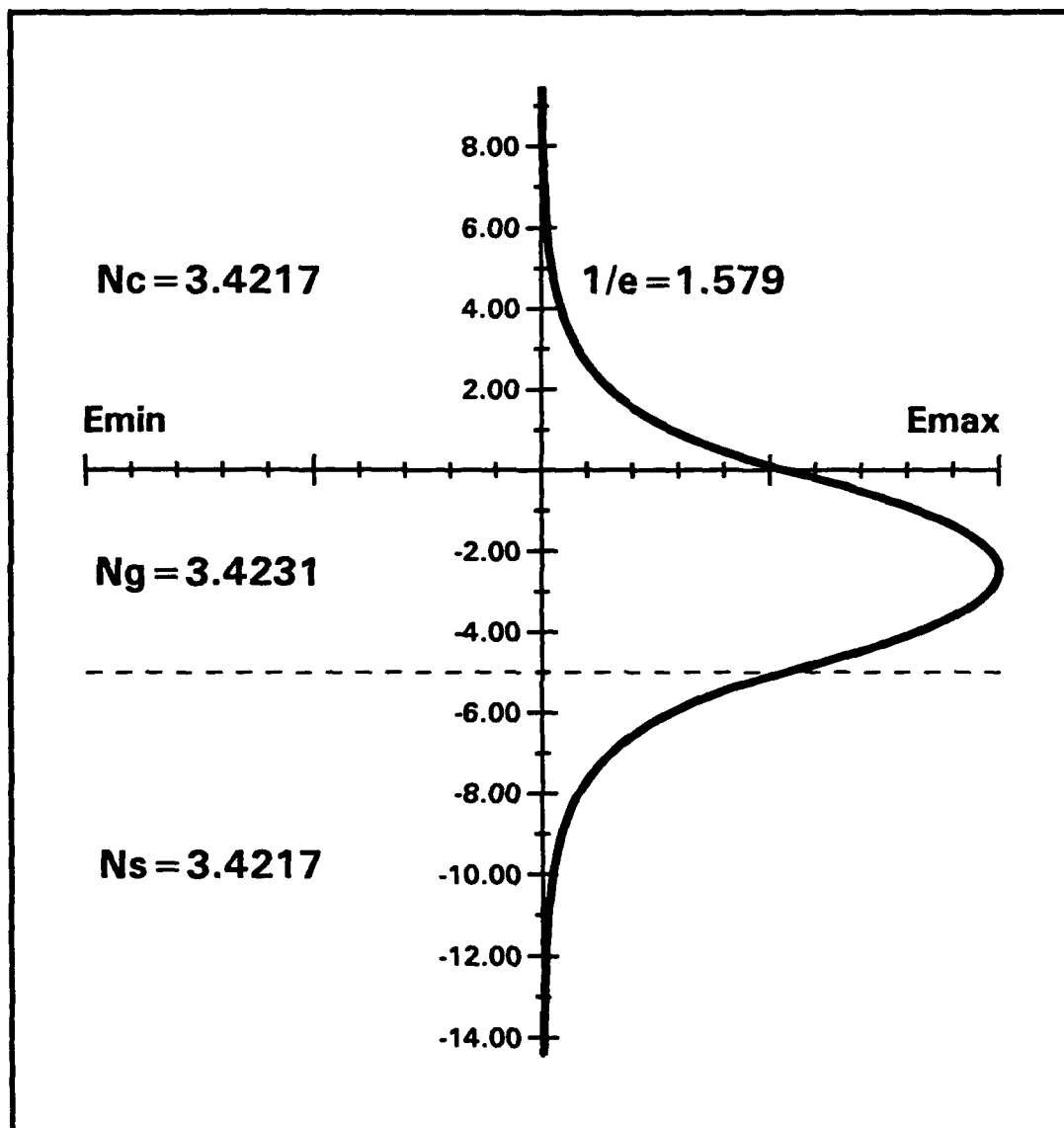


**Figure 6.8** Electric field distribution for an optical waveguide defined by selective intermixing. The indices of refraction are based on a 4:1 selectivity ratio of the interdiffusion coefficients in the cladding and guide regions. The as-grown quantum well is 5 ML wide and the waveguide is 5  $\mu\text{m}$  wide.

and power is transferred between guides. The coupling length for such a device, which is the distance that the optical field must propagate in order to transfer all power from one guide to the other, is given by

$$L = \frac{\pi}{2\kappa_c} + \frac{m\pi}{\kappa_c} \quad (6.31)$$

where  $\kappa_c$  is the coupling coefficient, and  $m$  is the mode number for the transverse electric (TE<sub>m</sub>) waveguide mode. The coupling coefficient is defined by the overlap of one waveguide mode with the evanescent tail of the adjacent waveguide mode.<sup>[83]</sup> If the overlap is small enough to be treated as a perturbation, then the coupling coefficient for a coupler with propagation in the x-direction and guide separation in the y-direction is given by<sup>[84]</sup>

$$\kappa_c = \frac{2\beta_y^2}{y_0\beta_x W(y_0^{-2} + \beta_y^2)} e^{-\frac{s}{y_0}} \quad (6.32)$$

where  $\beta_y$  is the mode propagation coefficient in the y-direction,  $\beta_x$  is the propagation coefficient in the x-direction,  $y_0$  is the  $1/e$  point of the evanescent field,  $W$  is the width of the waveguides, and  $s$  is the separation between them. The length of a 3 dB coupler, which splits the power evenly between the waveguides, for a TE<sub>0</sub> mode is shown in Figure 6.11.

For a reasonable 5-7 m separation, the splitter would need to be 310-340 m long to transfer 50% of the optical power between waveguides, which is also reasonable for integrated optics. Shorter lengths can be easily obtained, but the control over the length becomes more difficult, and variations in length become more critical to the coupling ratio. This is just a single example of how selectively intermixed quantum wells can be used in integrated optics.

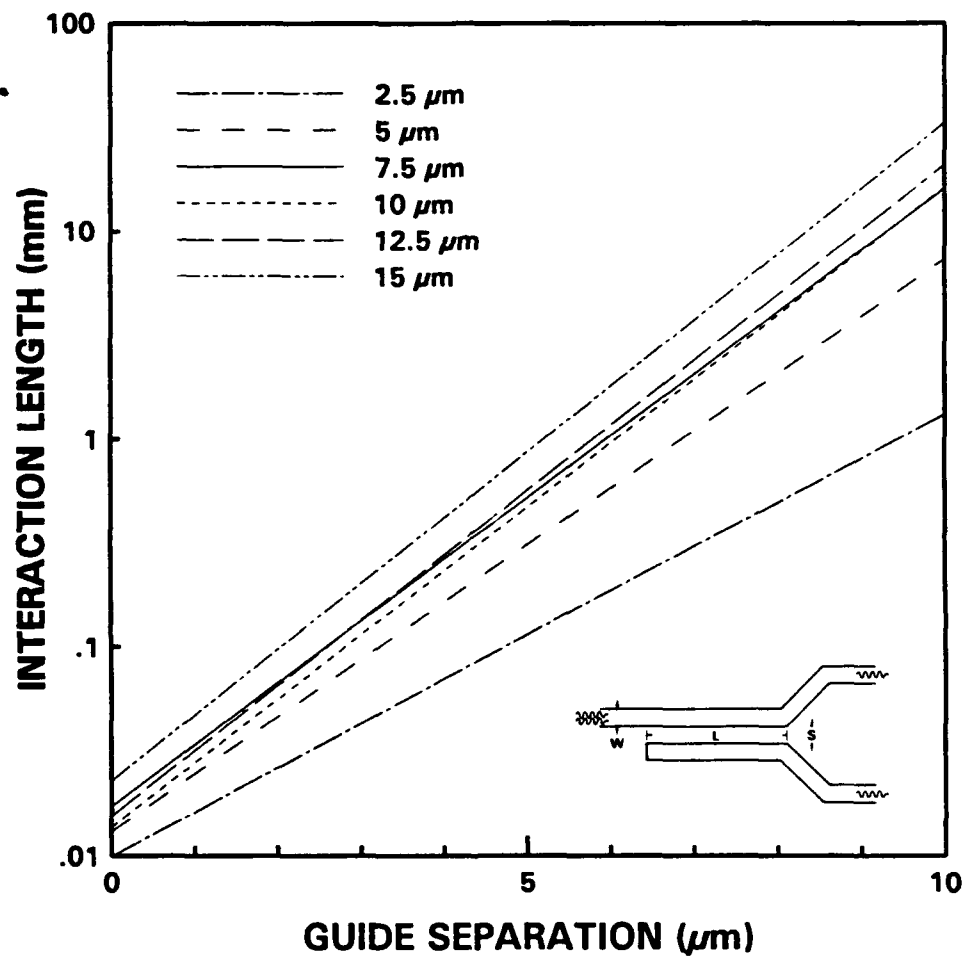


**Figure 6.9** Interaction length of a 3 dB optical waveguide coupler designed with disorder-defined waveguides. The waveguides are comprised of selectively intermixed 5 ML GaAs/Al<sub>0.3</sub>Ga<sub>0.7</sub>As quantum wells. The waveguide widths are indicated in the legend, and the interaction length for 50% power transfer between the guides is given as a function of guide separation for each case. The inset shows a schematic of the device.

## 7 The Trek

This final chapter is a review of this research endeavor. It begins with a summary of the work performed. The next section outlines the specific conclusions drawn from the various experiments and calculations presented earlier. Finally, recommendations are made to the enterprising engineer who would use this thesis as a starting point for designing integrated optical circuits based on thermally intermixed quantum wells and superlattices.

### 7.1 Voyages

This research has focused on quantifying the changes of the optical properties of quantum wells and superlattices due to the thermal interdiffusion of the heterostructure interfaces. Various interdiffusion experiments were performed and characterized using photoluminescence (PL) techniques and theoretical models in order to develop a new model that describes the changes. A summary of this study is presented here, emphasizing the original research performed.

The potential well shape resulting from heterostructure intermixing was examined in Chapter 4. It started with the refinement of a computer model to include an error function shape in studying intermixed heterostructure interfaces (Section 4.1). Further improvements in the model's speed were achieved with a thoughtful scheme of dividing the intermixed well. The scheme presented yielded greater accuracy for the same number of divisions. The validity of the error function composition profile was then questioned, and an experiment was performed to determine if the Al-Ga interdiffusion coefficient is dependent on aluminum composition (Section 4.2). A computer model was developed which used a composition-dependent interdiffusion coefficient, and

simulations were compared to the experimental results. While a small compositionally dependent trend was observed, the differences were within the experimental error and deemed insignificant within the conditions of the experiment.

The next section examined models to calculate the energy dispersion relations of superlattices (Section 4.3). A one-dimensional tight-binding calculation in the envelope-function approximation was studied first, but this method was limited to weakly coupled wells. A Kronig-Penney type calculation was examined next. This model was able to handle strongly coupled wells, and was successfully adopted to thermally intermixed superlattices using error-function-shaped interfaces.

Chapter 5 addressed several potential techniques to selectively control the interdiffusion process. First, the use of gallium ions implanted near the surface to create a local gallium overpressure was studied (Section 5.1). A gallium focused ion beam (FIB) was used to selectively implant ions into the surface near (not in) a GaAs/AlGaAs superlattice, and the samples were annealed. PL was used to measure the changes in energy with and without the implanted ions. The results suggested that the implant generated mobile defects which served to preserve the superlattice in and around the implanted areas. This led to a side experiment to ascertain the effects of different ambient overpressures on the mobility of electrons in a high-electron-mobility transistor (HEMT) structure. The nature of the structure, however, prevented the conclusive determination of the effects of the overpressure. A more appropriate experiment was proposed based on the availability of an FIB apparatus.

The next method of selective intermixing examined was the use of  $\text{SiN}_x$  as an encapsulant to preserve the morphology of the surface (Section 5.2). A GaAs/AlAs superlattice was prepared, and  $\text{SiN}_x$  stripes were patterned on the surface. The sample was annealed and the PL peak shifts were measured. This method provided a suitable selectivity between the covered and uncovered stripes.

Finally, arsenic-rich GaAs grown at low substrate temperature (LT-GaAs) was considered as a source of local arsenic overpressure (Section 5.3). An LT-GaAs layer was grown and patterned on a GaAs substrate, then reloaded into the molecular beam epitaxy machine for subsequent layer growth. The sample was then annealed and the PL peak shifts showed a trend verifying that the LT-GaAs stripes enhanced the Al-Ga interdiffusion coefficient. Although the processing techniques need refinement, this proof-of-concept experiment demonstrated that this is a possible method of selective intermixing.

The primary emphasis of this thesis was chronicled in Chapter 6. After a brief overview of the relationships between the various optical properties and origin of the dielectric constant, a model for the optical matrix element was developed (Section 6.1). The matrix element based on the Kane model was discussed, and the theory was extended to include the effects of the electron-hole envelope wavefunctions in thin wells, as well as the effects of varying interband matrix elements between the well and barriers. The new model was then applied to thermally intermixed quantum wells. Simulations based on the models were performed and the radiative electron-hole recombination lifetimes were calculated. These simulations were compared to time-resolved PL of thermally annealed thin wells. The data, however, was masked by what was probably non-radiative defects that were transported into the structure from the surface during the annealing process.

The damping coefficient was calculated next using a simple model describing the natural linewidth broadening (Section 6.2). The derivation of the dielectric constant for intermixed wells was then completed using a modified density of states function (Section 6.3). The density of states function for a superlattice was then formulated based on a previous calculation of the energy dispersion relation.

The chapter culminated with the first-ever calculation of the index of refraction of a partially intermixed quantum well (Section 6.4). A 5-monolayer (ML) well was used as an example, and the index difference was calculated for a selective intermixing case. The example was extended by including the intermixed wells in an optical waveguide, calculating the electric field distribution, and modeling a 3-dB power splitter. The calculation was presented as an example of using realistic values of indices of refraction of partially intermixed wells in a useful integrated optical device.

## 7.2 Where No One Has Gone Before

The following is list of conclusions which can be drawn from the work performed in this thesis.

- (a) Compositional dependence of the Al-Ga interdiffusion coefficient is negligible at 850°C with 1 atm As<sub>4</sub> overpressure. While a slight dependence is evident, it is within the experimental error. Higher temperatures, however, may exhibit a stronger dependence.
- (b) The accuracy of a numerical solution of the Schrödinger Wave Equation in an error-function-shaped potential well is improved if the finite regions of the well are chosen such that there are more regions in areas of rapidly varying potential.
- (c) Energy levels of quantum wells with widths between 8 and 10 ML (20 and 30 Å) are the most sensitive to thermal annealing. The energy levels of thinner wells tend to saturate near the barrier, and levels in thicker wells rely on the well to fill in before they shift in energy.
- (d) SiN<sub>x</sub> can be used to selectively mask areas of a quantum well or superlattice from overpressure-enhanced intermixing. The minimum feature sized, however, has yet to be determined.

- (e) Patterned GaAs grown at low substrate temperature (LT-GaAs) can be used as a localized "arsenic overpressure" to enhance intermixing. Additional work is needed to improve the fabrication process in order to determine how much interdiffusion enhancement is possible.
- (f) The electron-to-heavy-hole (e-hh) envelope wavefunction overlap is critical to the optical matrix element of thin quantum wells. The interband matrix elements of both the well and the barriers are also important when significant portions of the wavefunctions are in each.
- (g) The optical matrix element for e-hh transitions in ultrathin quantum wells gets larger as the wells are thermally intermixed. This is primarily due to the improvement in the carrier wavefunction overlap. This effect also translates to a theoretical reduction in the radiative lifetime of the wells.
- (h) The refractive indices of a selectively intermixed quantum well are somewhere between that of a completely intermixed well and a completely preserved well. The index difference between the preserved and intermixed areas is then much less than between the two extremes, which is important when applied to the design of a device, such as an optical waveguide.

The overall conclusion of this thesis is that the optical properties of quantum wells and superlattices can be altered through selective intermixing, and the resulting differences are large enough to be used in integrated optical applications. This work quantifies, for the first time, these changes in relation to the extent of intermixing the quantum well experiences. While there are several more elaborate theories that describe the optical properties of both quantum wells and bulk material, this work bridges the gap between them, which is essential if selective intermixing is to become a

useful technology. From here, then, design rules can begin to emerge which govern the fabrication of integrated optical components that take advantage of the unique properties of quantum wells and superlattices.

### 7.3 The Continuing Mission

While this thesis is a significant advancement in the science of the optical properties of semiconductor quantum structures, more work is required to make it a complete technology. This section contains recommendations which will build on this thesis and approach such a level. Explicit suggestions for individual experiments to improve the work can be found in the body of this document, while this section is reserved for more general recommendations.

Two recommendations are made from an experimental standpoint. The first is to find an optimum method of selectively controlling the intermixing process. The techniques tested here are just a few of the possible candidates. While  $\text{SiN}_x$  encapsulation shows the most promise, its limits need to be tested, and other methods should be considered, or perhaps, combined for the best results.

The second experimental recommendation is to fabricate some integrated optical devices, such as the one described in Section 5.4, in order to test the theory. This, of course, applies to any extensions of this theory as well.

On the theoretical side, other effects can be factored into the model. These may include the effects of X and L band transitions (especially at higher aluminum composition), the inclusion of non-radiative scattering processes (such as phonons) in the calculation of the lifetime and damping coefficient, or excitons for low-temperature, low-carrier-excitation applications.

Another possibility is to extend the basic theory to include electro-optic effects. These effects are useful in such devices as integrated optical interferometers, bistable devices, spatial light modulators, and self-electro-optic devices (SEED's). This particular recommendation would be especially well-complemented by appropriate experimental investigations.

These are just a few suggestions of research that builds on this study. This dissertation should serve as a good starting point for an investigation of any of these, or any other studies which are concerned with the optical properties of intermixed quantum wells and superlattices.

## 8 References

1. L. Esaki and L.L. Chang, *Phys. Rev. Lett.*, **33**, 495 (1974).
2. R. Dingle, W. Wiegmann, and C.H. Henry, *Phys. Rev. Lett.* **33**, 827 (1974).
3. For a review of quantum well and superlattice devices, see for example: *Semiconductors and Semimetals*, Vol. 24, Ed. by R.K. Willardson, and A.C. Beer (Academic Press, New York, 1987); C. Weisbuch and B. Vinter, *Quantum Semiconductor Structures: Fundamentals and Applications*, (Academic Press, New York, 1991).
4. N. Holonyak, Jr., R.M. Kolbas, R.D. Dupuis, and P.D. Dapkus, *IEEE J. Quantum Electron.*, **QE-16**, 170 (1980).
5. W. Streifer, D.R. Schreifer, and R.D. Burnham, *Appl. Opt.*, **18**, 3547 (1979).
6. W.D. Ladig, N. Holonyak, Jr., M.D. Camras, K. Hess, J.J. Coleman, P.D. Dapkus, and J. Bardeen, *Appl. Phys. Lett.*, **38**, 776 (1981).
7. N. Holonyak, Jr., W.D. Ladig, M.D. Camras, J.J. Coleman, and P.D. Dapkus, *Appl. Phys. Lett.*, **39**, 102 (1981).
8. D.G. Deppe, K.C. Hsieh, N. Holonyak, Jr., R.D. Burnham, and R.L. Thornton, *J. Appl. Phys.*, **58**, 4515 (1985).
9. R.L. Thornton, R.D. Burnham, T.L. Paoli, N. Holonyak, Jr., and D.G. Deppe, *Appl. Phys. Lett.*, **48**, 7 (1986).
10. F. Julien, P.D. Swanson, M.A. Emanuel, D.G. Deppe, T.A. DeTemple, J.J. Coleman, and N. Holonyak, Jr., *Appl. Phys. Lett.*, **50**, 866 (1987).
11. R.G. Hunsperger, *Integrated Optics: Theory and Technology*, 2nd Ed. (Springer Verlag, New York, 1984).
12. K.Y. Hsieh, Y.C. Lo, J.H. Lee, and R.M. Kolbas in *GaAs and Related Compounds, Atlanta, Georgia, 1988*, *Inst. Phys. Conf. Ser.*, No. 96, 393 (1989).
13. K.V. Vaidyanathan, M.J. Helix, D.J. Wolford, B.G. Streetman, R.J. Blattner, and C.A. Evans, Jr., *J. Electrochem. Soc.* **124**, 1781 (1977).
14. L.J. Guido, N. Holonyak, Jr., K.C. Hsieh, R.W. Kaliski, W.E. Plano, R.D. Burnham, R.L. Thornton, J.E. Epler, and T.L. Paoli, *J. Appl. Phys.* **61**, 1372 (1987).
15. Y. Hirayama, Y. Suzuki, S. Tarucha, and H. Okamoto, *Jpn. J. Appl. Phys.* **24**, L516 (1985).
16. J. Cibert, P.M. Petroff, D.J. Werder, S.J. Pearton, A.C. Gossard, and J.H. English, *Appl. Phys. Lett.* **49**, 223 (1986).
17. Y. Suzuki, and H. Okamoto, *J. Electron. Mat.* **12**, 397 (1983).

18. J.P. Leburton, K. Hess, N. Holonyak, Jr., J.J. Coleman, and M. Camras, *J. Appl. Phys.* **54**, 4230 (1983).
19. K.B. Kahan and J.P. Leburton, *Phys. Rev. B* **33**, 5465 (1986).
20. K.B. Kahan, and J.P. Leburton, *Phys. Rev. B* **32**, 5177 (1985).
21. D.W. Jenkins, *J. Appl. Phys.* **68**, 1848 (1990).
22. D.G. Deppe, and N. Holonyak, Jr., *J. Appl. Phys.* **64** R93 (1988).
23. P. Mei, H.W. Yoon, T. Venkateson, S.A. Schwarz, and J.P. Harbison, *Appl. Phys. Lett.* **50**, 1823 (1987).
24. T.Y. Tan and U. Gösele, *Appl. Phys. Lett.* **52**, 1240 (1988).
25. T.Y. Tan, U. Gösele, and S. Yu, *Critical Rev. In Solid State Mater. Sci.* **17**, 47 (1991).
26. G.A. Baroff and M. Schluter, *Phys. Rev. Lett.* **55**, 1327 (1985).
27. B. Goldstein, *Phys. Rev. B* **121**, 1305 (1961).
28. L.L. Chang and A. Koma, *Appl. Phys. Lett.* **29**, 138 (1976).
29. Y.L. Hwang, K.Y. Hsieh, J.H. Lee, T. Zhang, U.K. Mishra, and R.M. Kolbas, *Proceedings of the 6th International Conference on Semi-Insulating III-V Compounds*, Montreal, Canada (1989).
30. M. Kaminiska, Z. Lilienthal-Weber, E.R. Weber, T. George, J.B. Kortright, F.W. Smith, B.-Y. Tsaur, and A.R. Calawa, *Appl. Phys. Lett.* **54**, 1881 (1989).
31. K.Y. Hsieh, Ph.D. Dissertation, North Carolina State University (1990).
32. D.G. Deppe, L.J. Guido, N. Holonyak, Jr., K.C. Hsieh, R.D. Burnham, and R.L. Thornton, *Appl. Phys. Lett.* **49**, 510 (1986).
33. J. Kasahara, Y. Kato, M. Arai, and N. Watanabe, *J. Electrochem. Soc.* **130**, 2275 (1983).
34. L.J. Guido, N. Holonyak, Jr., K.C. Hsieh, and J.E. Baker, *Appl. Phys. Lett.* **54**, 262 (1989).
35. E.S. Koteles, B. Elman, C.A. Armiento, P. Melman, J.Y. Chi, R.J. Holstrom, J. Powers, D. Owens, S. Charbonneau, and M.L.W. Thewalt, *J. Appl. Phys.* **66**, 5532 (1989).
36. Y. Hirayama, Y. Suzuki, S. Tarucha, H. Okamoto, *Jpn. J. Appl. Phys.* **28**, L162 (1989).
37. B. Elman, E.S. Koteles, P. Melman, and C.A. Armiento, *J. Appl. Phys.* **66**, 2104 (1989).

38. Y.J. Yang, Y.C. Lo, G.S. Lee, K.Y. Hsieh, and R.M. Kolbas, *Appl. Phys. Lett.* **49**, 835 (1986).

39. K. Ishida, M. Matsui, T. Fukunaga, T. Takamori, J. Kobayashi, K. Ishida, and H. Nakashima, *GaAs and Related Compounds, Las Vegas, Nevada, 1986 (Inst. Phys. Conf. Ser. No. 83, 1987)* p. 361.

40. D.F. Welch, D.R. Scifres, P.S. Cross, and W. Streifer, *Appl. Phys. Lett.* **51**, 1401 (1987).

41. R.D. Burnham, R.L. Thornton, N. Holonyak, Jr., J.E. Epler, and T.L. Paoli, *GaAs and Related Compounds, Las Vegas, Nevada, 1986, (Inst. Phys. Conf. Ser. No. 83, 1987)* p. 9.

42. Y. Hirayama, Y. Suzuki, H. Iguchi, S. Tarucha, and H. Okamoto, *Electronic Materials Conference, Amherst, 1986*, N-7 (Referenced in Y. Suzuki and H. Okamoto, *Jpn. J. Appl. Phys.* **25**, L912 (1986)).

43. See for example: R.J. Borg and G.J. Dienes, *An Introduction to Solid State Diffusion*, (Academic Press, New York, 1988).

44. J. Crank, *The Mathematics of Diffusion*, 2nd Ed. (Oxford, New York, 1975).

45. R.M. Fleming, D.B. McWhan, A.C. Gossard, W. Wiegmann, and R.A. Logan, *J. Appl. Phys.* **51**, 357 (1980).

46. R.M. Kolbas and N. Holonyak, Jr., *Am. J. Phys.* **52**, 431 (1984).

47. M.D. Camras, N. Holonyak, Jr., R.D. Burnham, W. Streifer, D.R. Scifres, T.L. Paoli, and C. Lindstrom, *J. Appl. Phys.* **59**, 5637 (1983).

48. S. Flugge, *Practical Quantum Mechanics*, (Springer, Berlin, 1971), pp. 94-100.

49. J.F. Holt, *Commun. A.C.M.* **7**, 366 (1964).

50. S.E. Koonin, *Computational Physics*, (Benjamin/Cummings, New York, 1985) p. 15.

51. P. Voisin, G. Bastard, and M. Voos, *Phys. Rev. B* **29**, 935 (1984).

52. G. Bastard in *Molecular Beam Epitaxy and Heterostructures*, L.L. Chang and K. Ploog, eds. (Martinus Nijhoff, Boston, 1985) p. 381.

53. H. Rucker, M. Hanke, F. Bechstedt, and R. Enderlein, *Superlatt. Microstructures* **2**, 477 (1986).

54. See, for example: C. Kittel, *Introduction to Solid State Physics*, 6th Ed. (Wiley, New York, 1986) pp. 164-166.

55. G. Bastard, *Phys. Rev. B* **24**, 5693 (1981).

56. P. Yuh and K.L. Wang, *Phys. Rev. B* **38**, 13307 (1988).

57. R.L. Kronig, *J. Opt. Sci. Am.* **12**, 547 (1926).
58. H.A. Kramers, *Atti. Congr. Intern. Fis.* **2**, 545 (1927).
59. H.C. Casey, Jr., D.D. Sell, and M.B. Panish, *Appl. Phys. Lett.* **24**, 63 (1974).
60. D.E. Aspnes, S.M. Kelso, R.A. Logan, and R. Bhat, *J. Appl. Phys.* **60**, 754 (1986).
61. B.O. Seraphin and H.E. Bennett in *Semiconductors and Semimetal: Vol. 3, Optical Properties of III-V Compounds*, R.K. Willardson and A.C. Beer, eds. (Academic Press, New York, 1967) p. 515.
62. S. Adachi, *J. Appl. Phys.* **58**, R1 (1985).
63. R.G. Hunsperger, *ibid.*, p. 61.
64. B. Jensen and W.D. Jensen, *IEEE J. Quantum Electron.* **QE-27**, 40 (1991).
65. S. Adachi, *Phys. Rev. B* **35**, 7454 (1987).
66. Y.C. Chang and J.N. Schulman, *Phys. Rev. B* **31**, 2069 (1985).
67. E.O. Kane, *J. Phys. Chem. Solids* **1**, 249 (1956).
68. R. Tsu and L. Ioriatti, *Superlatt. Microstructures* **1**, 295 (1985).
69. See, for example: S. Datta, *Quantum Phenomena*, Modular Series on Solid State Devices, Vol. 8, R.F. Pierret and G.W. Neudeck, eds. (Addison-Wesley, Reading, MA, 1989) p. 215.
70. G. Lasher and F. Stern, *Phys. Rev.* **133**, A553 (1964).
71. H.C. Casey, Jr., and M.B. Panish, *Heterostructure Lasers: Part A, Fundamental Principles*, (Academic Press, New York, 1985) p. 146.
72. G. Bastard in *Molecular Beam Epitaxy and Heterostructures*, L.L. Chang and K. Ploog, eds. (Martinus Nijhoff, Boston, 1985) pp. 391-2.
73. G.J. Sonek, J.M. Ballantyne, Y.J. Chen, G.M. Carter, S.W. Brown, E.S. Koteles, and J.P. Salerno, *IEEE J. Quantum Electron.* **QE-22**, 1015 (1986).
74. J.T. Verheyen, *Laser Electronics* (Prentice Hall, Englewood Cliffs, NJ, 1981) pp. 144-5.
75. N. G. Andersen, Ph.D Dissertation, North Carolina State University (1988).
76. S.D. Benjamin, Masters Thesis, North Carolina State University (1988).
77. W.H. Press, B.P. Flannery, S.A. Teukolsky, and W.T. Vetterling, *Numerical Recipes, the Art of Scientific Computing (Fortran)*, (Cambridge University Press, New York, 1989).

78. J. Crank, *ibid.*, p. 170.
79. Y.C. Chang and J.N. Schulman, *Appl. Phys. Lett.*, **43**, 536 (1983).
80. S.D. Benjamin, Ph.D. Dissertation, North Carolina State University (1991).
81. R.C. Miller, C.W. Tu, S.K. Sputz, and R.F. Kopf, *Appl. Phys. Lett.* **49**, 1245 (1986).
82. J. Zhang, P. Dawson, J.H. Neave, K.J. Hugill, I. Galbraith, P.N. Fawcett, and B.A. Joyce, *J. Appl. Phys.* **68**, 5595 (1990).
83. H. Nishihara, M. Haruna, and T. Suhara, *Optical Integrated Circuits*, (McGraw Hill, New York, 1989) p. 49.
84. R.G. Hunsperger, *ibid.*, p. 113.
85. H. Haug and S.W. Koch, *Quantum Theory of the Optical and Electronic Properties of Semiconductors*, (World Scientific, NJ, 1990), p. 22.
86. J.T. Verheyen, *ibid.*, p. 165.
87. M. Krahl, J. Christen, D. Binberg, D. Mars, J. Miller, *IEEE J. Quantum Electron.*, **QE-25**, 2281 (1989).
88. D.Y. Smith in *Handbook of Optical Constants of Solids*, E.D. Palik, Ed. (Academic Press, 1985) p. 45.
89. M.W. Prairie and R.M. Kolbas, *Superlatt. Microstructures*, **7**, 269 (1990).
90. M. Asada, A. Kameyama, and Y. Suematsu, *IEEE J. Quantum Electron.* **QE-20**, 745 (1984).
91. S. Datta, *ibid.*, Chap. 6, 7.
92. H.C. Casey, Jr. and M.B. Panish, *ibid.*
93. W. Potz, W. Porod, and D.K. Ferry, *Phys. Rev. B* **32** (6), 3868 (1985).

## **9 Appendices**

## 9.1 Appendix A

### The Dielectric Constant

The optical properties of a semiconductor are contained in the complex dielectric constant

$$\epsilon(\omega) = \epsilon'(\omega) + i\epsilon''(\omega) . \quad (9.1)$$

Absorption and reflection properties can be found by relating  $\epsilon(\omega)$  to the complex index of refraction by

$$\frac{\epsilon(\omega)}{\epsilon_0} = n_c^2(\omega) = (n(\omega) + i\kappa(\omega))^2 , \quad (9.2)$$

where  $n(\omega)$  is the real index and  $\kappa(\omega)$  is the extinction coefficient. The absorption coefficient  $\alpha(\omega)$  is related to the extinction coefficient by

$$\alpha(\omega) = \frac{2\kappa(\omega)}{c} \omega \quad (9.3)$$

where  $c$  is the speed of light. Using  $\epsilon''/\epsilon_0 = 2n\kappa$ ,  $\alpha(\omega)$  is related to the imaginary part of  $\epsilon(\omega)$  by

$$\alpha(\omega) = \frac{\omega}{\epsilon_0 c n(\omega)} \epsilon''(\omega) . \quad (9.4)$$

Finally, the reflectivity at normal incidence is given by

$$R(\omega) = \frac{(n(\omega) - 1)^2 + (\kappa(\omega))^2}{(n(\omega) + 1)^2 + (\kappa(\omega))^2} . \quad (9.5)$$

The usual method of experimentally determining the optical constants is to measure the absorption spectrum (and hence the extinction coefficient,  $\kappa(\omega)$ ) or the reflectivity (which gives  $n(\omega)$  for small  $\kappa(\omega)$ ) for a wide frequency range, and then use the Kramers-Kronig relations to transform the information back to the index of

refraction or extinction coefficient, respectively. Similarly, if the imaginary part of the dielectric constant is calculated, the real part can be found via the Kramers-Kronig relations, and vice versa. The transformations are given by

$$\epsilon'(\omega) = \epsilon_0 \cdot \frac{2}{\pi} \int_0^\infty \frac{\omega' \epsilon''(\omega') d\omega'}{\omega'^2 - \omega^2} \quad (9.6)$$

$$\epsilon''(\omega) = -\frac{2\omega}{\pi} \int_0^\infty \frac{[\epsilon'(\omega') - \epsilon_0] d\omega'}{\omega'^2 - \omega^2} .$$

### 9.1.1 The Oscillator Model

More fundamental than the dielectric constant is the polarizability, which is described by the atomic dipole,  $P$ . The classical equation of motion for an electron oscillating against a fixed nucleus is

$$m_e \ddot{x} + 2\gamma m_e \dot{x} + Kx = -eE \cos \omega t \quad (9.7)$$

where  $m_e$  is the mass of an electron oscillating against the nucleus,  $x$  is the displacement,  $\gamma$  is a frictional coefficient due to dissipative forces such as phonons,  $K$  is the spring constant,  $e$  is the electronic charge, and  $E \cos \omega t$  is the electric field from the photons. The solution to the displacement is

$$x = -\frac{eE/m_e}{(\omega_0^2 - \omega^2) - 2i\omega\gamma} \quad (9.8)$$

where  $\omega_0 = \sqrt{K/m_e}$  is the resonant frequency of the oscillator. The polarization is

then

$$P = -ex = -\frac{e^2/m_e}{(\omega_0^2 - \omega^2) - 2i\omega\gamma} E . \quad (9.9)$$

The macroscopic polarization  $\bar{P}$  is the sum of the atomic dipoles per unit volume, so for the single oscillator, the dielectric constant is

$$\begin{aligned}
\epsilon(\omega) &= \epsilon_0 + \frac{\bar{P}}{\bar{\epsilon}} \\
&= \epsilon_0 + \frac{e^2}{m_0 V} \frac{1}{\omega_0^2 - \omega^2 - 2i\omega\gamma} \\
&= \epsilon_0 + \frac{e^2}{m_0 V} \frac{\omega_0^2 - \omega^2}{(\omega_0^2 - \omega^2)^2 + 4\gamma^2\omega^2} + i \frac{e^2}{m_0 V} \frac{2\gamma\omega}{(\omega_0^2 - \omega^2)^2 + 4\gamma^2\omega^2} \\
&= \epsilon'(\omega) + i\epsilon''(\omega) . \tag{9.10}
\end{aligned}$$

For  $\omega \gg \gamma$ , the imaginary part,  $\epsilon''(\omega)$ , is non-zero only for  $\omega$  near  $\omega_0$ . In that case, it can be approximated by a Lorentzian curve with full-width-half-max of  $2\gamma$ ,

$$\epsilon''(\omega) \approx \frac{e^2}{2m_0\omega_0 V} \frac{\gamma}{(\omega_0 - \omega)^2 + \gamma^2} \tag{9.11}$$

If  $\gamma$  approaches zero,  $\epsilon''(\omega)$  can be approximated by a delta function

$$\begin{aligned}
\epsilon''(\omega) &\approx \frac{e^2 \pi}{2m_0\omega_0 V} \delta(\omega_0 - \omega) \\
&= \frac{e^2 \pi \hbar}{2m_0\omega_0 V} \delta(\hbar\omega_0 - \hbar\omega) . \tag{9.12}
\end{aligned}$$

Note that the Kramers-Kronig transformation of Equation (9.12) gives the real part of Equation (9.10) with  $\gamma = 0$ . This transformation is unnecessary in this case, however, since all the parameters used to calculate  $\epsilon''(\omega)$  can be used to calculate  $\epsilon'(\omega)$  directly.

### 9.1.2 Quantum Mechanical Model

The result above is only for a single classical oscillator, and has been simplified by removing friction losses, which is analogous to the conservation of energy. In a semiconductor, however, many oscillators with various frequencies, damping coefficients and strengths are present, and the classical case breaks down. In order to properly determine the dielectric constant, a quantum mechanical description is needed.

The derivation begins with the calculation of the absorption coefficient, which is then related to  $\epsilon''(\omega)$  by Equation (9.4). This begins with the absorption and emission rates  $W_{nm\beta\lambda}^a$  and  $W_{mn\beta\lambda}^e$ , respectively, which are

$$W_{nm\beta\lambda}^a = \frac{\pi e^2}{m_e^2 \omega \epsilon V} |P_{nm\lambda}|^2 n_{\lambda\beta} \delta[\vec{k}_n - \vec{k}_m] \delta[E_n - E_m - \hbar\omega_\beta]$$

$$W_{mn\beta\lambda}^e = \frac{\pi e^2}{m_e^2 \omega \epsilon V} |P_{mn\lambda}|^2 (n_{\lambda\beta} + 1) \delta[\vec{k}_n - \vec{k}_m] \delta[E_n - E_m - \hbar\omega_\beta] \quad (9.13)$$

The subscripts denote the following:  $m$  is the upper conduction band,  $n$  is the lower valence band,  $\beta$  is the photon wavevector,  $\lambda$  is one of two possible polarizations, and  $\vec{k}$  is the electronic wavevector which defines the particular state in the band  $m$  or  $n$ .

The factor  $n_{\lambda\beta}$  is the photon occupation number given by the Bose-Einstein distribution function. The absorption rate and the first term in the emission rate are the stimulated terms which depend on the number of photons  $n_{\lambda\beta}$ , while the other emission term is independent of the  $n_{\lambda\beta}$ , and hence is the spontaneous emission term. The first delta function maintains the conservation of momentum, assuming negligible photon momentum, and the second delta function is the conservation of energy from Fermi's Golden Rule. Finally,  $P_{nm\lambda}$  is the momentum matrix element, which is assumed to be independent of  $k$ , given by

$$P_{nm\lambda} = -i\hbar \int u_n^*(\vec{r}) \hat{a}_\lambda \cdot \vec{\nabla}_r u_m(\vec{r}) d^3r \quad (9.14)$$

In Equation (9.14) the dipole approximation is assumed, and  $\hat{a}_\lambda$  is the unit vector in the direction of the electric field of the  $\lambda$ -polarized photons. The functions  $u(\vec{r})$  are the periodic parts of the wavefunctions, which are usually taken near the zone center with a small range of  $k$ .

The momentum matrix elements have been worked out<sup>[67]</sup> for two conduction band states (spin-up and spin-down) and six valence band states (hh, lh, so; up and down) including spin-orbit interaction. The values are given in Table 9.1.

**Table 9.1. Momentum Matrix Elements between Conduction- and Valence-Band States**

|     | C1   | C2  |
|-----|--|---|
| hh1 | $\frac{P_o}{\sqrt{2}}(\lambda_x + i\lambda_y)$   | 0   |
| hh2 | 0  | $i\frac{P_o}{\sqrt{2}}(\lambda_x - i\lambda_y)$ |
| lh1 | $-iP_o\sqrt{\frac{2}{3}}\lambda_z$               | $i\frac{P_o}{\sqrt{6}}(\lambda_x + i\lambda_y)$ |
| lh2 | $\frac{P_o}{\sqrt{6}}(\lambda_x - i\lambda_y)$   | $P_o\sqrt{\frac{2}{3}}\lambda_z$                |
| so1 | $\frac{P_o}{\sqrt{3}}\lambda_z$                  | $\frac{P_o}{\sqrt{3}}(\lambda_x + i\lambda_y)$  |
| so2 | $-i\frac{P_o}{\sqrt{3}}(\lambda_x - i\lambda_y)$ | $i\frac{P_o}{\sqrt{3}}\lambda_z$                |

The conduction band dispersion relation was worked out by Kane as

$$E_c = E_g + \frac{\hbar^2 k^2}{2m_o} + \left( \frac{P_o \hbar}{m_o} \right)^2 \frac{k^2}{3} \left( \frac{2}{E_g} + \frac{1}{E_g + \Delta} \right) \quad (9.15)$$

$$= E_g + \frac{\hbar^2 k^2}{2m_e^*}$$

where  $\Delta$  is the split-off energy between the light-hole- and split-off-band maximas.  $P_o$  can then be solved for to find its dependence on the known conduction band effective mass, and is given by

$$P_o^2 = \frac{m_o E_o}{2} \left( \frac{m_o}{m_e} - 1 \right) \frac{3E_o + 3\Delta}{3E_o + 2\Delta} . \quad (9.16)$$

The rate of change in the number of photons is given by the summation over pairs of states of the emission minus the absorption rates, each multiplied by the their respective probabilities governed by Fermi-Dirac statistics. The rate is given by

$$\frac{d}{dt} n_{\lambda\beta} = \sum_{m, n, \vec{k}} W_{mn\beta\lambda}^e f_n (1 - f_m) - W_{nm\beta\lambda}^a f_m (1 - f_n) \quad (9.17)$$

where  $f_n$ ,  $f_m$  are the Fermi-Dirac distribution functions of the upper and lower states, respectively. Expanding,

$$\begin{aligned} \frac{d}{dt} n_{\lambda\beta} &= -n_{\lambda\beta} \sum_{m, n} \frac{\pi e^2}{m_o^2 \omega \epsilon V} |P_{nm\lambda}|^2 \sum_{\vec{k}} \delta[\vec{k}_n - \vec{k}_m] \delta[E_n - E_m - \hbar\omega] (f_m - f_n) \\ &\quad + \sum_{m, n} \frac{\pi e^2}{m_o^2 \omega \epsilon V} |P_{nm\lambda}|^2 \sum_{\vec{k}} \delta[\vec{k}_n - \vec{k}_m] \delta[E_n - E_m - \hbar\omega] f_n (1 - f_m) \\ &= -n_{\lambda\beta} \frac{1}{\tau_{\lambda\beta}} + l_{\lambda\beta} \end{aligned} \quad (9.18)$$

where the first term in the change in  $n_{\lambda\beta}$  is due to stimulated emission and absorption, and the second term is due to spontaneous emission. The absorption coefficient is given by

$$\alpha_{\lambda\beta} = \frac{1}{\tau_{\lambda\beta} c n(\omega)} \quad (9.19)$$

which is related to the imaginary part of the dielectric constant via Equation (4). Solving for  $\epsilon''(\omega)$  gives

$$\begin{aligned}
\epsilon''(\omega) &= \frac{\epsilon_0}{\tau_{\lambda\beta}\omega} \\
&= \frac{\pi q^2}{m_0^2\omega^2 V} \sum_n \sum_m |P_{nm\lambda}|^2 \sum_{\vec{k}} \delta[\vec{k}_n - \vec{k}_m] \delta[E_n - E_m - \hbar\omega] (f_m - f_n)
\end{aligned} \tag{9.20}$$

### 9.1.3 Oscillator Strength and Lineshape Broadening

To link Equation (9.20) to the oscillator model of Equation (9.12), examine the response between two bands  $n$  and  $m$  at wavevector  $\vec{k}$ . Let  $E_n - E_m = \hbar\omega_0$ ,  $f_m = 1$ ,  $f_n = 0$ , and consider only one polarization. Equation (9.20) then becomes

$$\begin{aligned}
\epsilon''(\omega) &= \frac{\pi e^2}{m_0^2\omega^2 V} |P_{nm\lambda}|^2 \delta[\hbar\omega_0 - \hbar\omega] \\
&= \frac{\pi \hbar e^2}{2m_0\omega V} \frac{2|P_{nm\lambda}|^2}{m_0\hbar\omega} \delta[\hbar\omega_0 - \hbar\omega] \\
&= \frac{\pi \hbar e^2}{2m_0\omega V} f_{nm\lambda} \delta[\hbar\omega_0 - \hbar\omega] .
\end{aligned} \tag{9.21}$$

The factor  $f_{nm\lambda}$  is called the oscillator strength which describes the relative strength of the oscillator between band  $m$  and band  $n$  for the polarization  $\lambda$  compared to the other oscillators in the entire system. The oscillator strength obeys the sum rule<sup>[85]</sup>

$$\sum_{n,m} f_{nm\lambda} = 1 . \tag{9.22}$$

If the oscillator in Equation (9.21) is allowed to be damped as in Equation (9.11), the delta function can be replaced by a Lorentzian lineshape,

$$\begin{aligned}
\pi \hbar \delta(\hbar\omega_0 - \hbar\omega) &= \pi \delta(\omega_0 - \omega) \\
&\approx \frac{\gamma}{(\omega_0 - \omega)^2 + \gamma^2} ,
\end{aligned} \tag{9.23}$$

so Equation (9.21) becomes

$$\epsilon''(\omega) = \frac{e^2 f_{nm\lambda}}{2m_0\omega V} \frac{\gamma_{nm\lambda}}{(\omega_0 - \omega)^2 + \gamma_{nm\lambda}^2} . \tag{9.24}$$

Re-introducing the sum over discrete states,

$$\epsilon''(\omega) = \frac{e^2}{2m_e \omega V} \sum_n \sum_m \sum_{\vec{k}} \frac{f_{nm\lambda} \gamma_{nm\lambda}}{(\omega_0 - \omega)^2 + \gamma_{nm\lambda}^2} \delta[\vec{k}_n - \vec{k}_m] \quad (9.25)$$

In a real system, the lifetimes of the states are finite, so the energy (and hence the frequency) is broadened due to the uncertainty principle<sup>[86]</sup>  $\hbar \Delta \omega \tau \approx \hbar$ , or

$$2\gamma_{nm\lambda} = \Delta\omega \approx \frac{1}{\tau} = \frac{1}{\tau_m} + \frac{1}{\tau_n} \quad . \quad (9.26)$$

This lifetime-broadening is referred to as natural broadening if  $\tau$  is radiative only. The effects of collision broadening have been neglected in Equation (9.26), although they might be important (even dominant) since the interaction time of the collision can be several orders of magnitude lower than the mean radiative lifetimes. Fortunately,  $\gamma$  can be determined experimentally from absorption or time-resolved spectroscopy data.

Equation (9.25) is particularly useful for discrete features such as excitons, while Equation (9.20) can be used to describe systems with a continuous density of states. Broadening mechanisms can be included in the later case, however, by convolving it with the broadened lineshape.<sup>[87]</sup>

#### 9.1.4 Dielectric Constant

The dielectric constant can be calculated for a bulk semiconductor using Equation (9.20). For each band, with  $f_m = 1$ ,  $f_n = 0$ ,

$$\begin{aligned}
\epsilon''(\omega) &= \frac{\pi e^2}{m_e^2 \omega^2} |P_{nm\lambda}|^2 \frac{1}{V} \sum_{\vec{k}} \delta[E_n(\vec{k}) - E_m(\vec{k}) - \hbar\omega] (f_m - f_n) \\
&= \frac{\pi e^2}{m_e^2 \omega^2} |P_{nm\lambda}|^2 \frac{1}{V} \frac{V}{8\pi^3} \int 4\pi k^2 \delta \left[ E_g + \frac{\hbar^2 k^2}{2\mu} - \hbar\omega \right] dk \\
&= \frac{\pi e^2}{m_e^2 \omega^2} |P_{nm\lambda}|^2 \int \frac{2\mu(\hbar\omega - E_g)}{\hbar^2} \delta \left[ E_g + \frac{\hbar^2 k^2}{2\mu} - \hbar\omega \right] \frac{\sqrt{2\mu}}{2\hbar\sqrt{\hbar\omega - E_g}} dE \\
&= \frac{\pi e^2}{m_e^2 \omega^2} |P_{nm\lambda}|^2 \frac{\sqrt{2\mu}^{3/2}}{2\pi^2 \hbar^3} \sqrt{\hbar\omega - E_g} \\
&= \frac{\pi e^2}{m_e^2 \omega^2} |P_{nm\lambda}|^2 \rho_3(\hbar\omega - E_g) . \tag{9.27}
\end{aligned}$$

The conservation of momentum is contained in the explicit value of  $\vec{k}$  for  $E_n$  and  $E_m$  in the conservation of energy delta function. The reduced 3-dimensional (3D) density of states,  $\rho_3$ , contains the reduced mass for bands m and n,

$$\frac{1}{\mu} = \frac{1}{m_m} + \frac{1}{m_n} , \tag{9.28}$$

and only one spin is considered for each band pair.

To get the real part of the dielectric constant, the Kramers-Kronig transformation can be used, as long as the complex part is known over a sufficiently large frequency spectrum. If the spectrum of interest covers a small region, but is sufficiently separated from other features in the spectrum which contribute to the local real dielectric constant, the transformation can still be used with proper precautions.<sup>[88]</sup> In this case, the significant contributions from other parts of the spectrum must be included in the background dielectric constant,  $\epsilon_b(\omega)$ , which is real and replaces  $\epsilon_0$  in Equation (9.6).

If only a small spectral region is known, as in the case of a band edge where only the parabolic part near  $\vec{k} = 0$  is assumed, the Kramers-Kronig analysis will have large errors. To get around this problem, the real part of Equation (9.10) can be used with  $\epsilon_0 = \epsilon_b(\omega)$  and the real oscillator term multiplied by the oscillator strength, or

$$\epsilon'(\omega) = \epsilon_b(\omega) + \frac{e^2}{m_0 V} |P_{nm\lambda}(\omega)|^2 \frac{\omega_0^2 - \omega^2}{(\omega_0^2 - \omega^2)^2 + 4\gamma^2\omega^2} \quad (9.29)$$

For the quantum well dielectric constant, we start with the second step of Equation (9.27), and substitute  $\vec{k} dk = (\mu/\hbar^2) dE$ , and proceed as follows with the assumption  $k_{||} = 0$ , and  $k = k_z$  which is quantized in the  $\hat{z}$  direction.

$$\begin{aligned} \epsilon''(\omega) &= \frac{\pi e^2}{m_0^2 \omega^2} |P_{nm\lambda}|^2 \frac{1}{2\pi^2} \int \vec{k} \delta \left[ E_g + \frac{\hbar^2 k^2}{2\mu} - \hbar\omega \right] \frac{\mu}{\hbar^2} dE \\ &= \frac{\pi e^2}{m_0^2 \omega^2} |P_{nm\lambda}|^2 \frac{\mu}{2\pi^2 \hbar^2} \int (k_{||} + k_z) \delta \left[ E_g + \frac{\hbar^2 k_{||}^2}{2\mu} + \frac{l^2 \pi^2 \hbar^2}{2\mu L_z} - \hbar\omega \right] dE \\ &= \frac{\pi e^2}{m_0^2 \omega^2} |P_{nm\lambda}|^2 \frac{\mu}{2\pi^2 \hbar^2} \int k_z \delta [E_g + E_l - \hbar\omega] dE \\ &= \frac{e^2 \mu}{2\pi m_0^2 \hbar^2 \omega^2} |P_{nm\lambda}|^2 k_z \Theta[\hbar\omega - (E_g + E_l)] \\ &= \frac{\pi e^2}{m_0^2 \omega^2} |P_{nm\lambda}|^2 \frac{\mu}{2\pi^2 \hbar^2} k_z \Theta_l \\ &= \frac{\pi e^2}{m_0^2 \omega^2} |P_{nm\lambda}|^2 \rho_{\text{red}}^{\text{QW}} \end{aligned} \quad (9.30)$$

where  $\Theta_l$  is a step function for each quantized level,  $E_l$ , and  $\rho_{\text{red}}^{\text{QW}}$  is the reduced density of states for a finite quantum well with only one spin considered (see Appendix C). In fact, the reduced density of states in Equation (9.30) is valid for all systems as long as the proper form of  $k_z$  is used.<sup>[89]</sup>

## 9.2 Appendix B

### Optical Matrix Elements in Quantum Wells

Under the envelope-function approximation, the wavefunction of an electron in the conduction band of a quantum well can be expressed as<sup>[90]</sup>

$$\Psi_{n_i \vec{k}} = \Phi_{n_i}(z) u_n(\vec{r}) e^{i(\vec{k}_x + \vec{k}_y) \cdot (\vec{r}_x + \vec{r}_y)} \quad (9.31)$$

where  $\hat{z}$  is the direction of quantization,  $n$  denotes the band with subscript  $i$  indexing the bound state,  $\Phi(z)$  is the envelope wavefunction and  $u(\vec{r})$  is the periodic Bloch function of the bulk material. The momentum matrix element between the conduction band (n) and valence band (m) with a photon field polarized in the direction  $\hat{a}_\lambda$  is

$$\begin{aligned} P_{nm\lambda}^{QW} &= -i\hbar \int \Psi_{n_i \vec{k} \text{vec}}^* \hat{a}_\lambda \cdot \vec{\nabla}_r \Psi_{m_i \vec{k}} d^3 r \\ &\approx \int \Phi_{n_i}^*(z) \Phi_{m_i}(z) dz \left[ -i\hbar \int u_n(\vec{r}) \hat{a}_\lambda \cdot \vec{\nabla}_r u_m(\vec{r}) d^3 r \right] \delta(\vec{k}_{n||} - \vec{k}_{m||}) \\ &= \langle n_i | m_i \rangle P_{\lambda mn} \delta(\vec{k}_{n||} - \vec{k}_{m||}) \quad . \end{aligned} \quad (9.32)$$

The first term,  $\langle n_i | m_i \rangle$  is the overlap of the envelope wavefunctions which was assumed to be  $\delta_{mn}$  by Asada *et al.* However,  $\langle c_1 | h h_1 \rangle \approx 0.8$  for a one-monolayer GaAs/Al<sub>0.3</sub>Ga<sub>0.7</sub>As quantum well, so the approximation by Asada *et al.* is no longer valid for ultra-thin wells.  $P_{\lambda mn}$  is related to the bulk matrix element except for its average with respect to the direction of  $\vec{k}$ , and the delta function is the momentum conservation term.

Using the  $\vec{k} \cdot \vec{p}$  method, Kane calculated the wavefunctions  $u(r)$ . If  $\vec{k} = k \hat{z}$ , the normalized wavefunctions can be written in spinor rotation as<sup>[91]</sup>

$$\begin{aligned}
u_{c\uparrow}(\vec{r}) &= \begin{pmatrix} \alpha_{c\uparrow} \\ \beta_{c\uparrow} \end{pmatrix} = \begin{pmatrix} |S\rangle \\ 0 \end{pmatrix} , \\
u_{h\uparrow}(\vec{r}) &= \begin{pmatrix} \frac{1}{\sqrt{2}}|X\rangle + i\frac{1}{\sqrt{2}}|Y\rangle \\ 0 \end{pmatrix} , \\
u_{h\downarrow}(\vec{r}) &= \begin{pmatrix} -i\sqrt{\frac{2}{3}}|Z\rangle \\ i\frac{1}{\sqrt{6}}|X\rangle - \frac{1}{\sqrt{6}}|Y\rangle \end{pmatrix} , \\
u_{s\uparrow}(\vec{r}) &= \begin{pmatrix} \frac{1}{\sqrt{3}}|Z\rangle \\ \frac{1}{\sqrt{3}}|X\rangle + i\frac{1}{\sqrt{3}}|Y\rangle \end{pmatrix} , \\
u_{c\downarrow}(\vec{r}) &= \begin{pmatrix} 0 \\ |S\rangle \end{pmatrix} , \\
u_{h\uparrow}(\vec{r}) &= \begin{pmatrix} 0 \\ i\frac{1}{\sqrt{2}}|X\rangle + \frac{1}{\sqrt{2}}|Y\rangle \end{pmatrix} , \\
u_{h\downarrow}(\vec{r}) &= \begin{pmatrix} \frac{1}{\sqrt{6}}|X\rangle - i\frac{1}{\sqrt{6}}|Y\rangle \\ \sqrt{\frac{2}{3}}|Z\rangle \end{pmatrix} , \\
u_{s\downarrow}(\vec{r}) &= \begin{pmatrix} -i\frac{1}{\sqrt{3}}|X\rangle - \frac{1}{\sqrt{3}}|Y\rangle \\ i\frac{1}{\sqrt{3}}|Z\rangle \end{pmatrix} .
\end{aligned} \tag{9.33}$$

The basis function  $|S\rangle$  is a symmetrical s-like wavefunction, while  $|X\rangle$ ,  $|Y\rangle$ , and  $|Z\rangle$  are atomic p-like functions antisymmetric in x, y, and z, respectively. The subscripts  $c, h, l$  and  $s$  are for conduction, heavy-hole, light-hole, and split-off bands, respectively, and  $\uparrow$  and  $\downarrow$  denote spin-up and spin-down functions. Because of the symmetry of the basis functions, the only allowed integrals are

$$-i\hbar \langle S | \frac{\partial}{\partial x} | X \rangle = -i\hbar \langle S | \frac{\partial}{\partial x} | Y \rangle = -i\hbar \langle S | \frac{\partial}{\partial x} | Y \rangle = P_0 . \tag{9.34}$$

Finally, the matrix elements between the Bloch wavefunctions are

$$P_{nm} = -i\hbar \langle \alpha_n | \vec{\nabla} | \alpha_m \rangle - i\hbar \langle \beta_n | \vec{\nabla} | \beta_m \rangle . \tag{9.35}$$

If  $\vec{k} \neq \vec{k}'$ , then the basis functions are denoted by a prime ( $|X'\rangle$ ) and are transformed to the original functions (see Figure 9.1) using<sup>[67]</sup>

$$\begin{pmatrix} X' \\ Y' \\ Z' \end{pmatrix} = \begin{pmatrix} \cos\theta\cos\phi & \cos\theta\sin\phi & -\sin\theta \\ -\sin\phi & \cos\phi & 0 \\ \sin\theta\cos\phi & \sin\theta\sin\phi & \cos\theta \end{pmatrix} \begin{pmatrix} X \\ Y \\ Z \end{pmatrix} , \\
S' = S . \tag{9.36}$$

The matrix element is a measure of the dipole moment between the hole in band m and the electron in band n, which forms a vector,  $\vec{P}$ , perpendicular to  $\vec{k}$ . The interaction of

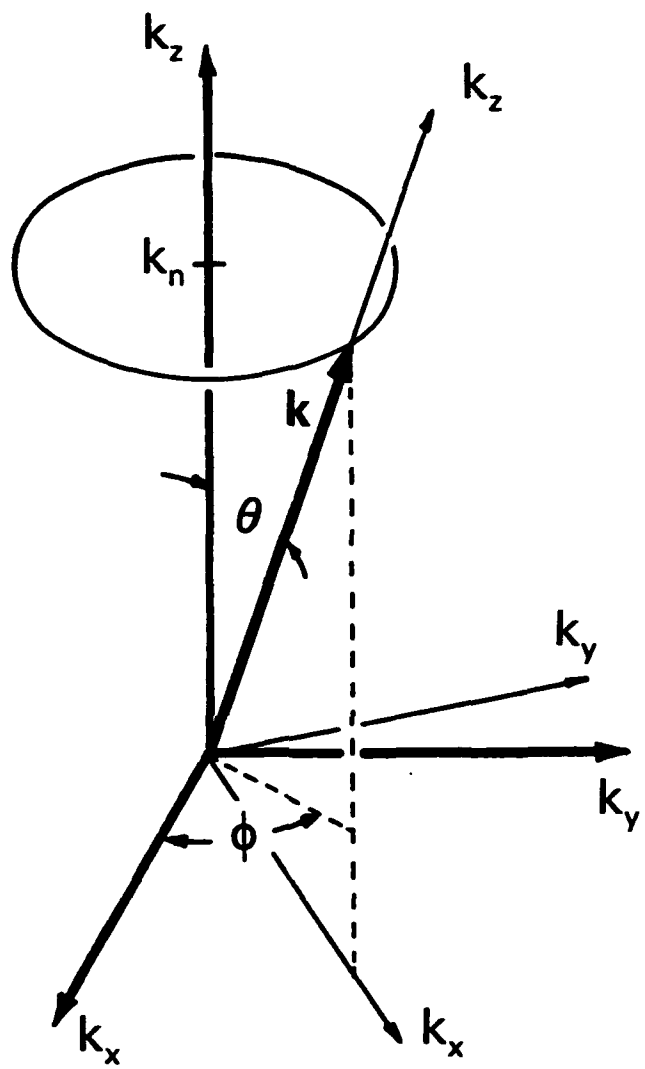


**Figure 9.1** Coordinate system for the transformation of basis functions. In a quantum well,  $k_z$  is taken as the quantized direction, and  $k_z$  is fixed at  $k_n$  for each energy level  $E_n$ . For transitions in the  $n^{\text{th}}$  level with  $|\vec{k}| > k_n$ , the angle  $\theta$  is fixed also.

the dipole with the electric field is described by  $|\vec{P} \cdot \hat{a}_x|^2$ , which is averaged over all directions of  $\vec{k}$  in bulk. In the case of  $\vec{E} = E \hat{x}$ , the matrix element for the conduction-heavy hole band transition is derived from the  $\hat{x}$  component of  $\vec{P}_{c\downarrow h\downarrow}$ ,

$$\begin{aligned}
 \vec{P}_{c\downarrow h\downarrow} &= -i\hbar \frac{1}{\sqrt{2}} \langle S' | \nabla | X' \rangle + i \langle S' | \nabla | Y' \rangle \\
 &= -i\hbar \frac{1}{\sqrt{2}} (\cos\theta \cos\phi \langle S | \nabla | X \rangle + \cos\theta \sin\phi \langle S | \nabla | Y \rangle \\
 &\quad - \sin\theta \langle S | \nabla | Z \rangle - i \sin\phi \langle S | \nabla | X \rangle + i \cos\phi \langle S | \nabla | Y \rangle) \\
 &= \frac{P_o}{\sqrt{2}} [(\cos\theta \cos\phi - i \sin\phi) \hat{x} + (\cos\theta \sin\phi + i \cos\phi) \hat{y} - (\sin\theta) \hat{z}] . \quad (9.37)
 \end{aligned}$$

or

$$\hat{a}_x \cdot \vec{P}_{c\downarrow h\downarrow} = \frac{P_o}{\sqrt{2}} (\cos\theta \cos\phi - i \sin\phi) \quad (9.38)$$

The average matrix element for the bulk is then

$$\begin{aligned}
 \langle P_{c\downarrow h\downarrow}^2 \rangle &= \frac{\int_0^{2\pi} \int_0^\pi |\hat{a}_x \cdot \vec{P}_{c\downarrow h\downarrow}|^2 \sin\theta d\theta d\phi}{\int_0^{2\pi} \int_0^\pi \sin\theta d\theta d\phi} \\
 &= \frac{P_o^2}{2} \frac{1}{4\pi} \int_0^{2\pi} \int_0^\pi (\cos^2\theta \cos^2\phi + \sin^2\phi) \sin\theta d\theta d\phi \\
 &= \frac{P_o^2}{2} \frac{1}{4\pi} \frac{8\pi}{3} = \frac{2P_o^2}{3} . \quad (9.39)
 \end{aligned}$$

Similarly, the matrix elements for the other bands can be calculated, and are given in Table 9.2.

In a quantum well, however,  $k_z$  is fixed for each state, so for a particular magnitude  $|\vec{k}|$ ,  $\theta$  will also be fixed. The average matrix element is then, for TE-polarized photons ( $\hat{a}_x \cdot \hat{z} = 0$ ),

$$\begin{aligned}
\langle P_{c\downarrow h\downarrow}^2 \rangle_{TE}^{QW} &= \frac{\int_0^{2\pi} |\vec{a}_x \cdot \vec{P}_{c\downarrow h\downarrow}| d\phi}{\int_0^{2\pi} d\phi} \\
&= \frac{P_o^2}{2} \frac{1}{2\pi} \int_0^{2\pi} (\cos^2 \theta \cos^2 \phi + \sin^2 \phi) d\phi \\
&= \frac{P_o^2}{2} \frac{1}{2\pi} (\pi \cos^2 \theta + \pi) \\
&= \frac{1}{2} \frac{P_o^2}{2} (1 + \cos^2 \theta)
\end{aligned} \tag{9.40}$$

In general, the effective mass in a superlattice is anisotropic, having a larger mass in the direction of the superlattice due to the modified dispersion relation. If, however, the mass is nearly isotropic, the following approximation can be made using  $k_z = k \cos \theta$ .

$$\frac{E_n}{E} \approx \frac{k_z^2}{k_x^2 + k_y^2 + k_z^2} = \frac{k^2 \cos^2 \theta}{k^2} = \cos^2 \theta \tag{9.41}$$

where  $E_n$  is the bound state energy ( $k_x = k_y = 0$ ), and  $E$  is the total energy for the three-dimensional (3D) system. In this case, Equation (9.39) becomes

$$\langle P_{c\downarrow h\downarrow}^2 \rangle_{TE}^{QW} = \frac{P_o^2}{4} \left( 1 + \frac{E_n}{E} \right) \tag{9.42}$$

The calculations for the other bands are given in Table 9.2. The approximation of Equation (9.40) can be used for  $\cos^2 \theta$ , while  $\sin^2 \theta$  can be replaced by  $(1 - E_n/E)$ .

Table 9.2. Bulk and Quantum-Well average matrix elements  $\langle P^2 \rangle$  for conduction-heavy hole, light hole, and split-off band transitions. Note that matrix elements for  $\uparrow\uparrow$  transitions are the same for  $\downarrow\downarrow$  transitions, and the  $\downarrow\uparrow$  transitions are the same for  $\uparrow\downarrow$ .

|       | $\lambda$ | Bulk                                     |  | Quantum Well                             |  |
|-------|-----------|--|--|--|--|
| Spins |           | $\uparrow\uparrow, \downarrow\downarrow$ | $\uparrow\downarrow, \downarrow\uparrow$ | $\uparrow\uparrow, \downarrow\downarrow$ | $\uparrow\downarrow, \downarrow\uparrow$ |
| c-hh  | TE        | $\frac{1}{3}P_o^2$                       | 0  | $\frac{1}{4}P_o^2(1 + \cos^2\theta)$     | 0  |
|       | TM        | $\frac{1}{3}P_o^2$                       | 0  | $\frac{1}{2}P_o^2 \sin^2\theta$          | 0  |
| c-lh  | TE        | $\frac{2}{9}P_o^2$                       | $\frac{1}{9}P_o^2$                       | $\frac{1}{3}P_o^2 \sin^2\theta$          | $\frac{1}{12}P_o^2(1 + \cos^2\theta)$    |
|       | TM        | $\frac{2}{9}P_o^2$                       | $\frac{1}{9}P_o^2$                       | $\frac{2}{3}P_o^2 \cos^2\theta$          | $\frac{1}{6}P_o^2 \sin^2\theta$          |
| c-so  | TE        | $\frac{1}{9}P_o^2$                       | $\frac{2}{9}P_o^2$                       | $\frac{1}{6}P_o^2 \sin^2\theta$          | $\frac{1}{6}P_o^2(1 + \cos^2\theta)$     |
|       | TM        | $\frac{1}{9}P_o^2$                       | $\frac{2}{9}P_o^2$                       | $\frac{1}{3}P_o^2 \cos^2\theta$          | $\frac{1}{3}P_o^2 \sin^2\theta$          |

Note that if all matrix elements for each transition are added together, including all combinations of spin and polarization, the total would be  $4P_o^2$ . The total includes the familiar spin degeneracy as well as the sum over both polarizations. The polarization selection rules can be obtained from Table 9.2 by comparing the matrix elements for each polarization. For TE, the selection rules give

$$\langle P_{ch}^2 \rangle_{TE}^{QW} : \langle P_{cl}^2 \rangle_{TE}^{QW} : \langle P_{cs}^2 \rangle_{TE}^{QW} = 3:1:2 \quad , \quad (9.43)$$

and for transverse magnetic (TM),

$$\langle P_{ch}^2 \rangle_{TM}^{QW} : \langle P_{cl}^2 \rangle_{TM}^{QW} : \langle P_{cs}^2 \rangle_{TM}^{QW} = 0:2:1 \quad . \quad (9.44)$$

In the conduction to heavy-hole transition, only transitions between states with the same spin are allowed, thus conserving angular momentum. The result of this spin selection rule is that an additional factor of  $\frac{1}{2}$  must be multiplied to  $\langle P_{ch}^2 \rangle$ ,<sup>[92]</sup> since the probability of the two states involved having the same spin is  $\frac{1}{2}$ .

Due to the relativistic motion of electrons near the atomic nuclei, an effective magnetic field is present, which gives rise to spin-orbit interaction. The result is the lifting of the degeneracy of the valence bands so that the light-hole and split-off-hole bands are separated from the heavy-hole band.<sup>[91]</sup> Hence, the spin selection rule is relaxed for these two bands, and transitions are possible between states with opposite spins.

To complete this discussion of the matrix element, we must determine  $P_o^2$ . In the Kane model, the conduction band dispersion is given by

$$\begin{aligned} E_c &= E_g + \frac{\hbar^2 k^2}{2m_o} + \frac{\hbar^2 k^2 P_o^2}{3m_o} \left( \frac{2}{E_g} + \frac{1}{E_g + \Delta} \right) \\ &= E_g + \frac{\hbar^2 k^2}{2m_c^*} , \end{aligned} \quad (9.45)$$

which is the origin of the effective mass,  $m^*$ . In Equation (9.44),  $E_g$  is the bandgap at  $k = 0$ ,  $\Delta$  is the spin-orbit splitting of the valence band, and  $m_o$  is the free-electron mass.  $P_o^2$  is then related to the effective mass in the conduction band by

$$P_o^2 = \frac{m_o E_g}{2} \left( \frac{m_o}{m_c^*} - 1 \right) \frac{E_g + \Delta}{E_g + \frac{2}{3}\Delta} . \quad (9.46)$$

In  $\text{Al}_x\text{Ga}_{1-x}\text{As}$ , the values of  $E_g$ ,  $m_c^*$ ,<sup>[62]</sup> and  $\Delta$ <sup>[93]</sup> are

$$E_g = 1.519 + 1.247x - \frac{5.405 \times 10^{-4} T^2}{T + 204} ; x \leq 0.45 \quad (9.47)$$

$$= 1.519 + 1.247x + 1.147(x - 0.45)^2 - \frac{5.405 \times 10^{-4} T^2}{T + 204} ; x > 0.45 \quad (9.48)$$

$$\Delta = 0.341 - 0.066x \quad (9.49)$$

$$\frac{m_c^*}{m_e} = 0.0665 + 0.0835x$$

where  $E_g$  is for the  $\Gamma$  band, and both  $E_g$  and  $\Delta$  are given in eV. Using these numbers and finding  $P_o^2$  for  $x = 0$  and 0.3, for example, we get

$$P_o^2(x = 0) = 7.48 E_g m_e \\ = 10.28 \times 10^{-30}$$

$$P_o^2(x = 0.3) = 5.22 E_g m_e \\ = 8.94 \times 10^{-30}$$

with units of eV-kg. The matrix element for the GaAs in this case is 1.15 times that of the alloy.

For a quantum well, the envelope wavefunction generally extends into the barrier, especially in very thin wells where most of the wavefunction is outside the well. For such a structure, neither the envelope-wavefunction overlap, nor the matrix elements for the Bloch wavefunctions in the barriers is negligible. To include these effects, the matrix element given in Equation (9.31) must be found for each region (the well and both barriers), then each part must be added to yield the total matrix element for the entire structure. The matrix element is then

$$\begin{aligned}
P_{\lambda ch}^{QW} &= P_{\lambda ch}^I + P_{\lambda ch}^{II} + P_{\lambda ch}^{III} \\
&= \langle P_{\lambda ch}^2 \rangle^I \int_{-\infty}^{-\frac{L_z}{2}} \Phi_{cl}^* \Phi_{hl} dz + \langle P_{\lambda ch}^2 \rangle^{II} \int_{-\frac{L_z}{2}}^{\frac{L_z}{2}} \Phi_{cl}^* \Phi_{hl} dz \\
&\quad + \langle P_{\lambda ch}^2 \rangle^{III} \int_{\frac{L_z}{2}}^{\infty} \Phi_{cl}^* \Phi_{hl} dz
\end{aligned} \tag{9.50}$$

where (including the spin selection rule), assuming  $\lambda = \hat{\alpha}_x$  (TE polarization) and

$$k_x = k_y = 0,$$

$$\langle P_{\lambda ch}^2 \rangle^I = \frac{1}{4} P_{o1}^2$$

and  $P_{o1}^2$  is given by Equation (9.46) using the appropriate parameters from that region.

### **9.3 Appendix C**

#### **The Density of States for Quantum Wells and Superlattices**

M.W. Prairie and R.M. Kolbas, "A General Derivation of the Density of States Function for Quantum Wells and Superlattices," *Superlattices and Microstructures*, Vol. 7, No. 4, pp. 269-277, (1990).

## A GENERAL DERIVATION OF THE DENSITY OF STATES FUNCTION FOR QUANTUM WELLS AND SUPERLATTICES

M. W. Prairie and R. M. Kolbas

Department of Electrical and Computer Engineering  
North Carolina State University, Raleigh, North Carolina 27695-7911

(Received 2 July 1990)

The intent of this paper is to provide the reader with a detailed summary of the development of the density of states (DOS) functions for two-dimensional systems. Specifically, the DOS is derived for an infinite quantum well, a finite well, and a periodic array of coupled wells (a superlattice). Many authors state that the DOS is "simply ..." without references, yet many who are new to the subject of two-dimensional systems may not see the "simplicity," for instance, of the derivation of the DOS for a superlattice. We also show the relationships between the expressions for each case when the appropriate limits are taken. This comparison shows the consistency that such a general derivation furnishes to each expression.

### Introduction

The distribution of carriers (electrons or holes) per unit energy interval in a semiconductor is determined by the density of states (DOS) and the Fermi-Dirac distribution functions. The DOS function tells us how many electron or hole states are in an interval of energy, while the Fermi-Dirac function tells us the probability of finding a carrier for each of those states. For instance, in the case of a superlattice, the distribution of electronic states, or the DOS, is somewhere between that of a quantum well and the bulk semiconductor, and the absorption and emission line-shapes are greatly affected due to the form of the DOS function.<sup>1</sup> This suggests that an understanding of the distribution of states is crucial in the development of optoelectronic devices employing two-dimensional systems.

In this review, the DOS function is first derived for the simple case of the ideal (infinite), two-dimensional (2D) square well. This pure 2D analysis is found to be inadequate and is improved with the incorporation of the third dimension (the well width). The next section considers the DOS function for thin or shallow wells with the bound states of interest near the top of the well. In this case, the ideal analysis breaks down, and the bound states must be found numerically and inserted into the DOS function. The effects of coupling between an array of finite quantum wells is considered next in the derivation for superlattices. Finally, the equivalence between each case is shown as the appropriate limits are taken. First is an example of the equivalence of the single well DOS to that of the bulk semiconductor as the well width is allowed to go to infinity. Next, a conceptual analysis is used to show that the superlattice DOS reduces to the single quantum well case as the barrier width gets large, and the

three-dimensional (3D) DOS is achieved when the barrier width goes to zero, or the well width goes to infinity.

### The Infinite Potential Well

The density of states (DOS),  $g(E)$ , is defined such that the number of orbital states per unit volume with energy between  $E$  and  $dE$  is<sup>2,3</sup>

$$g_i(E)dE = \sum_{\text{spin}} \sum_{\text{min}} \sum_{\text{other}} \int \frac{d\vec{k}}{(2\pi)^i}$$

where  $i$  is the number of dimensions,  $d\vec{k}$  is the differential volume (3D), area (2D) or length (1D) element for a surface of constant energy, and the summations are taken over spin, degenerate band minima, and any other mechanism resulting in a degeneracy of electronic states. For energy surfaces with a high degree of symmetry (spherical, parabolic, etc.), the differential volume element can be converted to a differential function of energy, and the DOS is obtained by taking the derivative of both sides of the above equation with respect to  $E$ . However, since such symmetry is not always the case, we will use the general expression for the DOS, which is given by<sup>2,3</sup>

$$g_i(E) = \sum_{\text{spin}} \sum_{\text{min}} \sum_{\text{other}} \int \frac{1}{(2\pi)^i} \frac{dS}{|\nabla_k E|} \quad (1)$$

where  $dS$  is the differential surface area of the constant energy surface in 3D, while we use a differential length for the 2D case.

The energy,  $E$ , of an electron near the minima of the conduction band in the free particle approximation is given by

$$E = \frac{\hbar^2 k^2}{2m^*} \quad (2)$$

where  $\hbar$  is Plank's constant divided by  $2\pi$ ,  $k$  is the wavevector of the particle, and  $m^*$  is the effective mass.

For the pure 2D case with only spin degeneracy, spherical energy surface, and  $k^2 = k_x^2 + k_y^2$ , Equation (1) becomes

$$\begin{aligned} g_2(E) &= 2 \int \frac{dS}{(2\pi)^2 |\nabla_k E|} \\ &= \int_0^{2\pi} \frac{2k d\phi}{4\pi^2 |\nabla_k [\hbar^2(k_x^2 + k_y^2)/2m^*]|} \\ &= \frac{2\pi k}{2\pi^2 \hbar^2 k/m^*} \\ &= \frac{m^*}{\pi \hbar^2}. \end{aligned} \quad (3)$$

Equation (3) is the DOS for the pure 2D case where there is no  $\hat{z}$  dimension, and bound states higher than  $n=1$  are neglected. In reality, there is a  $\hat{z}$  dimension, which in fact is responsible for the quantum size effects in a real device. To find the DOS using the more general approach, we must solve the problem in three dimensions. The energy is then

$$\begin{aligned} E &= \frac{\hbar^2}{2m^*} (k_x^2 + k_y^2 + k_z^2) \\ &= \frac{\hbar^2}{2m^*} (k^2 + k_z^2), \end{aligned} \quad (4)$$

where the electron is free in the  $\hat{x}$  and  $\hat{y}$  directions ( $k_x$  and  $k_y$  are continuous), while it is bound in the  $\hat{z}$  direction ( $k_z$  is discrete). With the help of Figure 1, the differential surface area is

$$dS = k d\phi \sqrt{(dk)^2 + (dk_z)^2}. \quad (5)$$

Since the differential change in energy along a constant energy surface is zero,

$$dE = \frac{\hbar^2}{m^*} (k dk + k_z dk_z) = 0,$$

so

$$dk = -\frac{k_z}{k} dk_z. \quad (6)$$

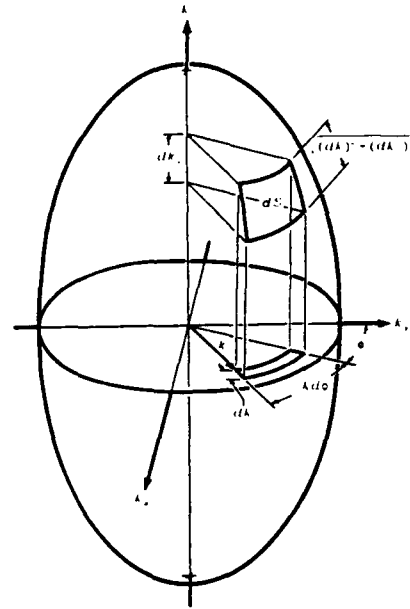


Figure 1. Differential surface area of a constant energy surface in cylindrical coordinates. The x-y cross section is circular, but the x-z (or y-z) cross section is not necessarily circular.

Substituting this expression into  $dS$ , we get

$$\begin{aligned} dS &= k d\phi \sqrt{\left(-\frac{k_z}{k} dk_z\right)^2 + (dk_z)^2} \\ &= \sqrt{k^2 + k_z^2} dk_z d\phi. \end{aligned} \quad (7)$$

The 3D single quantum well (SQW) DOS is then

$$\begin{aligned} g_3^{SQW}(E) &= \int_{-k_z}^{k_z} \int_0^{2\pi} \frac{2\sqrt{k^2 + k_z^2} d\phi dk_z}{8\pi^3 \left| \nabla_k \left[ \frac{\hbar^2}{2m^*} (k^2 + k_z^2) \right] \right|} \\ &= \int_{-k_z}^{k_z} \frac{\sqrt{k^2 + k_z^2} dk_z}{2\pi^2 \frac{\hbar^2}{m^*} \sqrt{k^2 + k_z^2}} \\ &= \frac{m^*}{\pi^2 \hbar^2} k_z. \end{aligned} \quad (8)$$

Recall from the solution of the infinite square well problem that  $k_z$  is quantized, and is given by  $k_z = n\pi/L_z$  where  $L_z$  is the width of the well.<sup>4</sup> Inserting this into Equation (8) gives

$$g_3^{SQW}(E) = \frac{m^*}{\pi \hbar^2 L_z} \frac{n}{L_z}. \quad (9)$$

Comparing this result to Equation (3), we see that

$$g_3^{SQW}(E) = g_2(E) \frac{n}{L_z} \quad n = 1, 2, 3, \dots \quad (10)$$

This same result can also be obtained starting with the 3D DOS. Using Equation (1), the 3D DOS for a bulk semiconductor is given by the well-known expression<sup>5</sup>

$$g_3(E) = \frac{\sqrt{2}(m^*)^{\frac{3}{2}}}{\pi^2 \hbar^3} \sqrt{E}. \quad (11)$$

The solution to the infinite square well (ideal case) results in quantized energies, and for both  $k_x$  and  $k_y$  equal to zero, is given by<sup>6</sup>

$$E_n = \frac{\pi^2 \hbar^2 n^2}{2m^* L_z^2} \quad n = 1, 2, 3, \dots \quad (12)$$

Using this form of the energy in Equation (11), the 3D DOS becomes

$$g_3^{SQW}(E) = \frac{\sqrt{2}(m^*)^{\frac{3}{2}}}{\pi^2 \hbar^3} \frac{\pi \hbar n}{\sqrt{2m^* L_z}} \\ = \frac{m^* n}{\pi \hbar^2 L_z} \quad (13)$$

which is identical to Equations (9) and (10). Equations (10) and (12) are shown graphically in Figure 2 below. Note for each step in  $n$ , a constant  $g_2(E)/L_z$  is added to the 3D DOS function, which results in a set of steps that follow the bulk DOS curve.

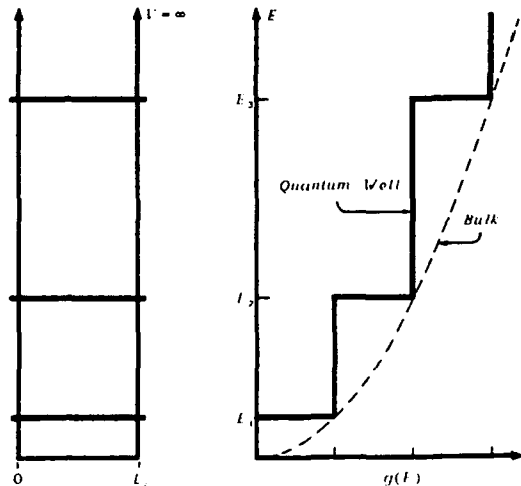


Figure 2. The DOS of an infinite quantum well as it corresponds to the bound-state energies. In this case, the bound-state energy is inversely proportional to the well width, while the DOS is inversely proportional to the square of the width, so a well that is half as thick as the original one will have a bound state twice as high, and a DOS four times the original value.

### The Finite Potential Well

We have seen so far that the DOS of an infinite potential well is a step-like function, where a constant  $g_2(E)/L_z$  is added to  $g_3^{SQW}(E)$  for each quantized step in energy. For the finite well, however, the wavefunctions near the top of the well are less confined, resulting in lower bound state energies compared to those of the infinite well, resulting in different size steps in the DOS. This can be seen by solving Schrödinger's Equation and numerically or graphically finding the values for the bound states.<sup>7</sup>

The finite potential well is shown in Figure 3. Taking the bottom of the well as zero potential and the top of the well as  $V_0$ , we can define the following variables:

$$\alpha^2 = \frac{2m^*(V_0 - E)}{\hbar^2}$$

$$k^2 = \frac{2m^* E}{\hbar^2}$$

$$\gamma^2 = \frac{2m^* V_0}{\hbar^2}.$$

For even wavefunctions, the solution is

$$\alpha = k \tan\left(k \frac{L_z}{2}\right), \quad (14)$$

while the odd solution is

$$\alpha = -k \cot\left(k \frac{L_z}{2}\right). \quad (15)$$

Also, notice that from the defined variables,

$$\gamma^2 = \alpha^2 + k^2. \quad (16)$$

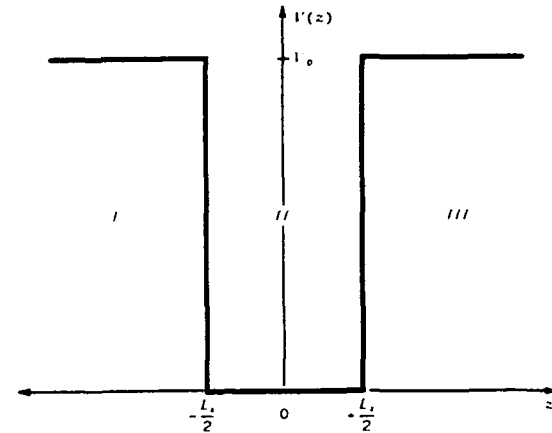


Figure 3. Finite potential well. The width is  $L_z$ , and the potential depth is  $V_0$ .

which is the equation for a circle with radius  $\gamma$ . Graphing equations (14-16) as in Figure 4, we can find the set of allowed values  $k_n$ , which give us the values of the energy eigen states

$$E_n = \frac{\hbar^2}{2m} k_n^2. \quad (17)$$

Using Equation (17) in (11), we find the DOS for the finite quantum well (FQW) to be

$$g_3^{\text{FQW}}(E) = \frac{m^* k_n}{\pi \hbar^2} \frac{1}{\pi}. \quad (18)$$

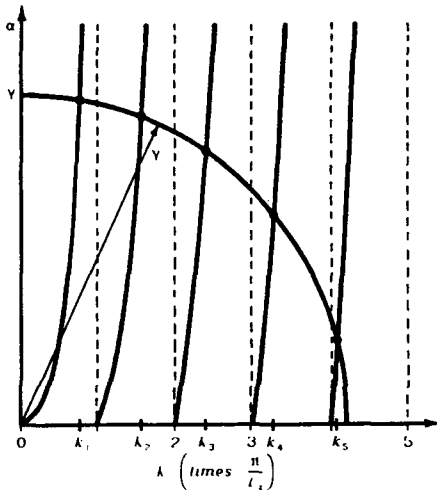


Figure 4. Graphical solution for bound states in a finite potential well. As the well gets thinner, the circular curve of radius  $\gamma$  will contract. In this case (symmetric well), there will always exist at least one bound state.

Notice that  $\Delta k = k_{n+1} - k_n$  is no longer a constant. In fact,  $\Delta k$  gets smaller as  $n$  gets bigger for the same reason that each bound state of the finite well is lower than the corresponding eigen energy of the infinite well by an increasing amount as  $n$  increases as shown in Figure 5.

Notice that the highest bound state of the finite quantum well is very near the top of the well. Referring back to Figure 4, the intersection on the circle for this state occurs at a point where a tangent to the circle will be almost vertical. This means that if the width of the well were changed, the shift in the bound state would be very small. If the well was very thin such that  $\pi/L_z \gg \gamma$ , we would only have one bound state in the well and the energy of that state would be near the top of the well. In this case, a large change in  $L_z$  would only produce a small shift in the energy, as shown in Figure 6.

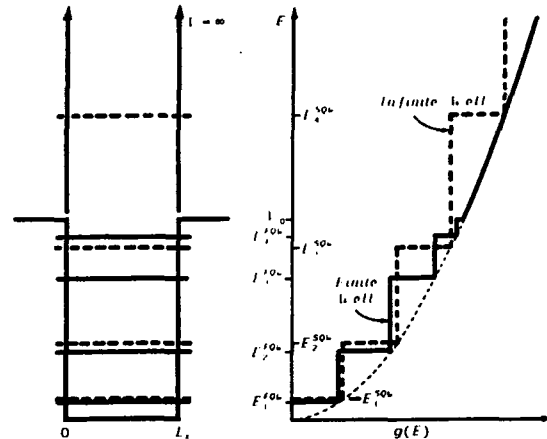


Figure 5. Comparison of energy states and DOS for an infinite single quantum well (SQW) and a finite quantum well (FQW). Notice that the energies of the states in the finite well are no longer inversely proportional to the well width, and the DOS is not inversely proportional to the square of the width.

Note that in this case, the DOS for a thin well has nearly the same DOS as a well twice as big as the first. This is contrary to the infinite well case, where the DOS of the first state of the thinner well is four times as great as the DOS of a well that is twice as wide! The consequence is that in a real system with very thin wells, calculations which depend on the density of states, such as the capture or emission of charge carriers, become less dependent on the width of the well. In this case, other factors such as the spatial extent of the wavefunction become more important.<sup>8</sup>

## Superlattices

When two finite quantum wells are placed near each other such that the barrier between them is small enough to allow interaction between the wells, the degenerate states split into two bound states of nearly the same energy. If this multiple quantum well arrangement were extended to many wells placed together, then the energy levels broaden into bands, much like the energy bands of the host crystal which are due to the periodicity of the atomic lattice. The differences are that the quantum well lattice is one dimensional with a period several times greater than that of the crystal, and the energy bands due to the coupled wells are superimposed onto the allowed energy bands of the host.

Such a structure, first proposed by Esaki and Tsu in 1969, is called a superlattice due to the periodic potential superimposed on the crystal's periodic potential, which gives rise to a new band structure.<sup>9</sup> The new potential is due to an array of square wells of width  $L_z$ , separated by barriers of width  $L_b$  and height  $U_0$ . Applying the tight-binding approximation to the new periodic potential, the superlattice energy bands can be calculated. For the periodic superlattice potential

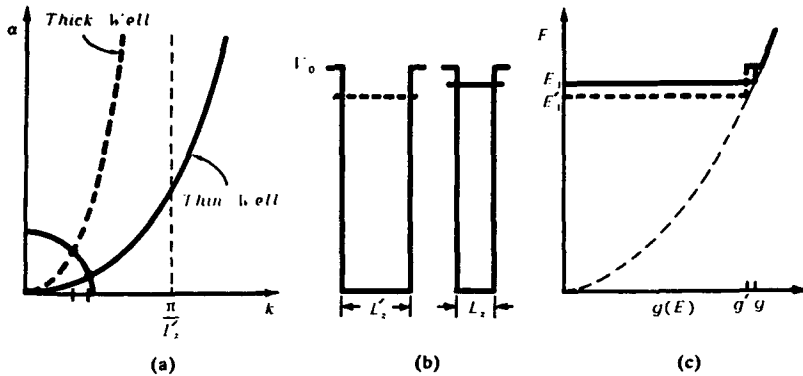


Figure 6. (a) Graphical solution for well with  $2L_z = L'_z$ ,  $\gamma \ll \pi/L'_z$ , (b) Single bound state for both wells, and (c) The DOS for the corresponding wells. Notice that the DOS of the thin well is *not* four times that of the thick well. In fact, for ultra-thin wells, the DOS of both wells may be nearly equal.

$U(z) = U(z - nd)$ , where  $d$  is the period of the superlattice,  $L_z + L_b$ , and  $n$  is an integer, the energies can be found using<sup>10</sup>

$$E = E^{SL} = \frac{\langle \psi_n | \mathcal{H}^{SL} | \psi_m \rangle}{\langle \psi_n | \psi_m \rangle} \quad (19)$$

where

$$\mathcal{H}^{SL} = \left\{ -\frac{\hbar^2}{2m} \frac{\partial^2}{\partial z^2} + U(z) \right\} \quad (20)$$

and

$$\psi_{n(m)}^{SL} = \sum_{n=1}^N e^{ik_z d} \psi^{FQW}(z - nd) \quad (21)$$

for  $N$  wells. Solving (19) yields

$$\begin{aligned} E^{SL} &= E^{FQW} - \alpha - \beta (e^{ik_z d} + e^{-ik_z d}) \\ &= E^{FQW} - \alpha - 2\beta \cos(k_z d) \end{aligned} \quad (22)$$

where

$$\alpha = \int_z (\psi^{FQW}(z))^* U(z) \psi^{FQW}(z) dz, \quad (23)$$

which is the shift from  $E^{FQW}$  due to the coulombic interaction of the coupled wells, and  $\beta$  is the exchange energy which determines the extent of the band broadening, and is given by

$$\beta = \int_z (\psi^{FQW}(z - d))^* U(z) \psi^{FQW}(z) dz, \quad (24)$$

assuming appreciable interaction from adjacent wells only. The important thing to note about  $\alpha$  and  $\beta$  is that as the barrier width decreases, the interaction

between wells should increase, and thus  $\alpha$  and  $\beta$  should increase.

The energy bands of a superlattice, as shown in Figure 7(a), can be found using Equation (19), with the total energy written as

$$\begin{aligned} E &= E^{SL} + \frac{\hbar^2}{2m} (k_x^2 + k_y^2) \\ &= E_0 - 2\beta \cos(k_z d) + \frac{\hbar^2}{2m} (k_x^2 + k_y^2) \end{aligned} \quad (25)$$

where  $E_0 = E^{FQW} - \alpha$ . The divergence of the total energy with respect to the wavevector is

$$\nabla_k E = 2d\beta \sin(k_z d) \hat{z} + \frac{\hbar^2}{m} (k_x \hat{x} + k_y \hat{y}),$$

so the magnitude is then

$$|\nabla_k E| = \sqrt{4d^2 \beta^2 \sin^2(k_z d) + \left(\frac{\hbar^2}{m}\right)^2 (k_x^2 + k_y^2)} \quad (26)$$

The differential surface area of the constant energy surface is given by Equation (5). Recall that the differential change in energy of a *constant* energy surface is zero, so we can relate  $dE$  to  $dk_z$ . Let  $k^2 = k_x^2 + k_y^2$ , then  $dE = 0$  becomes

$$dE = 0 = 2\beta d \sin(k_z d) dk_z + \frac{\hbar^2}{m} k dk_k.$$

so

$$dk = -\frac{2m \beta d}{\hbar^2 k} \sin(k_z d) dk_z. \quad (27)$$

The differential surface area of Equation (5) then becomes

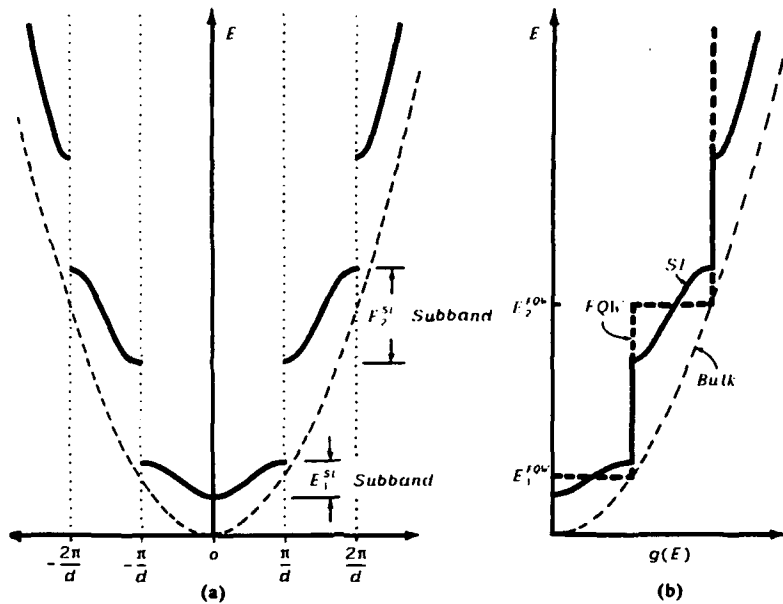


Figure 7. (a) Dispersion relation for a superlattice, and (b) DOS for a superlattice versus single well and bulk. Because the interaction between wells causes the bound states to broaden into bands, the DOS is no longer constant as with the finite well, but it does retain a step-like nature.

$$dS = k d\phi \sqrt{\left(\frac{2m^* \beta d}{\hbar^2 k}\right)^2 \sin^2(k_z d) (dk_z)^2 + (dk_z)^2} \quad (28)$$

which, using Equation (26), can be re-written as

$$\begin{aligned} dS &= d\phi dk_z \frac{m^*}{\hbar^2} \sqrt{4d^2 \beta^2 \sin^2(k_z d) + \left(\frac{\hbar^2}{m^*}\right)^2 k^2} \\ &= d\phi dk_z \frac{m^*}{\hbar^2} |\nabla_k E| \end{aligned} \quad (29)$$

Putting this in the DOS Equation (1), we get

$$\begin{aligned} g_3^{SL}(E) &= \frac{1}{4\pi^3} \int \frac{dS}{|\nabla_k E|} \\ &= \frac{1}{4\pi^3} \frac{m^*}{\hbar^2} \int_{-k_z}^{k_z} \int_0^{2\pi} \frac{|\nabla_k E|}{|\nabla_k E|} d\phi dk_z \\ &= \frac{m^*}{4\pi^3 \hbar^2} 2\pi \int_{-k_z}^{k_z} dk_z \\ &= \frac{m^*}{2\pi^2 \hbar^2} 2 \int_0^{k_z} dk_z \\ &= \frac{m^*}{\pi^2 \hbar^2} k_z. \end{aligned} \quad (30)$$

which is the same as Equation (8). The next step is to solve for  $k_z$ , but normalize the problem first by defining a dimensionless energy that is zero below the bottom of a subband, and has a value of one for energies above the subband. Using Equation (25), and adding and subtracting  $2\beta$ ,

$$E = E_0 + \frac{\hbar^2 k^2}{2m^*} - \frac{1}{2} 4\beta \cos(k_z d) + \frac{4\beta}{2} - 2\beta. \quad (31)$$

Rearranging,

$$\frac{E - E_0 - \frac{\hbar^2 k^2}{2m^*} + 2\beta}{4\beta} = \frac{1}{2}(1 - \cos k_z d) = \xi \quad (32)$$

where  $\xi$  is the new dimensionless energy. Now solving for  $k_z$ , we get

$$k_z = \frac{1}{d} \arccos(1 - 2\xi) \quad (33)$$

The DOS for a superlattice is then

$$g_3^{SL}(E) = \frac{m^*}{\pi^2 \hbar^2 d} \begin{cases} 0 & : \xi < 0 \\ \arccos(1 - 2\xi) & : 0 \leq \xi \leq 1 \\ \pi & : \xi > 1 \end{cases} \quad (34)$$

which is shown in Figure 7(b). To express  $g_3^{SL}(E)$  as  $g_3^{SL}(\xi)$ , we must note that

$$g_3^{SL}(E)dE = g_3^{SQW}(\xi)d\xi \quad (35)$$

and

$$d\xi = \frac{1}{4\beta} dE \quad (36)$$

So Equation (35) becomes

$$g_3^{SL}(\xi)d\xi = g_3^{SQW}(E)4\beta dE$$

or,

$$g_3^{SL}(\xi) = \frac{4\beta m^*}{\pi^2 \hbar^2 d} \arccos(1-2\xi) : 0 \leq \xi \leq 1 \quad (37)$$

Recall that this analysis was for *each* subband, so we must modify the equation to represent the general case. From the superlattice dispersion relation (Figure 7(a)) we see that, along with Equation (33), that the general form of the wavevector is

$$k_z = \frac{n\pi}{d} + \frac{1}{d} \arccos(1-2\xi_i) \quad (38)$$

where  $n$  is the number of filled subbands, and  $\xi_i$  is the dimensionless energy of the  $i^{th}$  subband where  $i = n + 1$  (recall that each  $\xi_i$  is unique since  $\xi_i$  depends on  $E^{SQW}$ ,  $\alpha$  and  $\beta$ , all of which change for different subbands). The total superlattice DOS is then

$$g_3^{SL}(E) = \frac{m^*}{\pi^2 \hbar^2 d} [n\pi + \arccos(1-2\xi_i)] \quad (39)$$

for  $0 < \xi_i < 1$ . For energies that fall between the  $n^{th}$  and  $i^{th}$  subband, we have

$$\begin{aligned} g_3^{SL}(E) &= \frac{m^*}{\pi^2 \hbar^2} \frac{n}{d} \\ &= g_2(E) \frac{n}{d} \end{aligned} \quad (40)$$

which looks a lot like Equation (10) ( $g_3^{SQW}(E)$ ), except that we have the factor of  $1/d$  instead of  $1/L_z$ . This is because the superlattice DOS depends on the interaction of coupled wells in a periodic potential of period  $d$ , while the single quantum well DOS depends only on  $L_z$  since there is no interaction from other wells.

### Equivalence of DOS Expressions

The single quantum well DOS derived earlier should reduce to the 3D DOS if the well width is allowed to go to infinity. As an example of this, let us find the number of electrons per unit volume in a quantum well of a non-degenerate semiconductor (i.e., let the conduction band energy,  $E_c$ , be greater than a few  $k_B T$  above the Fermi energy,  $E_F$ ). The solution should be equivalent to the electron density found

when the 3D DOS is used for the bulk semiconductor case. The expression for the electron density is<sup>11</sup>

$$\frac{N}{V} = n_e = \int_{E_c}^{E_{max}} g_3^{SQW}(E-E_c) f_{FD}(E) dE \quad (41)$$

where  $f_{FD}(E)$  is the Fermi-Dirac distribution function, which can be approximated by the Maxwell-Boltzmann distribution function,  $f_{MB}(E)$ , for a non-degenerate semiconductor where  $E_c - E_F$  is greater than a few  $k_B T$ , or

$$\begin{aligned} f_{FD}(E) &= \frac{1}{1 + e^{(E-E_F)/k_B T}} \\ &\approx e^{-(E-E_F)/k_B T} = f_{MB}(E) \end{aligned} \quad (42)$$

So the electron density,  $n_e$ , is then

$$\begin{aligned} n_e &= \int_{E_c}^{E_{max}} \frac{m^*}{\pi^2 \hbar^2} \frac{n}{L_z} e^{-\frac{(E-E_F)}{k_B T}} dE \\ &= \frac{m^*}{\pi^2 \hbar^2 L_z} e^{\frac{E_F}{k_B T}} \int_{E_c}^{E_{max}} n e^{-\frac{E}{k_B T}} dE \end{aligned} \quad (43)$$

Notice that  $n$  is a function of  $E$  that increases by one for each additional bound state. For the bottom of each step in the DOS curve, let  $E - E_c = E_n$ , and let  $(E_{max} - E_c) \gg k_B T$ , and take the contribution of each bound state separately, as in Figure 8,

$$\begin{aligned} n_e &= A + B + \dots \\ &= \frac{m^*}{\pi^2 \hbar^2 L_z} [e^{\frac{E_F}{k_B T}} \int_{E_1}^{\infty} e^{-\frac{E}{k_B T}} dE \\ &\quad + e^{\frac{E_F}{k_B T}} \int_{E_2}^{\infty} e^{-\frac{E}{k_B T}} dE + \dots] \\ &= \sum_n \frac{m^*}{\pi^2 \hbar^2 L_z} e^{\frac{E_F}{k_B T}} \int_{E_n}^{\infty} e^{-\frac{E}{k_B T}} dE \end{aligned} \quad (44)$$

or

$$\begin{aligned} n_e &= \sum_n \frac{m^* k_B T}{\pi^2 \hbar^2 L_z} e^{-\frac{(E_n - E_F)}{k_B T}} \\ &= \left[ \frac{m^* k_B T}{\pi^2 \hbar^2 L_z} \sum_n e^{-\frac{(E_n - E_F)}{k_B T}} \right] e^{-\frac{(E_c - E_F)}{k_B T}} \\ &= N_c^{SQW} e^{-\frac{(E_c - E_F)}{k_B T}} \end{aligned} \quad (45)$$

where  $N_c^{SQW}$  is the effective DOS for the conduction band electrons in a quantized system. As  $L_z$  grows large, the bound states will drop toward  $E_c$ , and will eventually form an energy band, as in the bulk material. When this happens, we can say that the number of bound states in the band is large (note in Equation (10) that  $L_z \propto n$ ), so as  $L_z$  goes to infinity,  $n$  also goes to infinity, and we should get the same  $N_c$  as for the 3D bulk case. In the limit of the sum going to an integral,

$$\begin{aligned} \sum_n e^{-\frac{(E_n - E_c)}{k_B T}} &\approx \int_0^\infty e^{-\frac{(E_n - E_c)}{k_B T}} dn \\ &= \int_0^\infty e^{-\frac{\pi^2 n^2}{2m^* L_z^2 k_B T}} n^2 dn \\ &= \sqrt{\frac{\pi}{2}} \cdot \sqrt{\frac{2m^* L_z^2 k_B T}{\pi^2 \hbar^2}} . \end{aligned} \quad (46)$$

Substituting Equation (46) into  $N_c^{SQW}$  gives

$$\begin{aligned} N_c^{SQW} &= \left( \frac{m^* k_B T}{\pi \hbar^2 L_z} \right) L_z \sqrt{\frac{m^* k_B T}{2\pi \hbar^2}} \\ &= 2 \left( \frac{m^* k_B T}{2\pi \hbar^2} \right)^{\frac{3}{2}} , \end{aligned} \quad (47)$$

which is exactly the value for the bulk case, where<sup>11</sup>

$$N_c^{BULK} = 2 \left( \frac{m^* k_B T}{2\pi \hbar^2} \right)^{\frac{3}{2}} . \quad (48)$$

Since Equations (47) and (48) are equivalent,  $N_c^{SQW} = N_c^{BULK}$  in the limit as  $L_z$  goes to infinity. This is equivalent to saying that the general 2D DOS is the same as for the bulk case in this limit since the only difference between these expressions is the DOS functions used at the start of their derivations.

To see how Equation (40) for the superlattice DOS relates to the single quantum well case,  $g_3^{SQW}(E)$ , we must move the wells of the superlattice apart ( $L_b \rightarrow \infty$ ), which removes their interaction. This results in  $\alpha$  and  $\beta$  both going to zero, so Equation (25) becomes

$$\begin{aligned} E &= E^{SQW} + \frac{\hbar^2 k^2}{2m^*} \\ &= \frac{\pi^2 \hbar^2 n^2}{2m^* L_z^2} + \frac{\hbar^2 k^2}{2m^*} \\ &= \frac{\hbar^2}{2m^*} \left( \frac{\pi^2 n^2}{L_z^2} + k^2 \right) \end{aligned}$$

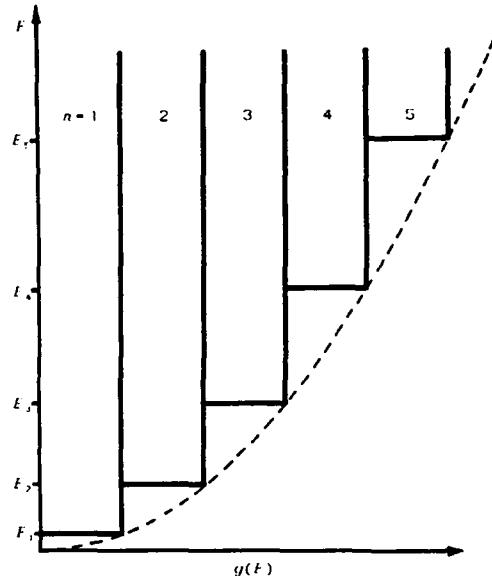


Figure 8. The DOS near the bottom of a wide quantum well. The contribution of electrons from each bound state is found when each element of the DOS is integrated with the distribution function, giving the total number of electrons as the sum of each contribution.

$$= \frac{\hbar^2}{2m^*} (k_z^2 + k^2) , \quad (49)$$

which means that  $k_z = n\pi/L_z$  in the limit of large barriers. Using this wavevector in Equation (31), we get

$$\begin{aligned} \lim_{L_b \rightarrow \infty} g_3^{SL}(E) &= \frac{m^*}{\pi^2 \hbar^2} \frac{n\pi}{L_z} \\ &= \frac{m^*}{\pi \hbar^2} \frac{n}{L_z} \\ &= g_3^{SQW}(E) \end{aligned} \quad (50)$$

Similarly, to show how the superlattice DOS relates to the bulk case,  $g_3(E)$ , we can either let  $L_b$  vanish, or let  $L_z$  go to infinity. If  $L_b$  gets small, the coupling between the wells get stronger, and the subbands broaden until the steps in the  $E$  vs  $g_3^{SL}(E)$  curve merge and form a continuous parabolic curve. Note that the symmetrical shape of the steps in Figure 7(b) are arc cosine functions, which is due to the assumption that only nearest-neighbor interactions contribute in the tight-binding theory. For very strong coupling, however, wells beyond the nearest neighbors must be considered since the spatial extent of the electron wavefunctions become large. This apparent failure of the tight binding method<sup>12</sup> will result in the loss of the arc cosine symmetry of the steps, and should allow the

shape of the steps to conform more to the parabolic bulk case.

If, however, we let  $L_z$  get large, the carrier wavefunction will be more confined in the wells, which reduces the coupling and causes the subbands to narrow. But increasing  $L_z$  also has the effect of moving the subbands down in energy (remember that the subbands are nearly centered on the bound states of the single quantum well), which would cause them to stack up at the bottom of the wells. For a large well width, the steps in the  $E$  vs  $g_3^{SL}(E)$  curve will become so small and numerous that they will form a quasi-continuous curve that will approach the bulk DOS case. In either case, the energy band would approach the bulk case, where  $E(k)$  can be approximated by a parabolic curve, and  $k_z$  would become

$k_z = \sqrt{2m^*E/\hbar}$ . Using this intuitive analysis in Equation (38), we get

$$k_z = \frac{n\pi}{d} + \frac{1}{d} \cos^{-1}(1 - 2\xi_1) \approx \frac{\sqrt{2m^*E}}{\hbar} \quad (51)$$

and Equation (39) becomes

$$g_3^{SL}(E) = \frac{m^*}{\pi^2\hbar^2} \cdot \frac{\sqrt{2m^*E}}{\hbar} - \frac{\sqrt{2(m^*)^2}}{\pi^2\hbar^3} \sqrt{E} \quad (52)$$

which is the 3D DOS given in Equation (11).

### Conclusions

The derivation of the DOS function for quantum wells and superlattices is straight forward when approached with some insight into the physical constraints of these structures. The pure 2D infinite well case proved to be inadequate for the treatment of actual quantum well systems because it ignores the well width and higher-order bound states of the quantum well. The finite well case was obtained when the appropriate boundary conditions were applied. Special

care must be taken when analyzing very thin wells because the energy levels may or may not be strongly dependent on the well width. The superlattice DOS was then derived by considering the interaction of an array of finite quantum wells. Finally, we showed that each of the above cases is consistent with the others when the appropriate limits of well or barrier width are taken into account.

**Acknowledgement** - This work was supported by Strategic Defence Initiative Organization/Innovative Science and Technology Office through the Army Research Office DAAL 03-90-G-0018. We also thank K. Kim for his assistance in checking the derivation of the superlattice DOS, and S. Prairie for her editing skills.

### References

1. M. Krah, J. Cristen, D. Bimberg, D. Mars, and J. Miller, "Impact of Well Coupling on the Spontaneous Emission Properties of GaAs/AlGaAs Multiple-Quantum-Well Structures," *IEEE J. Quantum Elect.*, QE-25, pp. 2281-8 (1989).
2. C. Kittel, *Introduction to Solid State Physics*, 6th ed., John Wiley and Sons, New York (1986), pp. 111-2.
3. R. H. Bube, *Electronic Properties of Crystalline Solids*, Academic Press, New York (1974), pp. 87, 172.
4. J. P. McKelvey, *Solid State and Semiconductor Physics*, Robert E. Krieger Publishing Company, Inc., Malabar, FL (1966), p. 85.
5. C. Kittel, *ibid.*, p. 133.
6. *ibid.*, p. 128.
7. J. P. McKelvey, *ibid.*, pp. 88-91.
8. R. M. Kolbas, Y. C. Lo and J. H. Lee, "Laser Properties and Carrier Collection in Ultrathin Quantum-Well Heterostructures," *IEEE J. Quantum Elect.*, QE-26, pp. 25-31 (1990).
9. L. Esaki and R. Tsu, "Superlattice and Negative Differential Conductivity in Semiconductors," *IBM J. Res. Develop.*, 14, 61 (1970).
10. C. M. Wolf, N. Holonyak, Jr., and G. E. Stillman, *Physical Properties of Semiconductors*, Prentice Hall, Englewood Cliffs, NJ (1989), pp. 47-9.
11. C. Kittel, *ibid.*, p. 202.
12. N. W. Ashcroft and N. D. Mermin, *Solid State Physics*, Saunders, Orlando, FL (1976), pp. 184-5.

## 9.4 Index

- 3 dB coupler, 97
- Absorption coefficient, 25, 72
- Alloy scattering, 86
- Antisite defect, 7
- Bandgap of GaAs, 44
- Boltzmann-Matano method, 19
- Bound states
  - error function profile, 42
  - experimentally determined, 54
- Bound states, 19
- Carrier dynamics, 87
- Composition profile
  - error function, 42
- Compositional dependence, 49
- Coupling coefficient, 97
- Coupling length, 97
- Crystal growth, 28
- Damping coefficient, 27, 88
- Defect transport, 13, 87
- Density of states, 89
  - intermixed superlattice, 91
  - quantum well, 89
- Device processing, 38
- Dielectric constant, 24, 26, 72, 89, 90
  - background, 73, 92
- Dielectric encapsulation, 10
  - strain effects, 13
  - stress field, 13
- Diffusion coefficient, 7
- Directional coupler, 95
- Effective mass, 47
- Einstein relations, 82
- Electron mobility, 65
- Envelope function approximation, 23
- Envelope wavefunctions, 26
- Error function, 17
  - profile, 42
- Error function model, 42
- Extinction coefficient, 25
- Fermi level, 9
- Fick's Second Law, 17, 49
- Focused ion beam, 63
- Frenkel Pair, 7
- Gain coefficient, 75
- Gallium focused ion beam, 63
- Hall mobility measurements, 40
- Heisenberg Uncertainty Principle, 88
- HEMT, 65
- Heterojunction intermixing, 6
- Heterostructure intermixing, 42
- Implantation, 14
  - arsenic, 15
  - gallium, 14
- Interdiffusion coefficient, 9
  - composition-dependent, 49
  - experimentally determined, 54
  - gallium implant, 64
- Intermixed potential wells, 16
- Intermixed quantum wells, 42
- Intermixed superlattices, 56
- Interstitial
  - gallium, 64
- Interstitial defect, 7
- Joint density of states, 25
- Kane model, 25, 74
- Kramers-Kronig transformations, 24
- Kronig-Penney model, 23, 57
- Lifetime, 82
- Line width, 88
- Lineshape, 90
- Matrix element, 26, 73, 74
- electron to heavy-hole, 27
- GaAs, 27, 74
- MODFET, 65

Natural broadening, 88  
Non-radiative lifetime, 89  
Non-radiative scattering, 86

Optical characterization, 29  
Optical matrix element, 25  
Optical properties, 24, 72  
Oscillator approach, 26  
Oscillator strength, 26, 73  
Overpressure, 10

    arsenic, 10, 35  
    gallium, 10, 35

Partially intermixed quantum structures, 3  
Passive waveguides, 93  
Photoluminescence spectroscopy

    time-integrated, 31  
    time resolved, 32

Poschl-Teller potential, 21  
Potential wells, 16

Quantum wire, 16

Radiative lifetime, 82, 88  
Rapid thermal annealing, 14  
Reduced density of states, 89  
Reduced mass, 90  
Reflectivity, 72  
Refractive index, 72

    AlGaAs alloy, 92  
    annealed 5-ML well, 95  
    group, 82  
    intermixed quantum well, 92

Scattering, 88  
Selective disordering, 15  
Selective intermixing, 63, 95  
Selectivity ratio, 67, 95  
Self-diffusion coefficient, 9  
Shooting method, 21  
SiNx encapsulation, 67  
Spontaneous emission, 82  
Stimulated emission, 82  
Stop-growth, 84  
Substitutional defect, 7  
Superlattice energy dispersion, 22, 58

Thermal annealing, 34  
Thermal intermixing, 6  
Thermal scattering, 87

Tight-binding approximation, 22, 56  
Two-dimensional electron gas, 65

Vacancy, 7

Wavelength shift, 47